A flexible low-cost quantitative phase imaging microscopy system for label-free imaging of multi-cellular biological samples

By

Chandrabhan Seniya

Thesis

Submitted to the University of Warwick

for the degree of

Doctor of Philosophy in Engineering

School of Engineering

February 2018

THE UNIVERSITY OF
WARWICK

TABLE OF CONTENTS

CHAPTER 4. OPTICAL DESIGN: LOW-COST QUANTITATIVE PHASE IMAGING MICROSCOPE..52

LIST OF FIGURES

LIST OF TABLES

ACKNOWLEDGEMENTS

I would like to express profound gratitude and sincere thanks to my supervisor Professor David Towers for his invaluable support, encouragement, belief, inspirational guidance, and instilling skills over the past four years in the optical microscopy, live cell imaging, and mathematical modelling. His moral support and fruitful guidance enabled me to complete my research work successfully in time.

Besides my supervisor, I would like to thank the Madhya Pradesh State, Govt. of India for providing partial funding including maintenance allowances and full tuition fees to the University of Warwick, United Kingdom for doctoral research work. I also thank the School of Engineering at the University of Warwick for the partial supporting maintenance allowances in the UK.

My immense gratitude is extended to Dr. Jiang Shihong, (Research Fellow) for helping in MATLAB and LabVIEW programme codes. The critiques provided by Dr Shihong helped me to design the optical experiments and increased my level of understanding of optical instrumentation. I benefited a great deal from discussions with Dr. Christian Kroner (Research Fellow). His inspirational attitude helped me to stay positive and enthusiastic for the project.

Finally, I would like to thank my wife and my son, the two most beautiful and valuable persons, for giving all necessary support and time to carry research work.

I would like to dedicate this research work to the memory of my father.

CHANDRABHAN SENIYA

DECLARATION

The candidate confirms that the work embodied in this thesis is his own and that proper credit has been given to the works that were taken advantage during this piece of research work. I, CHANDRABHAN SENIYA, hereby declare that I have produced this thesis without the prohibited help of third parties and without making use of aids other than those specified and the notions taken directly or indirectly from other sources have been given proper credit.

This thesis has not previously been presented in a similar or identical form to any other University for the award of Doctor of Philosophy. The research work embodied in this thesis was conducted from January 2014 to October 2017 in the Optical Engineering and Imaging Laboratory under the supervision of Prof David Towers, Head of School, School of Engineering, The University of Warwick, United Kingdom.

LIST OF PUBLICATIONS

Papers/Conference proceedings published

1. **C. Seniya,** C.E. Towers, D.P. Towers, A flexible low-cost quantitative phase imaging microscopy for label-free imaging of biological samples using aperture masks, Optics Express. (Manuscript submitted)

2. **C. Seniya,** C.E. Towers, D.P. Towers, Improvements in low-cost label-free QPI microscope for live cell imaging, Proc. SPIE 10414, Advances in Microscopic Imaging. 104140F (July 28, 2017).

3. **C. Seniya,** C.E. Towers, D.P. Towers, [LS5.2009] Developments in low-cost label-free live cell imaging for biological samples, In MMC2017, Manchester 3-6th July 2017.

4. **C. Seniya,** C.E. Towers, D.P. Towers, Low-cost label-free live cell imaging for biological samples, in Quantitative Phase Imaging III. Gabriel Popescu; YongKeun Park, Editors, Proceedings of SPIE Vol. 10074 (SPIE, Bellingham, WA 2017), 100741I.

5. **C. Seniya,** C.E. Towers, D.P. Towers, Phase shift interference microscopy for label-free live cell imaging of biological samples, 4th Annual School of Engineering Symposium. University of Warwick, pp. 85-86, 22nd April 2016.

Posters Presented

1. **C. Seniya,** D.P. Towers, Low-cost Quantitative Phase Microscope for live cells imaging, in Warwick Medical Imaging Network meeting. University of Warwick, 28th April 2017. **[Best poster prize for early career researchers (£250)].**

2. **C. Seniya,** D.P. Towers, Cost-effective method for label-free live cell imaging of biological sample, in Research Poster Competition 2016 (Research Student Skills Programme). University of Warwick, 9th June 2016.

Note: The poster was selected to display in the Research Exchange (Library) during the summer period.

3. **C. Seniya,** D.P. Towers, Generate and evaluate tools to quantify cell: cell contacts in live cell imaging of label-free biological samples, Annual Postgraduate Symposium 2015, School of Engineering, University of Warwick.

LIST OF ABBREVIATIONS AND SYMBOLS USED

Abbreviation/symbol	Full form/ meaning
BW	Bandwidth
CCD	Charged-coupled device
CL	Coherence length
CPI	Common-path interferometry
CW	Centre wavelength
DHM	Digital holography microscopy
DPM	Dynamic phase microscope
DIC	Differential interference contrast
DIM	Dynamic interference microscopy
FOV	Field of view
FPM	Fourier phase microscopy
FWHM	Full width half maximum
GFP	Green fluorescent protein
ID	Inner diameter
LCA	Laser-cut aperture
LED	Light emitting diode
LQPIM	Low-cost quantitative phase imaging microscope
MoM	Magnification of microscope
ms	Milliseconds
NA	Numerical aperture
nm	Nanometer
OCT	Optical coherence tomography
OD	Outer diameter
OPD	Optical path difference
OPL	Optical path length
PCM	Phase contrast microscopy
PIM	Phase imaging microscope
PSA	Phase shifting algorithm

PSI	Phase shift interferometry
PSM	Phase shifting module
PZT	Piezoelectric transducer
QPI	Quantitative phase imaging
R	Resolution of microscope
SLIM	Spatial light interference microscopy
SLM	Spatial light modulator
Std Dev	Standard deviation
WDT	White-light diffraction tomography
WLI	White light illumination
wDPM	White-light diffraction phase microscopy
2D	Two dimensions
3D	Three dimensions
4D	Four dimensions
3F@90°	Three frames at 90°
3F@120°	Three frames at 120°
4F@90°	Four frames at 90°
5F@90	Fiver frames at 90°
7F@90°	Seven frames at 90°
6+1F@60°	Six plus one frame at 60°
h(x, y)	Height at point (x,y)
I(x, y)	Intensity of the image field at point (x,y)
$\mathbf{I_{dc}}$	Non-scattered image light field
$\mathbf{I_{ac}}$	Scattered image light field
k(x, y)	Fringe order
Δφ(x, y)	Phase change at point (x,y)
t(x, y)	Thickness at point (x,y)
α	Mean phase shift or step angle
γ	Signal modulation
δ	Standard deviation (Std Dev)
σ_φ	Phase noise
φ_{ns}	Phase from background field
φ_s	Phase from scattered field
$\mathbf{n_{air}}$	Refractive index of air
$\mathbf{n_b}$	Refractive index of background or surrounding fluid

n_o	Refractive index of object
nm	Nano-meter (10^{-9})
μm	Micrometre (10^{-6})
λ	Wavelength of illumination source
Δλ	Spectral width
υ	Frequency of light wave

ABSTRACT

In this thesis, a flexible low-cost quantitative phase imaging microscopy (LQPIM) system for imaging both thin and thick biological phase objects in a non-contact, non-invasive, and label-free manner is reported. LQPIM optics was developed based on classical Zernike's phase contrast approach and an additional phase shifting module to introduce user-defined phase modulations by utilising standard optical components. The phase shifting was performed using twin concentric mirrors or laser cut apertures in the arms of a Michelson interferometer where the reference mirror can be moved in λ / n steps $(n$ - number of steps) with a piezoelectric transducer. Hence, the optical phase shifting modules are 10 - 15% (approximately) of the cost compared to the more widely reported modules based on spatial light modulator. In the microscope implementation reported in this thesis, a total magnification of 25x was achieved utilising relay lenses in LQPIM optics together with a standard 10x objective lens. The imaging system was simulated in MATLAB, where two-beam interference equation with varying bandwidth (1 – 250 nm), centre wavelength (450 – 650 nm) of the illumination sources and a range of previously reported phase shift algorithms (PSA) were used. The simulation results confirm that the optimum phase resolution is achievable if a broadband source of bandwidth 30 - 50 nm is used for illuminating thin (i.e. ≤ 250 nm) and thick (i.e. ≥ 1250 nm) biological samples. The four frames at 90° PSA and six plus one frames at 60° PSA offer different compromises between image acquisition time, phase resolution and out-perform other PSAs. A phase resolution of 0.382 nm and 0.317 nm was achieved using four frames at 90° and six plus one frames at 60° PSAs, respectively for the broadband illumination from a green LED. A coherent, single longitudinal mode laser source with a rotating diffuser for speckle averaging, gave 0.667 nm and 0.512 nm phase resolution using the same algorithms mentioned above. The parasitic fringes resulted in reduced resolution; hence, incoherent LED illumination was preferred. Measurements are presented over a longer optical path difference (≥ 1250 nm) than hitherto reported for a similar microscope. The given exemplar data demonstrates an ability of LQPIM system to quantify cellular and sub-cellular structures at the nanoscale in epidermis cells of *Allium cepa*.

Key words: Quantitative phase imaging, low-cost, optical microscopy, phase imaging and phase shift imaging.

Chapter 1. INTRODUCTION

To understand cellular physiology (cell cycle and cellular growth) and cellular mechanics or dynamics (protein transport and migration) are very important in the field of cell biology and biomedicine, especially without perturbing their natural activity. Furthermore, the cellular phenomenon is very complex and challenging in the context of microscopy imaging due to the fast migration of fine spatial objects, varying cell to cell contacts and changing structural organisation, hence, several highly sensitive spatial and temporal measurements can be associated for large-scale measurements. The time-scale ranging from milliseconds to hours to measure from sub- scale to millimetre scale are very important to address the cellular and subcellular structural dynamics.

There is an unresolved need in biological science to understand homoeostasis in live cell imaging experiments and precisely the role of a cell to cell contact that is believed to inhibit mitosis and potentially other growth mechanisms. In contrast, when cell to cell contact is not present, e.g. when a tissue has wounded, the edges of the wound generate cells with free surfaces, and repair mechanisms are needed to create cells to repair the wound. This leads to a controversial philosophy that the local environment of cells, which determine the phenotype of the cells, drives homoeostasis rather than a stem cell needed as an initiator for the regeneration mechanism. Investigating these phenomena needs advanced microscopy techniques to quantify the interaction between cells in live cell imaging experiments where homeostasis can be maintained for an extended periods to observe cells over the long duration (i.e. hours to days). This requirement limits the available techniques away from the prevalent use of fluorescence as the mainstay of generating contrast. Furthermore, an introduction of, generally, toxic fluorescence reporters limits the cell viability and natural functionality. Live cell imaging experiments play a vital role in addressing many issues, for example to understand complex biological process in the cell, drug development studies, cancer-related studies, morphological variations, cell to cell contacts, structural organisation of cellular and subcellular organelles and tissues. The imaging experiments can also give an insight into cellular functionality, mortality, biomechanical properties, effect of toxins and drugs on cells. An ideal microscopy method should be non-invasive, non-contact, and able to render both qualitative and quantitative information without altering the inherent properties of the living specimen.

The epi-fluorescence microscopy methods have been readily applied to study cellular and subcellular live events at the molecular level [1]. The observation of cellular structures, for example mitochondria, cell membrane, nucleus, cytoskeleton proteins and vesicles in 3D with a resolution down to scales [2] have been possible using flourescent labelling agents. However, these observations may have limitations due to high cost of molecule specific fluorophore agents, modification of natural bio-activity, photo-toxicity to healthy cells and photo-bleaching [3], [4]. The discovery of green fluorescent protein (GFP) has revolutionised measurements on live cells using epi-fluorescence microscope, where test cells are expected to express GFP genetically [5], [6]. Furthermore, the prolonged exposure with high-intensity illumination is required to visualise such genetically modified cellular moieties with tagged auto fluorescence dyes. In this case, only a low temporal resolution and low quantum efficiency can be achieved, and the prolonged exposure can cause phototoxicity to healthy cells and alteration of natural events. Therefore, the label-free, non-invasive, non-contact, and non-cell altering methods can be a better choice to understand the cellular and sub-cellular events natively.

Practically, all the biological cells are transparent in nature and hard to image with most straightforward label-free imaging techniques, for example bright field microscopy, because they generate minute changes in the amplitude of light whilst altering the phase significantly [7]. Therefore, to examine such phase objects an optical development in contrast-enhancing imaging techniques, such as phase contrast microscopy (PCM) [8] and Differential Interference Contrast (DIC) [9] have been developed. These modalities can provide an enhanced contrast at an expense of additional optical components, light source and critical alignment procedures. The information retrieved was only qualitative. Hence, none of the method with labels or without labels (conventional phase contrast) are able to render quantitative information regarding thick cell cultures, especially, 3D cell colonies.

The imaging technologies developed in the mid-20th century and innovations in optical instrumentation have become very attractive to biomedical scientists. The advancements have fashioned a movement toward imaging at cellular and sub-cellular levels in a label-free manner for the deeper understanding of the biological events. A variety of optical methods have been developed to image both labelled and non-labelled samples to study cell morphology and functionality both qualitatively and quantitatively [10], for example to identify and track spatially distributed bio-molecules in a cellular medium as they function in their native background [11]. To avoid any type of modification in natural behaviour and harm to healthy cells, researchers have tried several label-free methods in past as well as in the recent years, for example optical coherence tomography [12], DIC microscopy [13], Fourier phase microscopy [14], diffraction phase microscopy [15] and modified versions of PCM, for example quantitative phase imaging (QPI) [16], [17].

The optical imaging methods yield not only morphological changes such as shape and size but also renders quantitative information of cellular structural gears, molecular details of cellular interactions and information about growth as well as death of the cells. The ability to monitor biological events in real-time at the cellular and sub-cellular level has widened understanding of many physiological processes inside the cell including translocation of cellular organelles, protein trafficking, protein-protein interactions and DNA-protein interactions [18]. Optical imaging microscopy relies on the introduction of contrast between transparent biological objects and their surrounding media, tissues, or cellular structures. The label-based cellular assays can help in identifying morphological variation and alterations inside a cell after phenotypic screening [19]. Furthermore, the phenotypic changes induced by an imaging experiment can be avoided by using non-invasive high throughput techniques. The label-free, multi-focus imaging methods can essentially work on differences in the optical path lengths to enhance image contrast for the qualitative analysis of desired information. An interferometry based techniques such as DIC [20] or digital holography do not readily provide quantitative information on the specimen-induced phase shifts [21]. Furthermore, their inherent contrast mechanism and related image artefacts make automated cell segmentation very difficult and hardly robust [22]. Unfortunately, these methods suffer from well-known halo artefacts at cell edges, which can compromise the success rate of downstream image analysis.

1.1 Motivation

It has been reported that the cell segmentation process is complicated and non-robust for various forms of qualitative phase microscopy, however, for example the cells from a ptychography imaging system have been well segmented [23]. In practice, these images are mostly used to cell segmentation assays and potential data source for the direct analysis. Although, the interference-based microscopy has tremendous advantages, however, qualitatively it is still affected by the optical low contrast and noise associated with the instrument. These effects can be removed to a certain extent by employing post-processing methods.

Common path interferometry (CPI) is a well-known universal tool for extracting and quantifying phase distributions from the optically transparent objects [24], [25]. The researchers have, recently, combined PCM with QPI to develop an optimal solution to study the cellular dynamics of weakly scattering and absorbing biological specimen [16], [26]–[28]. The cellular functions of spatially fine sutures can be quantified at scale or even at sub- scale by detecting the optical path length change induced by the cellular structures [29], [30]. QPI based methods have been applied to measure red blood cells dynamics [31], [32], average tissue refractive index [33]–[36], cell dry mass [36]–[38] and statistical parameters [39]. QPI methods based on common-path optics have shown superior stability in phase measurement over long time periods [15]. However, the operational field of view and/or accuracy are limited in some QPI methods because they are constrained to the assumption of a plane reference wave [14], [15].

A good phase resolution can be achieved in diffraction phase microscopy (DPM), but the speckle noise generated by high coherence illumination (i.e. laser source) has limited the achievable resolution [15]. A common-path optical system, known as spatial light interference microscopy (SLIM) was reported in 2011, by employing a broadband illumination source and a SLM for phase filtering [26]. The merit of the method arises from the use of broadband illumination to largely eliminate the coherent noise, but the approach introduces a need for expensive and specialised components, for example, the spatial light modulator (SLM), phase contrast illumination and a dedicated objective lens in combination with a high-speed camera. Dynamics behaviour monitoring at 12.5 frames per second has been made possible, but, with some diffraction and aberrations affecting the data quality [29], [40].

Phase shift interferometry (PSI) based method can be a robust methodology to extract and quantify the phase change induced by objects in sample under examination. It has an advantage of automatic phase determination over the image field. It also gives independent phase values for each pixel in the image. PSI methods have been applied in holographic interferometry [21], [41], quantitative phase microscopy [16], [29], [30], [42], [43] and interference based microscopy methods [21], [42]. These methods are expensive to be utilised in a biological laboratory. Therefore, there is a need to develop robust, flexible and cheaper techniques that can be easily accommodated into the scientific community. Furthermore, using the methods reported above, quantitative phase measurments have been obtained up to 20 µm into a cell culture grown on a coverslip and of optical path differences up to ≈ 240 nm, which is representative of a single layer of cells. Therefore, there is a need to develop new imaging methods that can image thick biological specimens, for example multi-layer or 3D cell cultures.

Researchers have also employed different illumination sources from narrowband to broadband wavelengths in interferometric configurations in order to resolve the fringe order ambiguity in the wrapped phases resulting from PSI [44], [45]. For example a fibre optic pressure sensor has been developed in the interferometric mode to measure the displacement of a diaphragm due to a pressure differential between an internal cavity and that externally [46]. In this case, multiple narrowband laser wavelengths were used where the multi-wavelengths allows the fringe order information to be calculated and the single mode fibre helps produce low noise interferometric signals at each wavelength [47]. The result is a sensor with high temporal bandwidth and the ability to operate over a broad range of optical path differences.

1.2 Aims and Objectives

The overall aim of this PhD research work was to develop a flexible, low-cost quantitative phase imaging microscopy technique for label-free live cell imaging and quantification of the cell to cell interactions as such processes are of fundamental importance in cell biology and cancer related studies. The objectives to reach this aim are listed below.

i. To develop theoretical models for phase measuring microscopy and light interaction with cells.

ii. To construct a practical phase measuring microscope, that can offer new capabilities in terms of phase measurement from thick biological samples.

iii. To demonstrate the efficiency of developed microscope by utilising optical and biological specimens as a proof of concept.

1.3 Original contributions

From the literature, neither optical imaging with labels nor conventional phase contrast imaging with PSI are able to render quantitative information from thick cell cultures, (i.e. multilayer or 3D cell cultures). Therefore, to study complex multilayer cell-to-cell interactions or the action of signalling molecules that directs a cell's fate and biological process a suitable microscopic method and quantitative analysis are needed. The following specific aspects have been developed in this thesis.

- **To find optimal solutions for quantifying transparent thick biological specimens using theoretical models.** A relationship between the wavelength (λ), bandwidth (FWHM) of the illumination source and a suitable PSA that can be of great importance to render an optimal phase imaging solution has been addressed. This relationship plays a critical role in the phase resolution and measurement range of the microscope and has not been reported, previously. The mathematical models utilised are based on the two-beam interference equation and their performance are evaluated in terms of the phase resolution obtained (the effect of more complex models is considered within the thesis, see Chapter 4, Section 4.8). The mathematical simulations are able to show that on an average the six plus one frame at 60° PSA performed well compared to other PSAs [25], [48], especially in the case of thick samples (≥ 1250 nm). Furthermore, PSAs with low number frames have an advantage of more rapidly producing good phase maps from thin samples (≤ 250 nm), but, have failed to reconstruct phase map from thick samples (≥ 1250 nm). The simulation results also confirm that the phase measurement accuracy can be strongly dependent on the selected PSA, an optical path difference, bandwidth and wavelength of the illumination source. The obtained results have informed the design of a microscope for quantitative phase imaging from both thin and thick optical samples.

- **Construction of a flexible LQPIM system to offer new capabilities regarding phase measurement from thick biological samples.** The LQPIM optical system has been developed using standard optical components. The optical imaging method has been implemented with either twin concentric mirrors or laser-cut apertures (LCAs) combines Zernike’s PCM approach and a phase shifting module (PSM) to enable phase modulation between the scattered and non-scattered optical image fields. In both setups, the phase shift is simple to control via a piezoelectric (PZT) driven high precision linear stage holding a reference mirror in the back focal plane of LQPIM system. In practice, most commercial condensers position the illumination annulus at an intermediate numerical aperture. The use of a mirror system with twin concentric mirrors will limit the NA of the system due to leakage of light in the space between concentric mirrors and hence worsen the lateral resolution. This approach has an advantage of common path interferometric optics, simple in design with less optical components and most importantly, the twin-machined concentric mirrors are significantly cheaper than the specialised components, e.g. an SLM used in other quantitative phase measuring microscopes.

To overcome the difficulty associated with bench-top LQPIM optics based on twin machined concentric mirrors a second approach was also developed by placing LCAs in the arms of a Michelson interferometer based PSM. The optimised LCAs, efficiently separates, reshapes and minimises the cross-talk between the scattered and non-scattered image light fields at the Fourier plane and hence, renders a high contrast interference image at CCD camera. In this case, good phase resolution was acheived by mimicking the precise physical size of the annular ring and the phase plate available in condenser and objective lens of a commercial PCM. The PSM available in both LQPIM optical approaches provide a flexibility to implement any number and magnitude of phase steps and hence, the phase map of the objects can be reconstructed efficiently using any PSA reported in the literature.

- **Assessment of LQPIM system by utilising optical and biological samples as a proof of concept.** The PSAs simulated and evaluated for making phase measurements from thin and thick optical samples are demonstrated experimentally using LQPIM system. Based on the captured number of phase-shifted interference intensity frames at CCD camera, 2D and 3D phase maps of an NBS 1963A Test chart were obtained as well as from epidermis cells of *Allium cepa*. The phase maps enable the microscope performance to be evaluated in term of the spatial resolution and noise in phase measurement. The assessment was done under broadband green light illumination from a light emitting diode (LED) and a narrowband laser. Interestingly, an LED illumination gave better phase resolution (i.e. 0.318 nm) due to short coherence length

(≤ 8 nm), broadband (FWHM - 42 nm) and speckle noise free illumination compared to a narrowband laser illumination (i.e. 0.521 nm). The comparative assessment of phase noise and phase resolution by various PSAs was also performed and an example data from the biological samples are reported.

1.4 Thesis direction

The thesis has been structured in six Chapters (1-6). Chapter 1 gives brief information on contrast generation using fluorescent labels in microscopy sample preparation to study structural organisation inside biological cells and their potential benefits and drawbacks. It also explains (in brief) imaging cells without stains, i.e. label-free imaging to see the same structural features without perturbations in the cellular environment. A motivation and the original contributions in phase imaging microscopy were presented.

An introduction to phase imaging microscopy methods is presented in Chapter 2. The advancement in the optics, camera sensor technology, and measurement techniques are described leading to the development and implementation of phase imaging methods. The phase images provide valuable insight about transparent cellular and subcellular dynamics of the live cells. The optical path difference encoded in the phase images can be retrieved using PSAs to address the requirements for quantitative data from biological specimens. Furthermore, the limitations associated with each imaging method were also outlined in their respective section description. The chapter also gives an information about the principle used in phase shift interferometry to encode and retrieve phase experimentally.

In Chapter 3, an impact of biological objects on the illuminating wavefront is presented. To show the impact mathematical models are developed and a description of models is presented. An optimal solution for imaging optically thin (≤ 250 nm) and thick (≥ 1250 nm) cellular and sub-cellular biological structures of interest is also discussed. The simulations were performed to identify the best solutions for imaging phase objects as a function of bandwidth (1 - 250 nm), central wavelength (450 - 650 nm) and a suitable PSA. Chapter 3 also presents an optimum PSA for imaging both optically thin for example a monolayer of cells and thick biological samples, for example multilayer of cells such as 3D cell colonies.

In Chapter 4, the working principle behind the flexible LQPIM system and its implementation using standard and low-cost optical components are described. The system is capable of quantitative phase imaging in a non-contact, non-invasive and label-free manner from the biological samples. Using the LQPIM optics, phase-shifted interference intensity images, as needed by a PSA, were captured to produce wrapped and then unwrapped phase distributions from objects in the sample to confirm the expected performance predicted from the simulation experiments (Chapter 3). Two LQPIM optical system are described for imaging phase objects. In both cases, a custom inverted microscope was coupled with a PSM to encode a predefined sequence of phase steps into the non-scattered image field with respect to scattered image field before rendering an interference image at CCD camera. The first LQPIM optical approach was developed based on twin concentric mirrors in a common path arrangement (Section 4.5.2) and the second module uses a non-common path optics by employing laser-cut apertures in the PSM to mimic the phase plate and annular ring inside a phase imaging microscope (Section 5.2). LCAs applied in the arms of a Michelson interferometer produces good contrast interference intensity image by minimising the cross-talk between the scattered and non-scattered image light fields in the Fourier plane. Thus, there is an opportunity to deliver mostly 'halo artefact' free images [49].

In Chapter 5, the optimisation of physical size of the LCAs to mask precisely the phase plate and annular ring is outlined. The assessment of LQPIM system to measure the phase and render quantitative phase maps from optical samples, for example the NBS 1963A Test chart, glass beads and epidermis cells of *Allium cepa* will also be presented. The phase resolution will be quantified and the ability to measure large optical path differences is presented by means of measuring glass beads (diameter, 10 - 30 µm). The assessment of LQPIM system was performed under broadband green LED (FWHM – 42 nm), a very broadband LED (FWHM – 250 nm) and a narrowband (FWHM – 1 nm), for example a green laser source.

In the concluding Chapter 6, the contributions linked with developed flexible LQPIM system are presented in the context of existing QPI methods. Future research prospects and discussion of future research is outlined. Since, the LQPIM is a flexible system, it can be potentially transformative with multiple opportunities for users in the field of cell biology and biomedical applications.

Chapter 2. PHASE IMAGING MICROSCOPY

The developments in light microscopy optics over the last 75 years have revolutionised the understanding of cellular and subcellular structural organisation of tissues and cells. Dark-field microscopy was the only method used for many years to visualise transparent biological objects by generating contrast [a]. The extraction of the structural features and cellular dynamics from unaltered live biological samples was very challenging before the introduction of PCM by Zernike in 1935. Furthermore, a holography microscopy method [50] was proposed based on phase altering information exploited by Zernike. The ideas of phase and amplitude allowed researchers to image thin transparent biological objects precisely to elucidate cellular and sub-cellular structural dynamics qualitatively. However, methods that are more robust are needed to record fast moving cellular and sub-cellular events and processes in real-time for quantitative analysis.

In 1955, Francis Smith introduced DIC microscopy a label-free imaging method for examining transparent biological specimens [51]. The technique was further refined by George Nomarski to produce aberration-free high-resolution phase images by converting phase variations into contrast through the principle of interferometry [13], [52]. The label-free imaging methods have been developed in past years to image biological structures that do not

---

[a] https://www.microscopyu.com/techniques/phase-contrast/introduction-to-phase-contrast-microscopy. Accessed on: 10/07/14

absorb illuminating light significantly, hence, remain transparent under ordinary microscope, for example bright field microscopy. The imaging methods have been improved in their optical setups to image transparent biological samples with more contrast by altering the intensity of the illumination light beyond that which occurs due to absorption. The cellular and sub-cellular structures can be considered as phase objects that primarily alters the phase of the illuminating wavefront. When illumination light is projected onto a biological specimen refraction, diffraction and scattering occur due to the spatial variations in thickness and refractive index between the surrounding fluid and the cellular and sub-cellular structures [52]. The spatial variations can advance or retard the phase of the illuminating light passing through them.

Phase altering objects can be imaged with specialised optics by converting phase variations into intensity variations, for example as in the case of PCM. The phase change $[\Delta\varphi(x,y)]$ by cellular structures can be characterised by a phase function which is directly proportional to the optical path length difference (OPD) or the optical thickness of the objects in the specimen. The OPD function depends on the spatial variation in refractive index across the objects $[n_o(x,y,z)]$ in the sample with respect to the background $[n_b(x,y,z)]$ and variable thickness $t(x,y)$ along the optical axis as per Eq. (2.1) and Eq. (2.2).

$$\Delta\varphi(x,y) = \left(\frac{2\pi}{\lambda}\right) \times OPD(x,y) \tag{2.1}$$

$$OPD(x,y) = \frac{\lambda}{2\pi} \int_0^{t(x,y)} \left(n_o(x,y,z) - n_b(x,y,z)\right) dz \tag{2.2}$$

where $\Delta\varphi(x,y)$ is the phase change and λ is the wavelength of an illumination source. The spatial variations in refractive index, thickness across the specimen and high frequency objects produces high contrast interference image. However, the contrast quality can be affected by non-uniform illumination, the structures available in the sample, their morphological features and how the light enters and moreover, leaves the cellular and sub-cellular structures.

In general, the biological specimens can generate two types of contrast, for example, exogenous (outer appearance) and endogenous (inner appearance) and both can be exploited by optical microscopy methods. The external appearance of the biological structure or a specific organelle can be exploited by tagging a fluorphore molecule to it, for example a GFP tagged molecule produces an exogenous contrast [53]. The British scientist Sir George G. Stokes has coined the term ‘fluorescence phenomena’ in 1852 to refer to emission from a fluorophore at longer wavelengths than that of the excitation and since then the developments in optical components and instrumentation lead to advancement in fluorescence microscopy methods because of the significant contrast obtained. Furthermore, the discovery of GFP has enabled researchers to image the cellular and sub-cellular structures precisely [5]. The genetically modified GFP tagged cells are allowed to express GFP naturally with the defined cellular structure to convert exogenous contrast to intrinsic contrast. There are several applications in biological science where fluorescence microscopy has been applied to study the cellular structural organisation and mechanics using exogenous contrast. Epi-fluorescent methods became very popular because of the high contrast available - typically using a specific wavelength of illumination tuned to the absorption of a fluorophore label present or added to the sample [b]. The light emitted by the fluorophore at a longer wavelength requires colour filters to efficiently separate from the illumination and hence, giving a high contrast image of fluorophore labelled objects. The remarkable achievements in fluorescence microscopy due to the discovery of molecule-specific fluorescent markers still have several well-known disadvantages, for example photo-bleaching, photo-toxicity to healthy cells, high cost of fluorescent dye and the necessity of excitation, beamsplitter and emission filters to isolate the fluorescent signals (typically £1.5-2k per filter set plus fluorophore and sample preparation time). Additional information can be obtained beyond that available from widely used epi-fluorescent microscopy methods such as confocal, multiphoton and stimulated emission depletion microscopy [54]. Furthermore, due to the above-mentioned potential disadvantages of labelling molecules the label-free methods can be a preferred choice to render observations of cellular physiology in the native environment.

In label-free imaging, no special preparation of the sample is needed and the contrast achieved may be either extrinsic or intrinsic. The intrinsic contrast is a natural property of the biological cellular and subcellular structures due to small variation in spatial parameters, for example index of refraction and thickness. The living cells holding cellular and sub-cellular structures are optically translucent and dense with discrete spatial properties. The small spatial variations reduces speed of illuminating light waves passing through them compared to the light passing through the surrounding medium. The difference in speed makes a bend in the uniform

---

[b] https://www.microscopyu.com/techniques/fluorescence/introduction-to-fluorescence-microscopy. Accessed on: 11/07/2014

wavefront that illuminates the objects in the sample. The change or delay in the speed of illuminating wavefront corresponds to a change in phase (Figure 2.1).

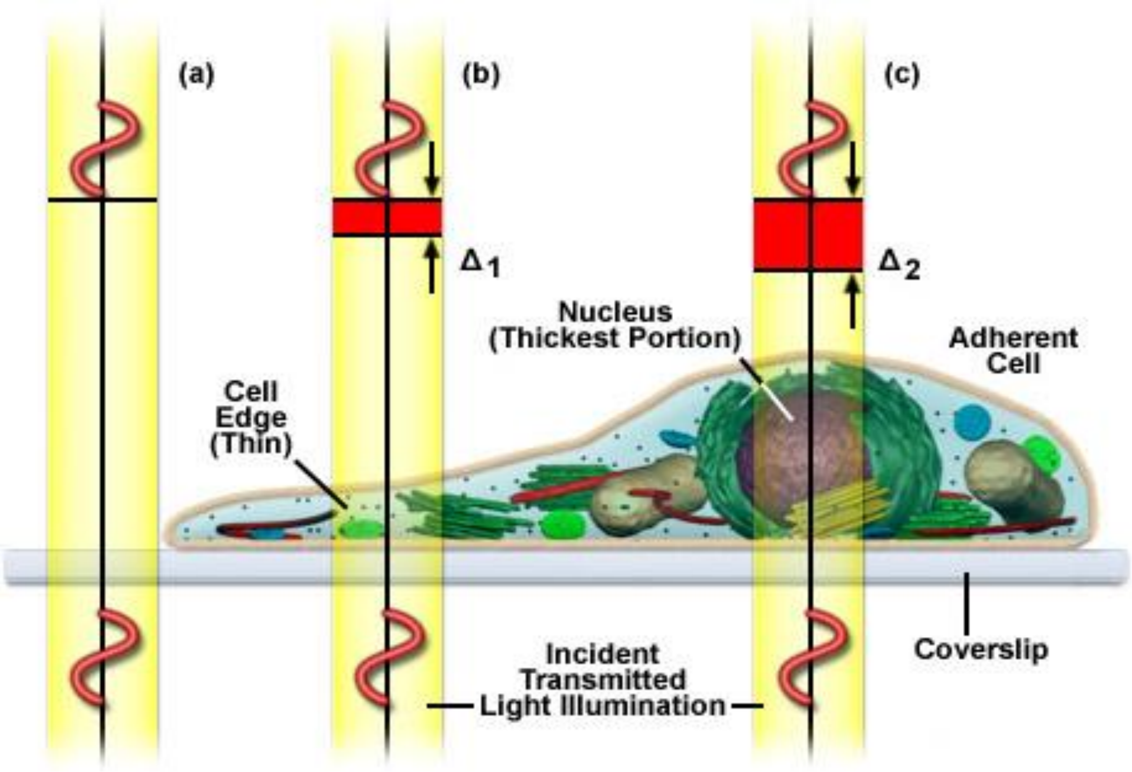

Figure 2.1 Phase-contrast imaging of semi-transparent thin object [c]

Figure 2.1a, no significant delay can be seen in light waves passing through the surrounding aqueous medium and the glass coverslip. However, a small delay can be seen when the wave passes through the aqueous medium surrounding the cell, between the cell wall and the cytoplasm (Figure 2.1b). Furthermore, a significant delay in light wave can be seen when it passes the thick part of the cell where the nucleus is present due to differences in the index of refraction (Figure 2.1c).

To exploit an intrinsic contrast generated by the translucent biological specimen remains a significant challenge in the field of light microscopy. Phase contrast techniques provide good contrast image utilising an interference phenomenon of two waves [55] passing through the specimen and meeting at image plane. Zernike developed PCM in 1930s by utilising two-wave interference phenomenon. In PCM, the contrast is generated by scattered and non-

---

[c] http://zeiss-campus.magnet.fsu.edu/articles/basics/contrast.html, Accessed on: 15/06/2014

scattered decomposed image light fields from the sample after inducing a relative phase shift of quarter wavelength and matching their relative amplitude at the image plane [8] (Figure 2.2 and Figure 2.3). The use of a quarter-wave retardation between two waves generates a mid-range intensity where sample induces a phase change to produce brighter or darker regions depending on value of index of refraction via interference at the image plane (Figure 2.3). In the case of bight field microscopy, the above image structure details would be faint and not very clear so not suitable for qualitative or quantitative inspection. The phase contrast image thus obtained is a “diffraction limited, nonlinear and qualitative interference intensity image”, therefore, quantitative phase information cannot be retrieved directly. PCM has enabled high contrast imaging of weakly scattering biological specimens without need of labelling. The internal cellular and sub-cellular objects produces scattered image light field carries structural detail in it’s amplitude and phase. The varying refractive index property of biological structures has been utilised by several researchers to measure phase delay, thickness of objects by converting phase data into thickness, dry mass and volumetric measurements [21], [37], [38], [56]–[58] by the implementation of pioneering ideas of Abbe, Zernike and Gabor. Some of the QPI methods are reviewed in Section 2.1.

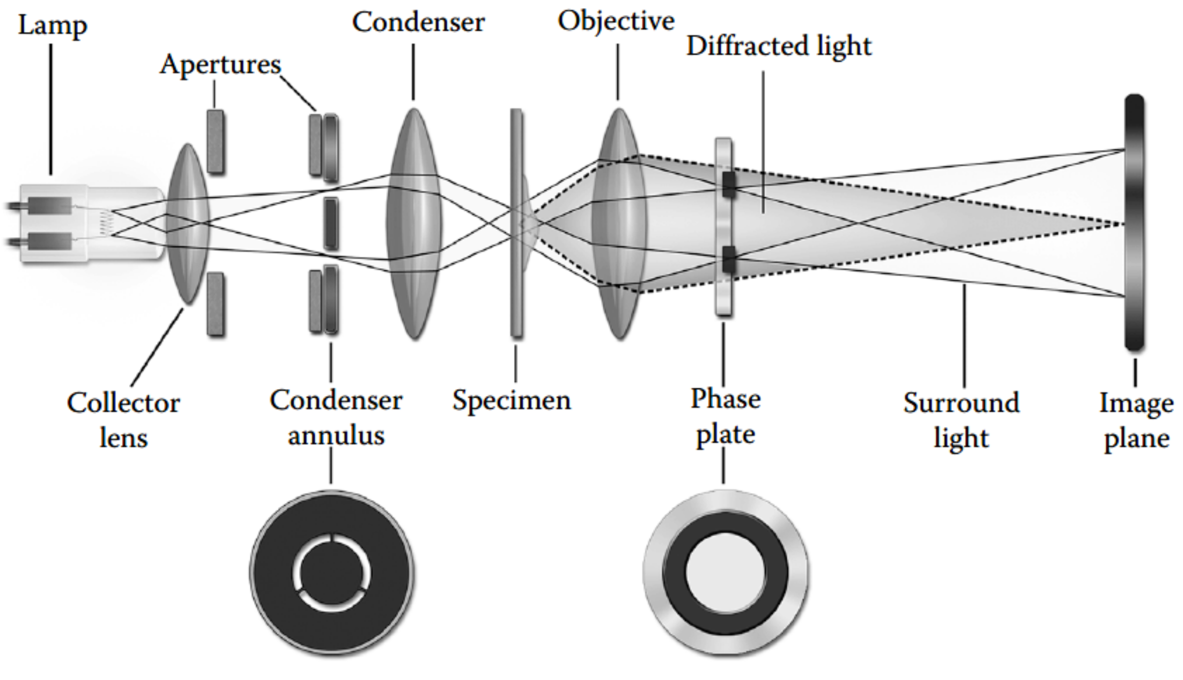

Figure 2.2 Optical train for phase contrast imaging [d].

---

[d] https://www.microscopyu.com/techniques/phase-contrast/introduction-to-phase-contrast-microscopy. Accessed on: 02/08/2014

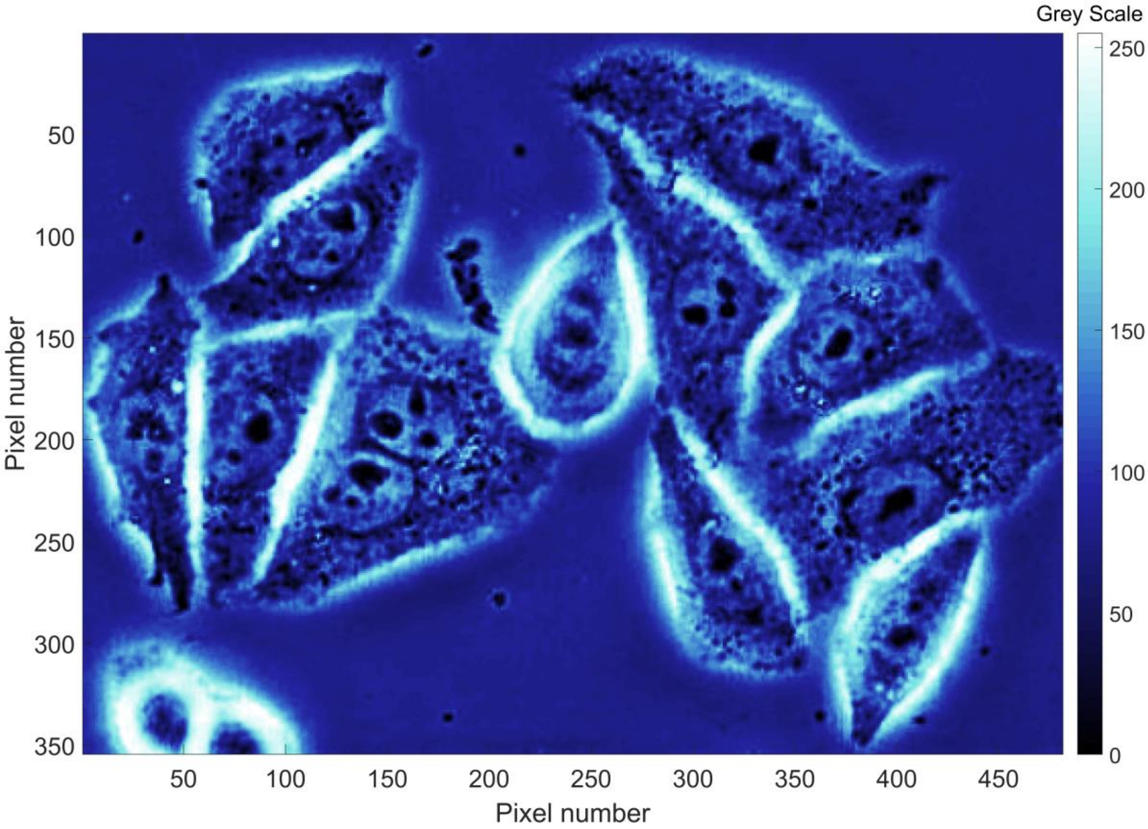

Figure 2.3 HeLa cells cultured on a glass coverslip imaged via a PCM [e].

2.1 Quantitative phase imaging

The QPI of the fast moving and changing cellular and sub-cellular objects can be of great importance to study the dynamics of cellular behaviour, effect of drugs and toxins, structural translocations, and to enlighten several biological questions regarding the cell cycle. Recently, researchers have combined PCM with QPI with an aim to apply this technique for quantitative, non-invasive and *in-vivo* studies of blood cells, HeLa cells and many more [14], [59], [60]. QPI method utilising Zernike's PCM concept and Gabor's holography approach are capable of rendering phase maps from the weakly scattering objects [16]. Full-field imaging techniques can provide a benefit of good spatial-temporal sensitivity to image biological samples. The interferometric measurements can provide an opportunity to render both quantitative and qualitative information from biological structures. The local thickness and refractive index of transparent structures both affect the OPD and can be measured dynamically using QPI techniques [61]; with thickness data obtained when there is independent information on the refractive index of the biological entity under examination.

---

[e] https://www.microscopyu.com/gallery-images/hela-cell-culture. Accessed on: 02/08/2014

However, these techniques are not sufficient to image multilayer cell cultures that induce larger scale optical path difference [62], for example 3D colonies. The CPI-based QPI techniques have shown superior stability for long-term phase measurements over the field of view without the need of faster scanning [14], [15], [63]. QPI schemes described in the literature are constrained to the assumption of a planar reference wave [64] which limits an accuracy at the operational field of view. Several QPI methods specifically for microscopy have been developed in recent years. Some of them are presented below.

2.1.1 Digital holographic phase microscopy

In 1948, the understanding of phase information enabled development of holographic microscopy [50]. Since then, the advancements in existing techniques have provided a suitable approach to quantify phase maps precisely [22], [41], [65]. Cuche et al. introduced digital holographic microscopy (DHM) for the first time in 1999. The intensity images recorded by DHM can be converted into holograms (the outcome of phase and amplitude reconstructions) of the objects using the Fresnel method to reconstruct the phase map from the sample [66], [67]. An advancement in charge-coupled devices (CCDs) camera and high-speed computers have enabled researchers to quickly record the necessary images to reconstruct holograms [68]. DHM has been successfully applied in biological sample analysis with 2° - 4° phase accuracy compared to optical coherence tomography [22] (will be reviewed in Section 2.3). The stray reflections from optical components, noise hosted by optical setup and dust on the sample slide can limit the achievable resolution. In general the reference and the object beams follow separate paths, therefore, can be affected by mechanical and temperature fluctuations and are susceptible to fringe order ambiguities due to air perturbations. Researchers have also tried off-axis configuration for DHM but failed to produce the best lateral resolution due to an angle between the reference and the object beams.

2.1.2 QPI methods based on off-axis optics

In this case, the reference beam is commonly tilted with a known off-axis angle and can be combined with object beam using a Michelson interferometer at the Fourier plane to form a phase-shifted interference image. The final quantitative phase map can be recovered from the recorded single intensity interference pattern using a Hilbert transform [69] or the Fourier domain demodulation [68]. Furthermore, an off-axis QPI method with laser illumination through a single mode fibre has also been demonstrated with full spatial coherence known as diffraction phase microscopy (DPM) [70]. In this method, a diffraction grating was used to generate multiple diffraction orders at the image plane of the microscope. The spatial separation of 0^{th} (low pass filtered) and first-order diffraction (non-filtered) was done in the Fourier domain via a pinhole or an SLM to achieve a common path optics. The two beams are combined to form an interference image that may be used to render a phase map from objects. The temporal resolution can be maximised due to use of a single interference image, but, the spatial resolution can often be limited by an off-axis angle and there are limitations on the slope of the object phase variation so as not to violate an assumption of increasing phase across the interferogram. It is particularly problematic in recovering phase maps from high frequency spatial phase objects, such as, the edges of cells where the phase gradients are very high (Chapter 3, Section 3.2).

2.1.3 QPI methods based on common-path optics

In the optical arrangement where the reference and the object beams travel the same path to form an interference image at the image plane is known as common-path optics. Fourier phase microscopy (FPM) is an example of common-path optics for the application of phase shifting to PCM [14]. In FPM, the reference image field was projected onto an SLM to create a sequential set of phase shifted interference images at CCD camera. The recorded images can be utlised to reconstruct phase maps of the cells to study membrane growth and fluctuations at nanometre scale with high temporal sensitivity and stability [70]. Most of the QPI methods including FPM use temporally coherent illumination (i.e. a narrowband laser) and hence, the speckle noise degrades contrast quality of the image [71]. However, CPI enables cancellation of noise and mechanical vibrations from the optics and hence, better for long-term monitoring of a biological samples. Common path configurations can be combined with either phase stepping or for single image acquisition by using a grating or an SLM under a suitable optical design [40]. Recently, a common path DPM with phase shifting using an SLM has been implemented to achieve good lateral resolution [15]. However, the average field cannot be optimised due to the fixed size of a pinhole in the centre of the SLM that generates the reference beam. The quantitative phase map can be reconstructed based on the scattered and non-scattered image fields that restrict the alignment of DPM optics with reasonable accuracy. This approach is not considered appropriate for this project due to the high cost of the components required, the complexity and time needed for the phase reconstruction algorithms and the compromise required with a fixed central pinhole. The single shot acquisition and common-path capability provides stable phase measurement and was most commonly applied at high magnification to reduce the phase gradients, e.g. 40x was used by Ding and Popescu

(2010), and has been exploited to render blood cell membrane dynamics and mechanics at scale [72].

2.1.4 QPI methods based on white light illumination

The microscopy methods with narrow-band (laser-like) illumination suffer from significant levels of speckle noise, which limits both the lateral image resolution and the ability to recover phase maps around the edges of the cells due to large steep gradients [67]. Broad bandwidth illumination can significantly reduce the generation of speckle noise. Therefore, many research groups have started utilising the broadband illumination to mitigate the speckle noise from their experiments, but at the same time, this introduces errors in the applied phase shifts (analogous to phase shift miscalibration errors) which primarily rely on the use of a single narrowband laser like-source. In recent years, DPM has been updated to use a broadband (white) light source in a reflection geometry to image biological samples and hence, offers lower noise compared to narrowband laser sources. Previous versions of DPM do not match high resolution and noise to contrast ratio due to the speckle generated by high temporal coherence of the laser illumination [15]. Furthermore, these methods well suffers from speckle noise and the reduced sensitivity in phase map reconstruction from transparent biological objects. The common path optical setups using white-light illumination has enabled researchers to achieve stable phase measurements from biological samples [26], [30]. For example SLIM developed by Wang et al. in 2011 has gained much attention due to the well-known advantage of common path optics and the use of white light illumination (WLI) to study the dynamics of label-free biological samples [29]. In previous works [14], [21], [73], [74] the phase resolution performance of a QPI has been re-scaled from units of radians into wavelength (nm) by applying a scaling factor of $\lambda/(2\pi)$ where the wavelength chosen corresponds to the centroid of the illumination spectra. This convention is adopted throughout this thesis. SLIM produced a phase resolution (scaled into nm) of 0.3 nm spatially and 0.03 nm temporally using a short-coherence illumination source that produces speckle-free imaging. However, in the context of microscopy, the spatial resolution of SLIM is limited by diffraction and aberrations [75] because it can’t take an advantage of the full numerical aperture of the condenser lens due to a much smaller size of illumination annular ring. Only 12.5 frames per second acquisition speed has been possible to record dynamics of fast moving biological objects [76], [77] limited by the hardware available in those experiments.

The use of WLI has improved the spatial sensitivity of SLIM [29] and off-axis based white-light diffraction phase microscopy (wDPM) [78]. wDPM can tolerate an object phase distribution with a lower space-bandwidth product due to the requirements of Hilbert transform phase analysis and hence, can only preserve the resolution at the expense of field of view [71]. White-light diffraction tomography (WDT), a label-free tomography method to image live cells, suitable to incorporate as an addition to conventional microscopy setups can only examine single cells up to 20 µm thick [30] and an optical path differences ≤ 240 nm. Furthermore, in the context of tomography method, the penetration depth is smaller and it should be possible to go much deeper into scattering tissues. Until today, none of the quantitative phase label-free microscopy methods are available to study organotypic cell cultures, where penetration depth or long optical path measurements are of critical interest.

2.1.5 Phase shifting mechanism applied to PCM based QPI methods

A number of phase-shifting mechanisms have been exploited in PCM based QPI methods using several optical components, for example a wave plate, rotating polarisers, PZT and an SLM. Typically, a standard Michelson interferometer can be used in the back focal plane of the microscope for spatial separation between the scattered and non-scattered image light fields and a pre-defined phase shift is introduced using any of the above-mentioned optical components. In most cases, the phase shifts are introduced sequentially to generate a temporal series of interference images from which phase variation induced by objects can be extracted by applying a trigonometric relationship. The method is simple in design with improved spatial resolution; however, if the phase-shifted images are generated using a grating then a difficulty arises in registering the different images onto a common set of pixel coordinates in order to calculate the wrapped phase. The phase sensitivity may be controlled by matching the relative power of the scattered and non-scattered beams to provide a reasonable signal to noise ratio [79]. Despite the simple design and good sensitivity, the acquisition speed is limited, as multiple frames are needed per interference image. Furthermore, use of laser illumination optics introduce speckle noise and non-common path optics provides sensitivity to spatial and temporal variations. Air turbulence and mechanical vibrations can perturb the phase shift introduced in this manner can be mitigated by providing a shielding box to cover the interferometer optics [80] or adopting common path optics as discussed in Section 2.1.3. Speckle noise can also be largely eliminated by use of WLI [43].

2.2 Phase imaging optics for dynamic events

In standard interferometer based microscopy methods, the acquisition speed of the imaging system is limited due to the number of sequential interference frames to be captured by the

CCD camera to render a phase map. The alternative is to use an off-axis reference wave and Hilbert transform analysis, however, as discussed above, this imposes limits on phase gradients and hence drives towards higher magnification especially when dealing with biological entities, such as cells. Biological processes runs faster compared to several hundreds of milliseconds, typically needed to record sequential measurements. To record and analyse such fast moving cellular dynamics proper vibration isolation and damping is required with high acquisition rate and spatial-temporal sensitivity to obtain high-quality data from moving objects. Dynamic interference microscopy (DIM) [81] has been developed to address such type of quantitative analysis in a label-free manner. The phase map from cells and cellular structures can be rendered robustly from a single image from DIM using a Linnik interferometer and a pixelated polarisation phase masks technology [81]–[83].

The approach relies on 4D Technology pixelated micro polariser-based camera, where a polariser mask is bound to the camera sensor [82]. A 2x2 grid of pixels receives a set of four phase-stepped intensities in which the polariser in front of each pixel is rotated by 45° with respect to each other. This results in four phase stepped intensity measurements with relative phase shifts of 90° suitable for direct calculation of the interference phase. The approach relies on the sample not varying significantly over the 2x2 grid pixels that is referred to as either a cell or a super-pixel. The configuration of phase steps from the pixelated phase mask are fixed with a significant cost to develop the masks, hence, this method is fixed to 4F@90° PSA. Furthermore, the magnification must be set according to the sample to minimise high phase gradients across each super-pixel.

The limitations of QPI methods for measuring thick biological samples are due to two main reasons. First, the illumination spectrum has not been optimised in past for the quantitative phase measurement. The use of narrowband laser illumination in QPI images produces images with speckle noise due to high temporal coherence that never match the contrast exhibited in white light techniques such as those from qualitative PCM and Nomarski diffraction microscopy [9]. The alternative is the use of broadband illumination, typically from thermal sources or white-light LEDs, and whilst this form of illumination can provide low levels of phase noise, measurements over large optical path differences ($\geq$ 1250 nm) have not been reported. The question of imaging thick organotypic cells (can be described as large volume of cells) using tomographic and/or phase microscopy still need to be addressed. Secondly, the experimental setup of QPI tends to be complex, utilise high-cost components and/or needs high maintenance. Quantitative phase microscopy has been shown to have the resolution necessary to find cellular and sub-cellular organelles and tissues. However, the high-resolution instruments developed so far based on QPI approaches have been restricted to a limited field of view [84] and cannot be applied for inspecting large regions of interest. Importantly, to find cell-to-cell contact inhibition processes the phase gradient at the edge of a cell is sufficiently large that accurately finding cell boundaries is expected to be feasible. Therefore, the potential is apparent to quantify the typical phase profile of a cell and apply quantitative phase microscopy to measure the phase profiles from single cell layers and multilayer cultures, as required to experimentally examine the full range of cell differentiation and regeneration phenotypes that exist, for example urothelial cell layers in the bladder [85].

2.3 Optical coherence tomography

Optical coherence tomography (OCT) can be an alternative technique to image biological cells and tissues in label-free manner [86], [87]. 3D maps of tissue *in-vivo* can also be possible using this technique. OCT uses a low temporal coherence broadband source to image tissue samples with a technique known as low-coherence interferometry [88]. 3D structural information can be rendered by OCT systems from the recorded intensity measurements of the backscattered light fields. The fundamental technique produces one-dimensional data along the path of an illuminating beam based on reflectance from a scattering medium (or tissue) with the depth localised by the coherence length in a Michelson interferometer optics [89]. The axial resolution can be achieved by the coherence length of the illumination source, typically down to a few microns along the beam axis and the numerical aperture (NA) of the imaging system determines the lateral resolution [90]. 3D data can be obtained by rapidly scanning the illuminating beam over two axes to render 3D volumes at conventional video rates (10’s of frames per second). The axial resolution at a few microns is approximately 1000x worse than that achievable from phase-stepped interferometry and therefore, OCT is not appropriate for detailed cellular and sub-cellular structure analysis. Furthermore, the resolution from OCT worsens with depth into the tissue.

2.4 Phase shift interferometry in microscopy

Speckle interferometry is a widely used technique to measure pressure displacement [47], strain and surface profiles of the test objects [44]. The phase information from the object of interest is extracted using phase-shiftted images. Michelson interferometer can be used to generate a defined phase shift in the reference beam compared with the object beam. The irradiance distribution of the interferogram produced by the superposition of the two beams can be recorded at the CCD camera to reconstruct a phase map using a suitable PSA. The phase is typically calculated using an inverse tangent function and hence, phase values are wrapped in the interval - π to +π. A suitable phase unwrapping algorithm need to be applied to give a contiguous phase distribution for the objects as appropriate [91], [92]. The fringe pattern formed from the two beams must be sampled correctly to reconstruct the wavefront of the test object. A conventional assumption is for the fringe pattern to be sampled with at least two pixels per fringe to enable a phase profile to be reconstructed correctly. Three or more phase-stepped images are needed to calculate phase distribution at each pixel independently. The change in phase can be used to monitor the morphological variations or displacement in the object. Arbitrarily large (≥ 1500 nm) deformations can also be measured from rough optical specimens provided there is sufficient coherence length and the interference patterns are sufficiently sampled spatially. In speckle interferometry, phase noise induced by the speckle pattern generated in interferometer is the main drawback [93]. PSI techniques have been applied to several optical applications, for example speckle interferometry [44], [93], holographic interferometry [41], [65], [94], quantitative phase microscopy [16], [42], [95] and differential interference contrast microscopy [96]. Furthermore, PSI has an advantage of automatic phase determination over a full sample area and provides independent phase values for each pixel. Uncertainty can arise in the calculated phase values due to instability in the phase step, mechanical vibrations and environmental perturbations [25]. However, these effects can be mitigated if the measurements are taken in short time intervals (<10 - 50 ms), using a proper shielding around interferometric optical components to stabilise the interferometer and applying vibration damping under experimental area.

2.4.1 Phase measurement techniques

In PSI, the phase difference can be generated by translating a reference mirror along the propagation direction of the incident wave. The fringe modulation can be a fundamental problem due to under-sampling, mechanical vibrations, and nonlinearity in phase shifter [25]. Many PSI techniques [97] have been published to date, where, some used a defined phase step between intensity measurements (i.e. PSI) and others integrate the intensity (i.e. integrating-bucket technique) while the phase is changed in constant manner. The number of measurements of the intensity at the detector may vary as per required by a PSA. A minimum three intensity measurements are needed to determine the phase change from test object using two-beam interference as expressed in [98] as per Eq. (2.3).

$$I(x,y) = I_0\left[1+\gamma\cos(\Delta\varphi(x,y)-\varphi')\right] \tag{2.3}$$

where $I(x,y)$ is the intensity recorded at the detector, I_0 is the DC component of the intensity, γ is the fringe visibility, $\Delta\varphi(x,y)$ is the desired interference phase and φ' is the applied known phase shift. Each of the terms on the right hand side of Eq. (2.3) depend on position on the detector in the same way as shown explicitly to the term on the left hand side. High contrast images can be produced if the fringe visibility $\gamma \approx 1$ $(0 < \gamma < 1)$ can be maintained. The fringe visibility of an interference pattern can be measured as per [99] using Eq. (2.4).

$$\gamma(x,y) = \frac{I_{\max} - I_{\min}}{I_{\max} + I_{\min}} \tag{2.4}$$

In Eq. (2.4), $\gamma(x,y)$ is the fringe visibility or modulation, I_{max} and I_{min} are the maximum and minimum intensity of the interference image. The graph in Figure 2.4 shows the fringe visibility as a function of the intensity ratio of the two interfering beams. Initially the fringe visibility drops rapidly as the intensity ratio deviates from unity but this decay levels out above an intensity ratio of about 20 as the denominator of Eq. (2.4) becomes effectively constant and the numerator depends on the square root of the intensity product of the two beams so reduces slowly as the intensity ratio becomes extreme.

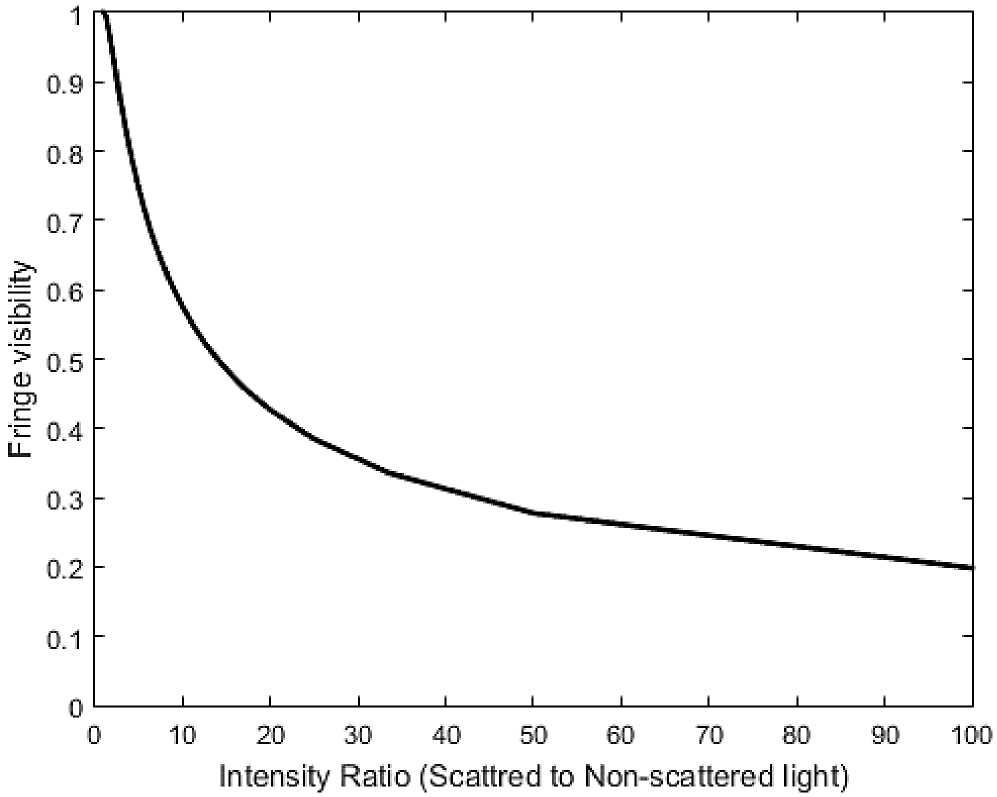

Figure 2.4 Fringe visibility inside an interference microscope.

Let one consider, the scattered $E_s(x,y)$ and the non-scattered E_{ns} with varying wave amplitudes having the same frequency (υ) and wavelength (λ) and both linearly polarised along the x-axis. The intensity of the superimposed interference image field produced by these waves can be written as per [100] using Eq. (2.5), where * indicates the complex conjugate.

$$I(x,y)=\left[E_s(x,y)+E_{ns})\right]\times\left[E_s(x,y)+E_{ns}\right]^* \qquad (2.5)$$

Further, an irradiance pattern on the camera can be measured using Eq. (2.6) after substituting $E_s(x,y) = A_s(x,y)e^{i\varphi_s(x,y)}$ and $E_{ns} = A_{ns}e^{i\varphi_{ns}}$ in Eq. (2.5).

$$I(x,y)=A_s(x,y)^2+A_{ns}{}^2+A_s(x,y)\times A_{ns}\left(e^{i(\varphi_s(x,y)+\varphi_{ns})}+e^{-i(\varphi_s(x,y)+\varphi_{ns})}\right) \qquad (2.6)$$

Further Eq. (2.6), takes form of well-known two-beam intensity equation after replacing amplitude (A^2) terms by intensity (I) term and solving for the complex fields.

$$I(x,y)=I_{ns}+I_s(x,y)+2\sqrt{I_{ns}I_s(x,y)}\cos\left(\Delta\varphi(x,y)\right) \qquad (2.7)$$

where $\Delta\varphi(x,y)$ is the phase value, $I_s(x,y)$ and I_{ns} are the intensity of the scattered and non-scattered image fields from a PCM. The two-beam interference is a key principle in PSI techniques. The phase modulation can be done in many different ways, for example moving a reference mirror [101], rotating a phase plate [24], rotating a polarizer [24], moving a diffraction grating [102] and using an SLM [103]. Moving a reference mirror using a PZT driven high precision linear stage technique was used in this thesis work to introduce the phase steps between the scattered and non-scattered image light fields in the LQPIM optics. The description of techniques is presnted in Section 2.4.2.

2.4.2 Moving a reference mirror for phase stepping

The phase of a beam can be altered by moving a mirror with the help of a PZT. It is the most commonly used method in commercial and non-commercial available interferometers, for example Michelson interferometer. In this process, a mirror is installed on a PZT driven high precision linear stage. The voltage applied to the PZT material controls the movement. The mirror displacement of λ/8 will produce a phase shift of λ/4 or equivalently π/2 radians if the beam of light is reflected at normal incidence. A schematic of the optical geometry to introduce such a phase shift (at mirror M_2) is presented in Figure 2.5. In Figure 2.5, the camera receives the reflected image from the mirror (M_1) as well as from the mirror (M_2) via the beam splitter. The superimposition of these images at the camera produces interference fringes. The phase-shifted images from the mirror (M_2) provide a way to vary the phase difference between these waves. The phase change thus introduced using an optical setup can be extracted using a suitable PSA, for example three frames or four frames at 90° or several other well-known algorithms [48], [97], [104]. A brief description of selected PSAs for evaluation in this project are presented in Section 2.5.

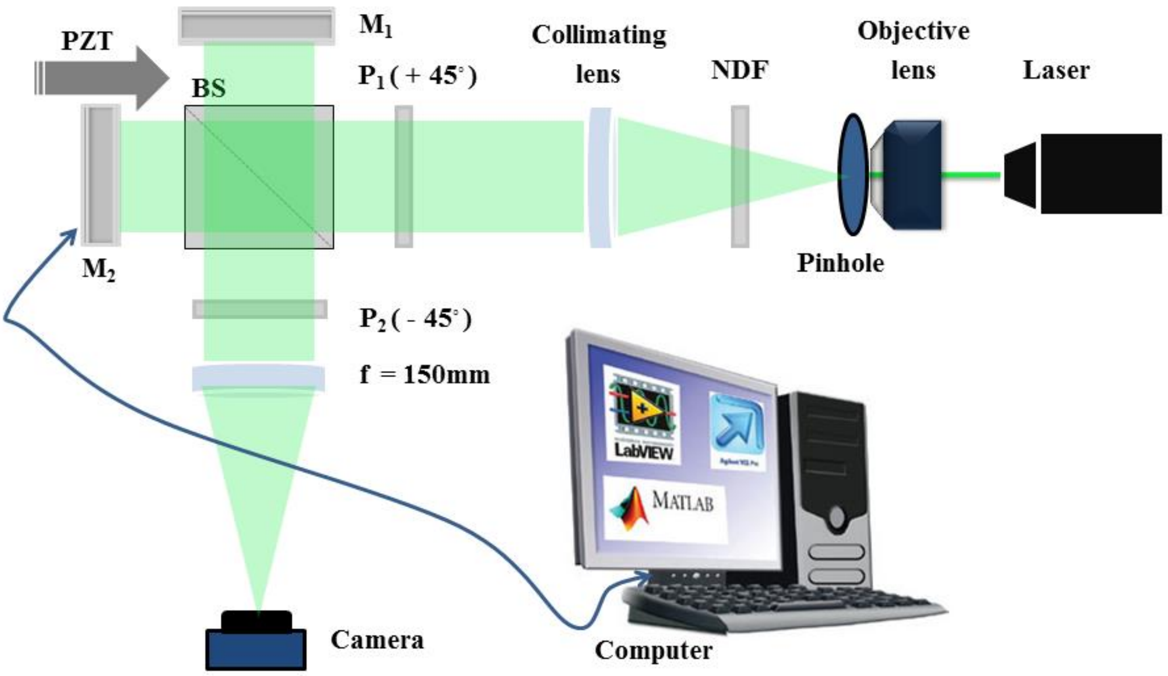

Figure 2.5 Schematic presentation of phase shift produced by a moving mirror; NDF (Neutral density filter), P_1-P_2 (Polarizer), M_1-M_2 (Mirror), BS (Beam splitter), OL (Output lens).

2.5 Phase extraction techniques

2.5.1 Three-frame technique

In a phase measurement experiment, only three interference images are needed to extract phase from the object under examination. Experimentally, a phase shift between 0 to π radians can be added to deduce the phase information from the captured interference images at the camera. The profile of the object can be measured using three frames at 90° (3F@90°) and three frames at 120° (3F@120°) PSAs as per [25] using Eq. (2.8) and Eq. (2.9), respectively. I_1, I_2, *and* I_3 are the phase-shifted intensity images in below equations corresponding to phase shifts of 0°, 90° and 180° for Eq. (2.8) and 0°, 120° and 240° for Eq. (2.9).

$$\Delta\varphi(x,y) = \tan^{-1}\left(\frac{I_1(x,y) - I_2(x,y)}{I_2(x,y) - I_3(x,y)}\right) \tag{2.8}$$

$$\Delta\varphi(x,y) = \tan^{-1}\left(\frac{\sqrt{3}\left(I_1(x,y) - I_2(x,y)\right)}{2I_1(x,y) - I_2(x,y) - I_3(x,y)}\right) \tag{2.9}$$

2.5.2 Four-frame technique

Although only three intensity measurements are required to solve PSI equation for the three variables, however, to reduce the systemic noise and sensitivity to phase stepper non-linearity more than three interference frames are often used. In general, a nominal phase step of $\pi/2$ (90°) is used to record the four-phase stepped intensity images to measure the phase profile of the surface as per [25] using Eq. (2.10), where, I_1 - I_4 are the phase-shifted intensity images.

$$\Delta\varphi(x,y) = \tan^{-1}\left(\frac{I_4(x,y) - I_2(x,y)}{I_1(x,y) - I_3(x,y)}\right) \tag{2.10}$$

$$\alpha = 2\tan^{-1}\sqrt{\frac{3(I_2(x,y) - I_3(x,y)) - (I_1(x,y) - I_4(x,y))}{(I_1(x,y) - I_4(x,y)) + (I_2(x,y) - I_3(x,y))}} \tag{2.11}$$

The mean phase step (α) applied between phase-shifted interference images can be checked as per [48] using Eq. (2.11).

2.5.3 Five-frame technique

Apart from the PSAs mentioned above, five-frame algorithms have also been reported in the literature to reduce the issue of residual errors and errors due to deviated value from the nominal phase step (i.e. $\pi/2$) [105]. Schwider et al. [106] have suggested a simple five intensity measurement algorithm at 90° phase step but, the residual errors and significant deviations in the mean phase step have not been quantified. In 1987, Hariharan et al. [101] further reviewed the algorithm and successfully optimised the calculation to be insensitive to low order detector nonlinearity and to compensate for significant deviations from the nominal phase step (i.e. 90° ± 5). The phase measurement based on five interference images can be a better choice if nonlinearity in the detector is present and can be retrieved using Eq. (2.12). Furthermore, an accuracy of the phase-shifted frames can be checked by measuring the mean phase step angle (α) as per [107] using Eq. (2.13), where, I_1 - I_5 are the phase-shifted intensity images in the given equations.

$$\Delta\varphi(x,y) = \tan^{-1}\left(\frac{-2I_2(x,y) + 2I_4(x,y)}{I_1(x,y) - 2I_3(x,y) + I_5(x,y)}\right) \tag{2.12}$$

$$\alpha = \cos^{-1}\left(\frac{I_5(x,y)-I_1(x,y)}{2\left(I_4(x,y)-I_2(x,y)\right)}\right) \tag{2.13}$$

2.5.4 Six plus one and other higher frame techniques

PSAs with higher number of intensity samples have also been reported in the literature for the white-light interferometry, for example Hariharan-Schwider five frames at 90° PSA [101], six plus one frame at 60° PSA [Eq. (2.14)] [108], [109] and seven frames at 90° PSA [Eq. (2.15)] [107], [110]. Shen et al. have also reported a nine and eleven frames at 90° PSAs with minimum simulated errors [111]. I_1 - I_7 are the phase-shifted intensity images in the given equations where 60° steps are used for Eq. (2.14) and 90° steps are used for Eq. (2.15).

$$\Delta\varphi(x,y) = \tan^{-1}\left(\frac{\sqrt{3}(I_2(x,y) + I_3(x,y) - I_5(x,y) - I_6(x,y))}{-I_1(x,y) - I_2(x,y) + I_3(x,y) + 2I_4(x,y) + I_5(x,y) - I_6(x,y) - I_7(x,y)}\right) \tag{2.14}$$

$$\Delta\varphi(x,y) = \tan^{-1}\left(\frac{4I_2(x,y) - 2I_4(x,y) + I_5(x,y)}{-I_1(x,y) + 7I_3(x,y) - 7I_5(x,y) + I_7(x,y)}\right) \tag{2.15}$$

From the literature, it is clear that most of the PSAs with higher numbers of frames are simulated using synthetic data but not on real time experimental data from biological specimens. PSAs such as 3F@90° and 4F@90° have been used to extract the phase distributions from biological samples (i.e. neuron cells) or optical samples (i.e. glass / polystyrene beads) in microscopy. The work in this thesis (which leads to a more flexible phase shifting module than for other forms of phase imaging microscope) enables a more general optimisation of PSA to be employed against bandwidth and centre wavelength of the illumination source and the time required to capture the data. Such an assessment has not been reported previously and the relationship between all these parameters is of interest to identify optimal solutions for quantitative phase microscopy.

2.6 Summary

A brief review of phase measuring microscopy methods such as DHM, off-axis methods, common-path interferometry, white light interferometry, DPM and OCT have been outlined in Chapter 2. Every technique has it’s own merits and drawbacks. The methods based on an SLM are generally better due to the ability to form a common path interferometer, but, the optical instrumentation is very expensive. Furthermore, an SLM needs to be calibrated for each PSA that going to be implemented with additional computational cost. Short coherence length illumination helps the SLIM method to produce speckle-free imaging at sub- spatial background noise. However, the spatial resolution of SLIM is limited by diffraction and aberrations [75] in the context of microscopy. The smaller illumination annulus aperture limits the utilization of the full numerical aperture of the condenser lens and hence, lowers the resolution. It can be seen from the literature that knowledge of the specific centre wavelength (λ), bandwidth (FWHM) of the illumination source and the respective PSA have not been studied or optimised. Therefore, computational models to explore these parameter space were developed and simulated in MATLAB and are discussed in Chapter 3.

Chapter 3. PHASE SHIFT ALGORITHMS FOR PHASE MEASUREMENT

The biological specimens considered in this thesis are mostly transparent optical objects, and hence, primarily a phase object as well as basic physical, structural and functional unit of life. All cells hold specific essential organelles, such as nucleic acids, ribosomes, mitochondria, Golgi complex and endoplasmic reticulum etc. necessary for the living cells. The mitochondria integrate multiple intracellular signals to regulate progression through the cell cycle as well as apoptosis. Therefore, mitochondria are vital to support functionality and to regulate healthy cell proliferation and prevent the development of abnormal cells. The cell is made up of protein, carbohydrate, lipids, salts and some other organic and inorganic molecules along with water. The inner details of transparent objects without staining or tagging can be imaged by PCM [8]. The phase contrast image of a cell is sensitive to minute optical path length changes down to the nanoscale; however, the information retrieved is only qualitative. QPI can quantify cell-induced shifts in the optical path and permit scale measurements of structural motions in a non-contact and non-invasive manner [60], [70]. Unlike PCM and DIC, QPI techniques also provide the significant advantage of quantifying optical parameters such as phase shifts introduced by cellular objects in the sample, a parameter that is related to the morphology and intracellular content of the cell [21].

3.1 Phase shift induced by the biological cell and cellular organelles

When a light wave passes through a medium, the wavefronts become retarded from their original positions due to the presence of a translucent object; such a displacement is termed a phase change or phase shift. The phase shift produced by a sample reflects the extent to which light wave propagation can be affected by the object present in the sample. The phases of the waves emerging from an object vary from in phase to out-of-phase as the thickness and composition of the sample (relative to the medium) varies. The degree to which the emergent light waves are out of phase i.e., change in retardation with respect to each other is termed a relative phase shift and can be expressed in radians.

The spatial variation in the refractive index can identify the cell organelles and biochemical changes inside the cells. The refractive index distribution of tissue is a high-end intrinsic marker of disease such as cancer and may set the basis for a new generation of computer-assisted label-free histopathology assays [35], [112], [113]. Techniques to quantify these distributions may enable earlier detection of disease and a correct diagnosis with high-sensitivity screening. When a light wave travels through a medium, the interaction with the medium induces changes in amplitude and phase of light depending on the properties of the medium. The scatter and absorption of the light are often wavelength dependent and hence, may give rise to colours and amplitude changes. The distribution of phase changes across a cell can be made visible as colour or intensity variations by interfering the transmitted light with another wave (i.e. reference). The phase shift produced by an object at an individual image point depends only on the thickness/height of the object at that point and the relative refractive index along the path of the wave that arrives at that point can be uniquely determined using mathematical expressions such as Eq. (2.8) to Eq. (2.15).

The morphological identification and phenotypic characterisation of living cells can be done based on variation in index of refraction between the objects and surrounding medium as well as the thickness [114]. The large distinguishable variations in optical thickness can be manifested by cellular structural organisation and morphological changes in cells and tissues. The living cell is a complex structure, which holds many organelles with distinct index of refraction and other optical properties. For example index of refraction for the plasma membrane, cytoplasm, mitochondria, lysosome and the nucleus are 1.48 [115], 1.36 - 1.39 [74], 1.4 - 1.42 [116], 1.600 [116] and 1.4175 - 1.485 [74], [117], respectively. Furthermore, the protein concentration within the cell mainly determines the effective refractive index of cells because it is present in significant amounts and has a high index of refraction 1.50 - 1.58

[115], [118]. Compared to healthy cells, cancer cells have more protein in the relatively larger nucleus to enable rapid cellular division which means cancer cells have a relatively larger refractive index than healthy cells due to the more considerable amount of protein [57]. For example in the case of breast cancer, healthy cells have an average refractive index of 1.385 while cancer cells have an average index of refraction about 1.399 ± 0.001 (the influence of temperature and other variables on the uncertainty obtained are considered as part of the analysis of results in this thesis, see Chapter 5, Section 5.5). The Lorentz-Lorenz mixing rule [119] provides a relation between water content and the refractive index of the cell and it’s organelles, that can be determined as per Eq. (3.1).

$$\frac{n_{cell}^2-1}{n_{cell}^2+2}=\left(\frac{n_w^2-1}{n_w^2+2}\right)\times\varphi_w(x,y)+\left(\frac{n_p^2-1}{n_p^2+2}\right)\times\varphi_p(x,y) \tag{3.1}$$

where n_w is the volume fraction of water, n_p is the volume fraction of protein, $\varphi_w(x,y)$ and $\varphi_p(x,y)$ are the phase change induced by water and protein, respectively. In cancer biology, it is well-documented that the refractive index of cancer cells is relatively higher than healthy cells. Therefore, some cancers can be diagnosed by the effective refractive index measurement of the cell as a quantitative indicator of cell malignancy [120].

3.2 Theoretical model for phase change by the biological structures

In general, the phase change is proportional to the integral of the refractive index along the optical path due to the varying thickness and optical properties of the objects in the sample. The spatial parameters for the refractive index and thickness variations have been considered in mathematical models simulated in MATLAB. In the model, it was assumed that monochromatic light illuminates the medium (ie. water) containing cells and other cellular structures, such as thin membrane, a nucleus (5 µm in size), mitochondria (approximately 1000 in number and 2 µm in size) and the cytoplasm surrounding all the structural components. The phase shift produced by cell organelles was analysed with respect to their index of refraction (mentioned in Section 3.1) and thickness. In the first case, a simple model of the cell with a thin membrane filled with cytoplasm was considered without any cellular organelles. In the second case, the model assumes a thin membrane, cytoplasm and the nucleus for the phase measurements and in the third case, the model considers all the cellular structural components including the nucleus, cytoplasm, a thin membrane and the mitochondria. The cell membrane and nucleus were assumed to be circular in geometry. An oval shape was predicted for the phase change by the cell membrane surrounded by cytoplasm in the first case (Figure 3.1).

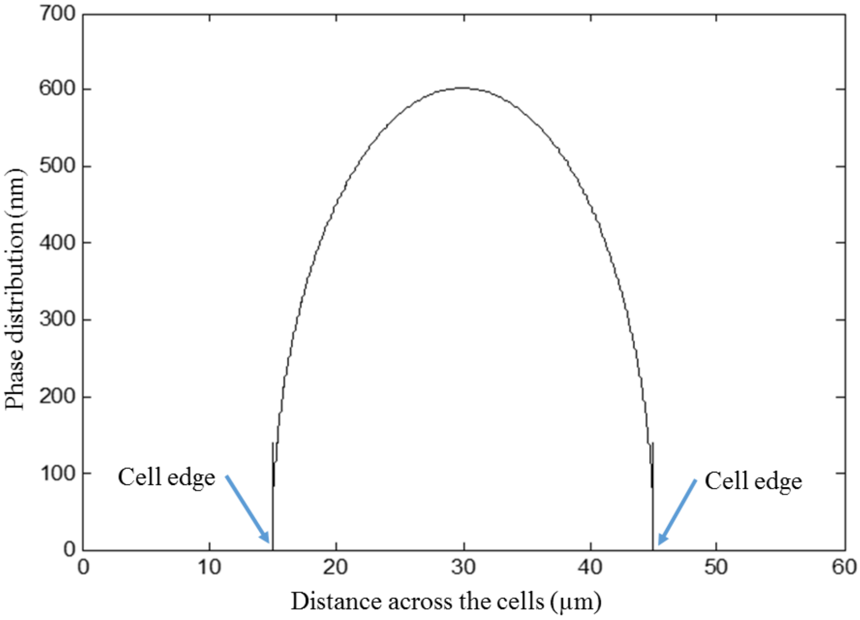

Figure 3.1 Phase distribution across the cell membrane

The phase distributions are given in nanometres with respect to the simulated illumination wavelength (λ, 530 nm), i.e. $\Delta\varphi\lambda/2\pi$. The peaks localised at either edge of the cell are due to the cell membrane's higher index refraction compared to the cytoplasm. Furthermore, an index of refraction of the nucleus is higher than the cell membrane and the cytoplasm and hence, a large peak for the phase change can be seen in the region of the nucleus (Figure 3.2).

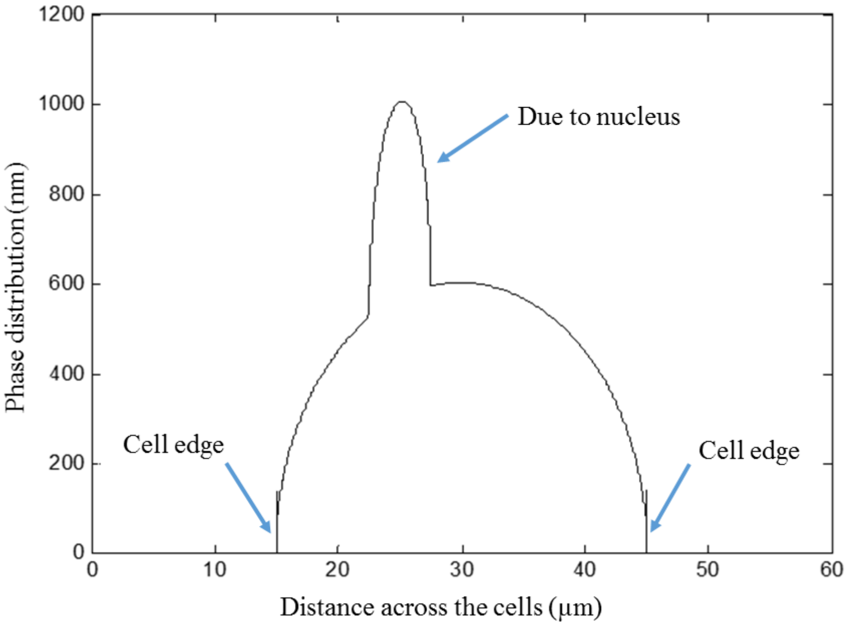

Figure 3.2 Phase distribution across the cell membrane, cytoplasm and the nucleus

Finally, the model considering all the structural components across the cell produces the phase distribution as shown in Figure 3.3, where, the distribution of mitochondria chosen was random. A very high phase and steep gradient change can be seen around the edges of cells (Figure 3.1 and Figure 3.2). The phase change at the edge of a cell is approximate 347 nm and appears as a gradient of $5.8x10^5$ nm/μm limited by the sample spacing in the simulations (approximately 0.6 nm). This abrupt change in phase and the fact that the phase change is a large fraction of one fringe signifies that the location of the edge of the cell should be able to be determined accurately. Consequently, cell-to-cell interactions are expected to be quantifiable. The presence of the nucleus and mitochondria significantly increases the phase change across a cell (Figure 3.3).

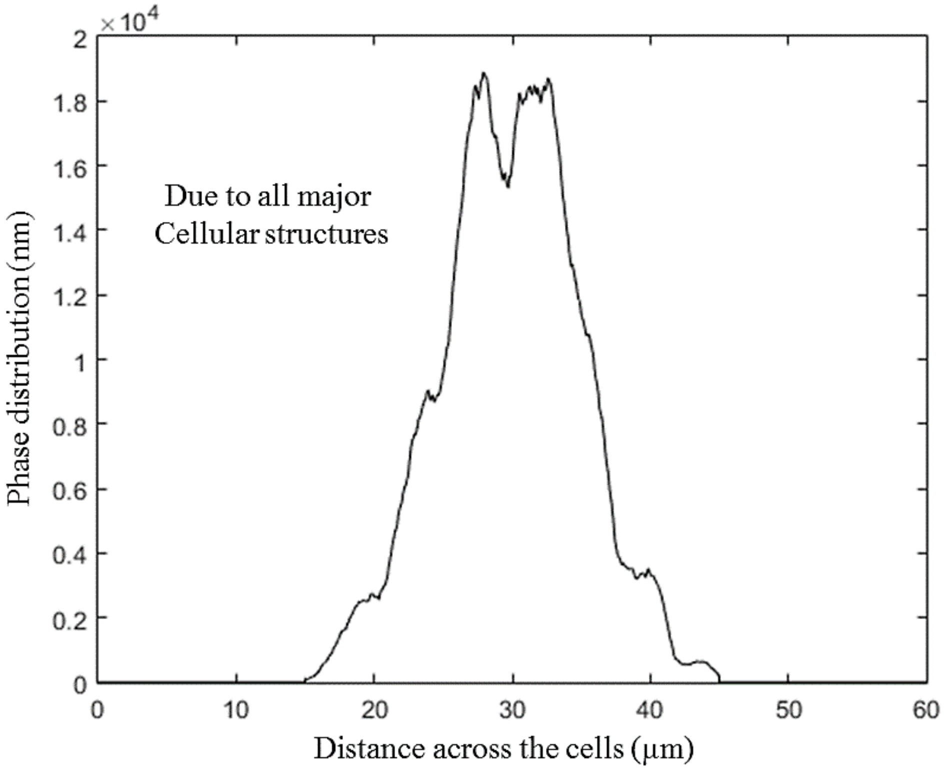

Figure 3.3 Phase distribution across the cell contains all the organelles

The reason for the significant phase change is that a single cell may hold a vast number of mitochondria (i.e. 200 - 1000 in numbers) and hence, the phase change due to mitochondria becomes dominant in the system. This is relevant to phase information of cells being used as a cancer diagnostic method. In the presence of representative levels of mitochondria, the most substantial phase change across a cell goes from approximately two fringes to 40 fringes. The amplitude change in transmission can be increased by using stains or dyes and stains can lead an increased phase change. However, the phase change from organelles tends to be much larger than the noise from PSAs. Hence, it is not required to look at resonant interference effects. Therefore, there is a need to establish the typical phase profile of a cell and the application of quantitative phase microscopy to measure the phase of the cells in single cell layers and multi-layers cultures (as required to simulate the full range of cell differentiation and regeneration phenotypes in urothelium).

3.3 Assessment of phase shifting algorithms

Phase stepping is now recognised an efficient method that allows automated fringe processing [44], measurement of displacement inside a cavity, strain [121] and surface profiles [93]. The most significant source of error in high-precision optical interferometer based instruments can be an inaccurate calibration of phase shifters [48] and the phase noise generated by speckle patterns [93]. Inside a phase shifting microscope, a certain number of intensity samples can be obtained with an equal phase shift of $2\pi/n$, where, $n = 0, 1, 2, 3 \ldots etc.$ known as intensity sampling [110]. The basic idea is to obtain different images of a fringe pattern with a constant phase increment between the consecutive frames so that a given pixel of the digitising system samples a periodic intensity over one period [25]. The conversion of the sampled intensities into phase using the methods introduced in Section 2.5 can be susceptible to different types of errors. The first significant source of error can be the real phase shift is different from the expected value. This can also be referred to as miscalibration of the phase stepping mechanism [25]. The second source of error can be that the intensity profile obtained was not purely sinusoidal, i.e. some harmonics are present due to a nonlinear intensity response. Lastly, the presence of scattering, e.g. from dust or imperfections on the optics, can generate diffraction and /or speckle patterns that add phase noise to the measurement [93]. The purpose of this chapter is to consider the implication of different PSAs, illumination source wavelength and source bandwidth on the phase noise obtained in the reconstructed phase maps from phase-stepped interference images. Furthermore, such a systematic investigation has not been reported to date and the results may have implications on the microscope design to produce a high contrast artefact-free image from a biological sample.

3.3.1 Description of phase assessment models

The theoretical mathematical models were written in MATLAB based on two-beam interference for the assessment of the phase measuring resolution in the presence of narrowband and broadband illuminating light with varying bandwidths. Let one consider; a biological sample is illuminated with a partially coherent light; the light field is decomposed in the microscope into the scattered, $E_s(x,y) = A_s e^{i\Delta\varphi_s(x,y)}$ and non-scattered, $E_{ns} = A_{ns}e^{i\Delta\varphi_{ns}}$ image light fields after passing through the sample. The two beams can be superimposed to form an interference intensity image at the detector. The phase distribution from the image object field $\varphi_s(x,y)$ and the background φ_{ns} can be expressed as the phase function at position (x,y). The total electric field received at each pixel on the CCD camera can be written as per Eq. (3.2).

$$E(x,y) = E_{ns} + E_s(x,y) \tag{3.2}$$

Further, the intensity of an interference image $[I(x,y)]$ at the detector can be obtained using Eq. (3.3) - Eq. (3.6). In Eq. (3.3) and Eq. (3.4) $*$ represnts the complex conjugate.

$$I(x,y) = \left[E_{ns} + E_s(x,y)\right] \times \left[E_{ns} + E_s(x,y)\right]^* \tag{3.3}$$

$$I(x,y) = E_{ns}E_{ns}{}^* + E_s(x,y)E_s(x,y)^* + E_{ns}E_s(x,y)^* + E_{ns}{}^*E_s(x,y) \tag{3.4}$$

$$I(x,y) = A_{ns}^2 + A_s(x,y)^2 + A_{ns}A_s(x,y)\left(e^{i(\varphi_s(x,y)+\varphi_{ns})} + e^{-i(\varphi_{ns}+\varphi_s(x,y))}\right) \tag{3.5}$$

$$I(x,y) = I_{ns} + I_s(x,y) + 2\sqrt{I_{ns}I_s(x,y)}\cos\left(\Delta\varphi(x,y)\right) \tag{3.6}$$

where $I_s(x,y)$ and I_{ns} are the intensity of scattered and non-scattered image fields respectively, $\varphi_s(x,y)$ is the phase delayed by objects in the sample and φ_{ns} is the phase from the non-scattered field (i.e. background). Furthermore, Eq. (3.6) can be generalised for an illumination broadband source, for example a white-light LED or a halogen lamp or a specific colour LED, where the full range of wavelengths can be utilised. The source has an intensity profile given by $I(\lambda)$ as per Eq. (3.7) that can be written as given below.

$$I(x,y,\lambda_k) = \sum_{k=\lambda_1}^{\lambda_k} I_{dc}(x,\ y,\ \lambda_k) + \sum_{k=\lambda_1}^{\lambda_k} I_{ac}(x,\ y,\ \lambda_k)\cos\left(\frac{2\pi}{\lambda_k}x + \varphi_n\right) \tag{3.7}$$

where I_{dc} is the average intensity relating to the background and I_{ns} is the modulation intensity relating to interference fringes, n is the number of phase shifts, λ is the wavelength, and x is an OPD and φ_n is the phase shift parameter for each phase-shifted interference image. Eq. (3.7) reduces to Eq. (3.8) in the case of narrowband illumination:

$$I(x,y,\lambda) = I_{dc}(\lambda) + I_{ac}(x,y,\lambda)\cos\left(\frac{2\pi}{\lambda}x + \varphi_n\right) \tag{3.8}$$

In either case, the interference phase, $\varphi = 2\pi x/\lambda$, can be obtained from a sum of sine and cosine components as per the given Eq. (3.9).

$$\varphi(x, y, \lambda_k) = \tan^{-1}\left(\frac{\sum_{i=1}^{N} \sum_{k=\lambda_1}^{\lambda_k} I_{i,k}(x, y) \times \gamma_k(x, y) \sin\left(\frac{2\pi}{\lambda_k} OPD + \varphi_i \right)}{\sum_{i=1}^{N} \sum_{k=\lambda_1}^{\lambda_k} I_{i,k}(x, y) \times \gamma_k(x, y) \cos\left(\frac{2\pi}{\lambda_k} OPD + \varphi_i \right)} \right) \tag{3.9}$$

3.3.2 Principle of phase unwrapping

The phase distribution can be measured inside an interferometer by changing the OPL between two arms known as phase stepping. The extraction of the phase $\varphi(x, y)$ using an arctangent function as per Eq. (3.9) that only ranges values from -π to -π and hence, phase discontinuities are present. A multiple of 2π needs to be applied to the wrapped phase at each pixel point to obtain a contiguous phase distribution known as phase unwrapping. The discontinuities in phase map can be resolved as per Eq. (3.10).

$$\varphi_{map}(x, y) = \varphi(x, y) + 2\pi k(x, y) \tag{3.10}$$

where $\varphi_{mas}(x, y)$ is the unwrapped phase map and $\varphi(x, y)$ is the wrapped phase obtained from Eq. (3.9) and $k(x, y)$ is the fringe order number. Phase unwrapping is now a fast and straightforward process in the majority of cases and any genuine discontinuities in the object phase profile can be localised to their original position [92], [93]. For real-time measurements of complex phase maps containing genuine object discontinuities, additive noise, stray reflection and mechanical vibrations can produce pixel scale or larger disturbances in the phase which may obstruct the phase unwrapping process [122]. Such type of complex discontinuities can still be mapped by using temporal phase unwrapping approaches where the phase is unwrapped along a temporal axis rather than spatially [123].

3.4 Error sources in phase measurement experiment

In this section, most common sources of error in PSI are described in brief. The error degrades precision and accuracy of the measured phase. The example of errors includes miscalibration of the phase shifter, aberration in the interferometric optics and reference wavefront, nonlinearity due to detector, air fluctuations and mechanical vibrations. These type of errors can be avoided by placing the interferometer optics on a vibration-isolated table, enclosing interferometric optics inside an opaque box to isolate from air currents and capturing data within few milliseconds (i.e. ≤ 5 - 10 ms).

3.4.1 Incorrect phase shift between interference frames

The inaccurate calibration of phase shifter, mechanical vibrations and air fluctuation in the laboratory leads to an incorrect phase shift between the sequential interference frames. The errors can be simply a linear term or non-linear. The accurate calibration of the optical system can eliminate the errors caused by miscalibration. The aberrations in the optics and / or a reference wave front error primarily cause a distortion on the measured phase. The effect can be reduced by using a high quality reference mirror and measuring the wave front (with no sample) that could be subtracted from the subsequent new measurements from the test objects. Severely aberrated wave fronts can give errors in the applied phase shifts; however, these tend to be insignificant compared to the other sources. Furthermore, an error in phase shift due to vibrations is much harder to avoid because "an optimum algorithm depends upon the frequency of vibration as well as the vibration relative to the phase shifting mechanism" [f].

3.4.2 Error due to detector nonlinearity

The error in the phase measurement can be introduced due to a nonlinear linear response to irradiance by the detector. Generally, the CCDs type detector array read out the even and odd rows through different registers for a good linear response. However, if the gain between the two registers is different and nonlinear it may cause an error in the measured phase values.

3.4.3 Error due to shot noise

The idea of multiplicative intensity noise is introduced in [93]. The phase-shifted frames can be affected by additive electronic noise that leads random phase errors statistically equivalent as in the case of speckle decorrelation. These phase errors are only 0.1 - 1.0 percentage range and are insensitive to ratio of the scattered and non-scattered beam intensity. The multiphoton noise from a photodetector can be modelled mathematically as per Eq. (3.11).

---

[f] Wyant, J. C. Phase shifting interferometry.nb - the University of Arizon, April 2011. URL http://fp.optics.arizona.edu/jcwyant/Optics513/ChapterNotes/Chapter05/Notes/Phase%20Shifting%20Interferometry.nb.pdf. Accessed on: 03/01/2015

$$I_o(x,y) = I(x,y) \times (1 + rand) \tag{3.11}$$

In the Eq. (3.11), $I(x,y)$ is the intensity of image, $I_0(x,y)$ is the intensity of image at the CCD camera and $rand$ is a function that generates an array of uniformly distributed random numbers in the interval (0,1). If a light source is emitting photons, the detector receives photons over an average time period at the pixel of a camera. The statistical property of shot noise can be found in the Goodman's work [124]. The shot noise suggests that there would be a random statistic on the received photons to get an intensity, which exhibits a standard deviation of plus or minus the square root of a number of the photons at that pixel.

$$\zeta_\varphi = \sqrt{p} \tag{3.12}$$

where ζ_φ is the shot noise, and p is the number of photons received at the detector. For example if the camera receives 100 photons a shot noise of 10 can be experienced or if the camera receives 10000 photons the shot noise will be 100. It implies that the absolute level of noise increases with intensity. The percentage of shot noise from the photodetector can be measured as per Eq. (3.13).

$$\%\_noise = \frac{Std(I_n)}{mean(I_n)} \times 100 \tag{3.13}$$

where I_n is the intensity at a pixel at the photodetector and n is the image number. A shot noise of 1.228 % was measured experimentally by examining a scene with a uniform illumination over 100 images using Eq. (3.13) for the Basler (Model: scA1400-17 gm) camera used in this project. The measured shot noise will be used in computational models such that the results will representative of those that can be expected in practise. The shot noise also causes an uncertainty in the measured phase as it can affect the phase-stepped images in different ways. The errors can be reduced by either employing a frame averaging approach or by capturing a higher number of phase-shifted intensity interference images.

3.4.4 Error due to intensity fluctuation

Similar uncertainties in the measured phase can also be introduced by the intensity fluctuations from an illumination source. The error can be quantified by finding the standard deviation in the measured phase as per [125] using Eq. (3.14).

$$\sigma_{\varphi} = \frac{1}{\sqrt{n} \times s} \tag{3.14}$$

where n is the number of phase-shifted intensity images and s is the signal to noise ratio. In the ideal condition, the standard deviation in phase noise σ_{φ} is limited by the number of photons (p) incident at the detector as per [126] using Eq. (3.15).

$$\sigma_{\varphi} \propto \frac{1}{\sqrt{p}} \tag{3.15}$$

3.4.5 Error due to quantisation

The difference between the input signal values to digital output signal value (rounded to the nearest integer) from a detector is referred as the quantisation error. In most applications, 8-bits (256 levels) is used in the digitisation of signals but higher levels, for example 10-bits or 12-bits or even 16-bits can be used to minimise the effect of quantisation. For example, "if the fringe modulation does not span the full dynamic range of quantisation levels the effective number of bits is less than the quantisation level" [f]. The standard deviation in phase error due to quantisation can be approximated as per [125] using Eq. (3.16).

$$\sigma_{\varphi}(PSA,\ b) = \frac{2}{\left(\sqrt{3 \times PSA}\right) 2^{i}} \tag{3.16}$$

where PSA is the phase shifting algorithm and i is the bit integer. The quantisation error can be minimised by averaging the captured data sets if the noise is higher than one bit.

3.4.6 Error due to additive white noise

When a CCD sensor captures an intensity image, the disordered motion of electrons causes a noise error known as additive white noise. The additive white noise can be a combination of the dark noise, transfer noise – addition or loss of charge carriers during image transfer process in the CCD sensor and the readout noise – caused by signal amplifying process. In general, this type of noise is modelled as additive Gaussian noise. Since the noise is signal independent, hence, the recorded image can be given as per Eq. (3.17).

$$I_r(x, y) = I_t(x, y) + \zeta(x, y) \tag{3.17}$$

where $I_t(x, y)$ is the true intensity image, $I_r(x, y)$ is the recorded intensity image with noise $\zeta(x, y)$ described by its variance and mean. The signal to noise ratio (SNR) can be measured as the ratio of the variance of true images σ_t to the variance of noise σ_ζ in the image (i.e. σ_t / σ_ζ).

3.5 Uncertainties in phase measurement

When imaging a biological object in the sample under a microscope, an approximately uniform illumination field is produced using a high numerical aperture condenser lens. The illuminating light field affects the phase measurement capability because the phase resolution depends on the interference of the scattered and non-scattered image fields from the objects surrounded by the medium and how the light emerge out after interacting with the objects in sample. Computational models for the expected uncertainties in the phase terms calculated from the PSAs have been used to explore the effect of microscope design (source characteristics of centre wavelength and bandwidth) as a function of OPD from the sample. The simulations have been conducted in MATLAB and follow a similar process to those reported in [45]. The interference function from Eq. (3.7) was modelled for each OPD a summation of the intensities obtained across the source spectrum and taking into account of the relative intensity at each wavelength. This process was repeated for each phase step. The resulting interference intensities as a function of OPD are then normalised to the same DC and modulation level as found in the experimental results (Chapter 5) such that values can be compared directly. The intensities were quantised and multiplicative noise with a standard deviation of 1.228 % applied as shot noise and was expected to be the dominant noise mechanism in the system [93]. The MATLAB code for the simulation is included in the thesis as appendix A.1. Representative results are included in the following figures and tables. If the object is illuminated using a narrow bandwidth source, for example a green LED (FWHM $\approx$ 42 nm, source spectrum defined for M530L3 LED from Throlabs) (Figure 3.4) the repeatability in the phase measurement (to 1 standard deviation) are in nanometer scale (1.732 nm, Figure 3.5).

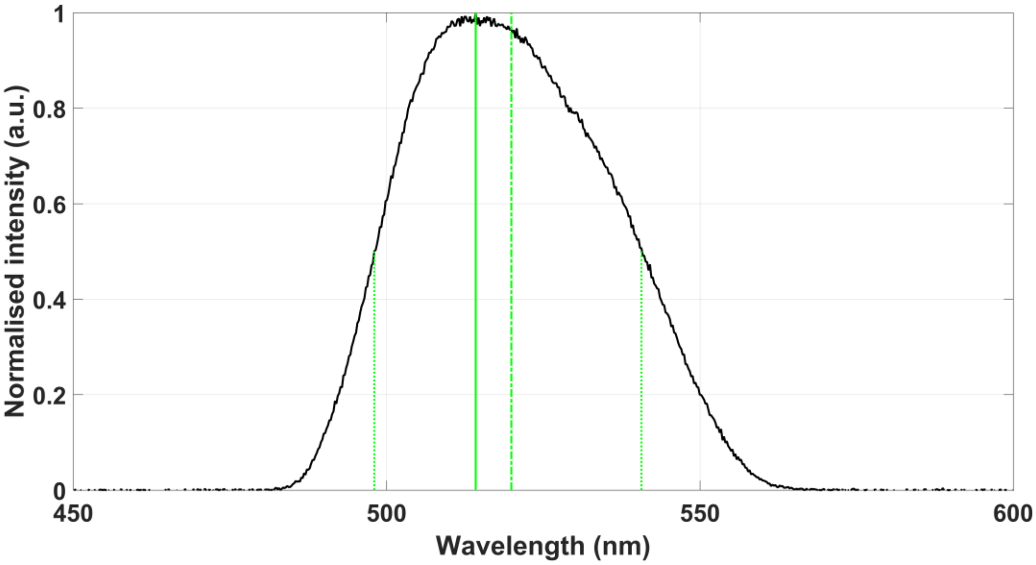

Figure 3.4 Spectrum profile of green LED, centroid wavelength (519.9 nm), peak wavelength (514.20 nm), FWHM - 42.60 nm

In the given Figure 3.5, top part shows the interference intensity as a function of OPD and reveals almost uniform fringe visibility over the OPD range shown (1250 nm), a consequence of relatively narrow bandwidth of the source. The effect of multiplicative noise is evident from an increased noise amplitude at the peaks (i.e. crest) of the intensity function compared to the troughs. Hence, the calculated (unwrapped) and theoretical phase distributions are practically identical which can be seen in the middle graph (in this case the six plus one frames at 60° steps algorithm has been used). The lower plot shows the difference between the calculated and theoretical unwrapped phase distributions and for this case exhibits generally random noise with a standard deviation of 1.732 nm corresponding to 1/300th of a fringe at the source centre wavelength of 520 nm. This type of simulation is useful to assess the noise contributions from a particular PSA, as the interferometric intensities are representative of real measurements but otherwise ideal. The possible reason for obtaining proper phase data is the high modulation with a narrow bandwidth illumination source. Furthermore, the modulation between the interfering scattered and non-scattered image light fields in the simulation experiment are of good quality (Figure 3.6). In this case, the interference intensity is plotted at 0° and 90° phase steps before the application of multiplicative noise.

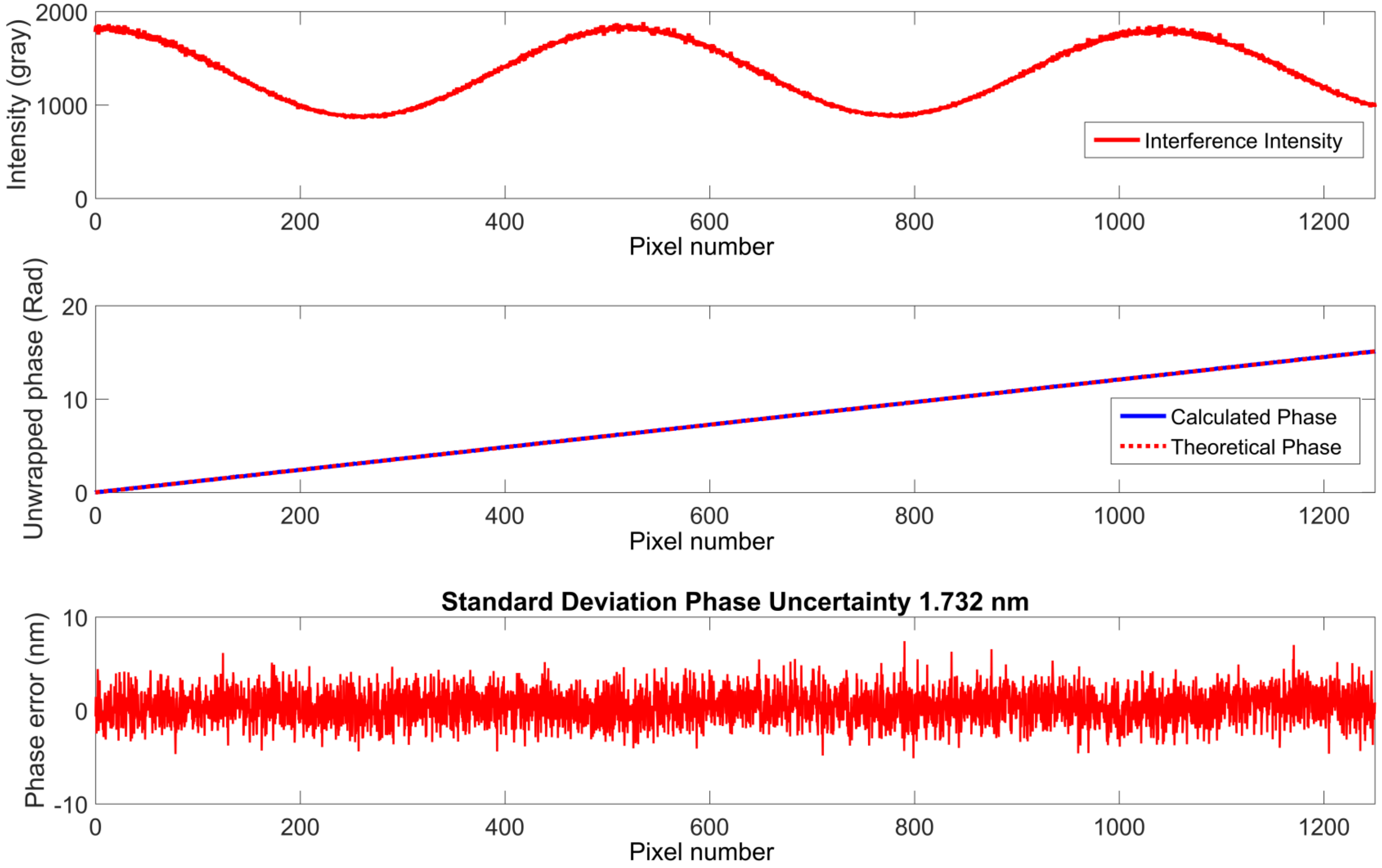

Standard Deviation Phase Uncertainty 1.732 nm

Figure 3.5 Uncertainty in the phase measurement under green LED illumination using 6+1F@60° PSA. The phase error was considered in nm due to the fact of measuring large optical path difference from thick optical and biological samples.

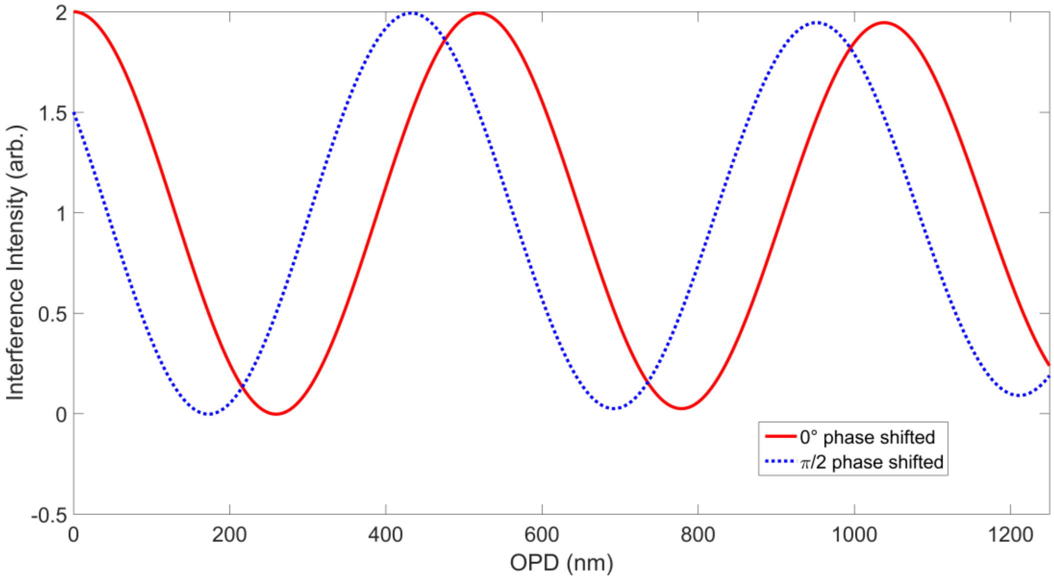

Figure 3.6 Simulated interference of a narrowband green light illumination from an LED.

The modulation depth of the interference signal is reduced if the narrowband source is replaced by a broadband source (FWHM, 30 - 90 nm), for example the illumination from a green LED emits the waves with wavelength λ and a spectral width $\Delta\lambda$ and this spectrum of waves that interfere constructively at some point in space will no longer be constructive after some additional optical path length known as the coherence length (*CL*). The coherence length for a Gaussian source intensity spectrum can be quantified as per Eq. (3.18).

$$CL \approx \lambda^2 / 2\pi\left(\Delta\lambda\right) \tag{3.18}$$

Interestingly, the modulation depth decreases when measuring more substantial optical path differences $\geq$ 1250 nm with an increased bandwidth (FWHM ≥ 100 nm) of illumination source and very short coherence length (≤ 8 nm) (Figure 3.7). This leads to a systematic increase in uncertainty between the calculated and theoretical phases as the OPD increases. Over the OPD range of 1250 nm the uncertainty is now increased to approximately 18.8 nm and is greater than 50 nm (1/10th of a fringe) at the maximum OPD considered. The low modulation of fringes after 650 nm OPD leads to an underestimation of the phase distribution with large standard deviation in phase uncertainty (Figure 3.7). This effect can be seen in the unwrapped phase in the middle part of Figure 3.7, where the theoretical phase (red dotted line) is up than the calculated phase (blue line). The six plus one frames at 60° PSA was used in this case. It implies that low modulation depth can be the primary source of uncertainty in the measured phase with a broadband illumination. A simulated interference of light waves from a broadband white-light source is presented in Figure 3.8. In Figure 3.8, the drop in modulation depth after 650 nm OPD can be seen clearly and it becomes worse after 1800 nm OPD. Further, the uncertainties caused by an illumination source due to varying bandwidth and wavelength can be reduced if a more appropriate PSA is applied.

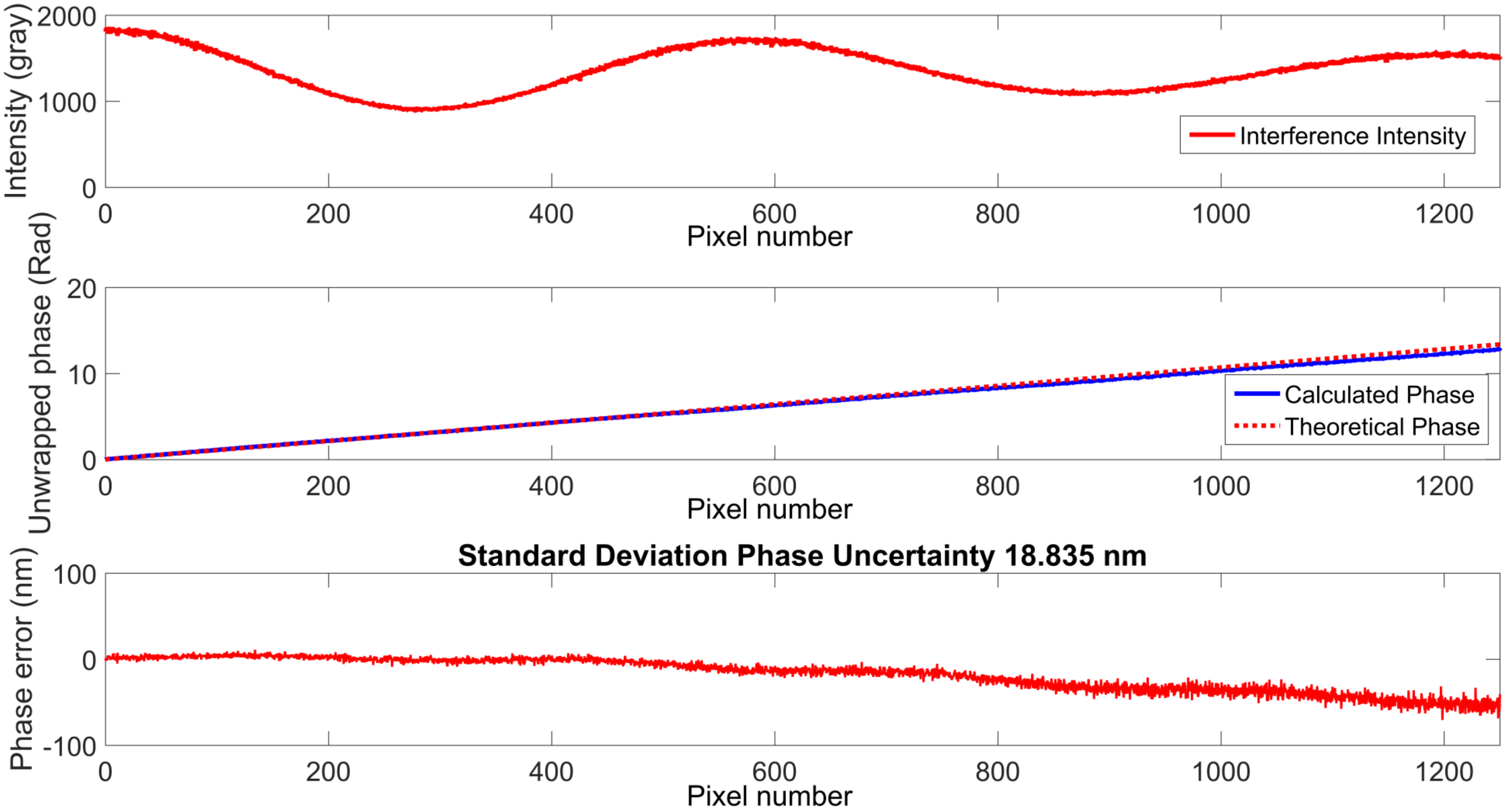

Figure 3.7 Uncertainty caused in phase measurement by warm white-light LED illumination using 6+1F@60° PSA. The phase error was considered in nm due to the fact of measuring large optical path difference from thick optical and biological samples.

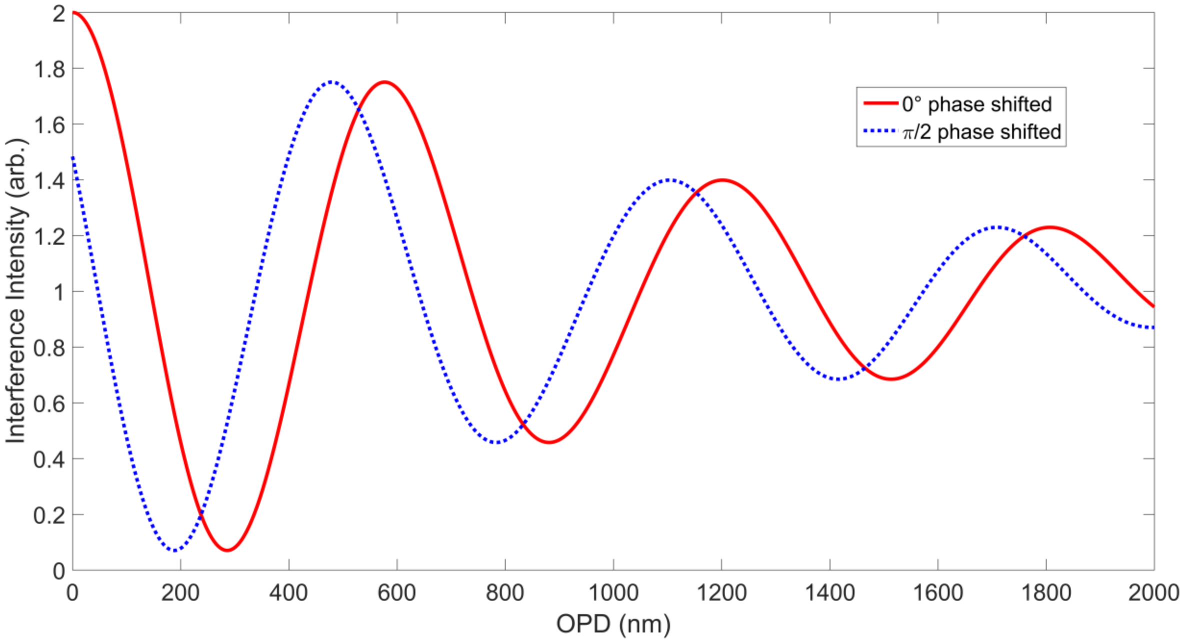

Figure 3.8 Simulated interference of a warm white-light illumination from an LED.

The theoretical simulations are implemented in MATLAB to understand the uncertainties caused by varying bandwidth (1 - 250 nm) and the centre wavelength (450 - 650 nm) of the broadband illumination sources and the role that the PSA has on the calculated phases. In the simulations, it is particularly interesting to find solutions that give low phase uncertainties over more extended optical path difference distributions that relate to thicker biological samples containing multiple cell layers. The reason to get particularly interested and concerned at the same time is to understand the benefit (or otherwise) of large broadband (FWHM, 200 - 300 nm) sources in quantitative phase microscopy, such as, those found in the work of Popescu et al. [16]. In the simulation as expected, the better phase resolution and distribution were obtained with narrow bandwidth illumination (FWHM - 1 nm or 42 nm) compared to broadband illumination (FWHM - 250 nm) sources from almost all the PSA methods considered here (Table 3.1 to Table 3.3) and reviewed in Section 2.5.

The tables (Table 3.1 to Table 3.3) show that the choice of PSA can make a big difference in the uncertainty in the obtwined phase noise measurements. In general, the use of more sophisticated (i.e. greater number of frames) PSAs give lower phase uncertainties. For small OPD ranges ($\leq$ 250 nm), the minimum phase uncertainties are obtained with a bandwidth of 42 nm, with a small increase for bandwidth of 1 nm and a larger increase for bandwidths of 250 nm. The simulations do not take an account for coherent noise that can be added with very narrow bandwidth sources, for example laser. For longer range measurements OPDs $\geq$1250 nm, the uncertainties increase significantly for the case of broadband light source, bandwidth 250 nm. This implies that the configurations reported by Popescu et al. [40], [127] will not work well for multiple cell layers or thicker biological samples. Hence, the narrowband LED sources, giving typically 30 - 50 nm FWHM are to be implemented in the LQPIM system (Chapter 5) for the assessment of phase resolution from both the optical sample (i.e. glass beads) and the transparent biological sample (i.e. epidermis cells of *Allium cepa*). For such fixed cells the combination of a narrowband green LED with a higher number of frames phase shifting algorithm, for example 6+1F@60° can be utilised to produces better phase distributions.

Table 3.1 Theoretical performance of PSAs (centre wavelength - 520 nm, bandwidth - 1 nm)

PSA	**OPD - 250 nm**		**OPD - 1250 nm**		**Std Dev Phase noise over 1250 nm OPD (σ_{φ}, nm)**
	Mean OPD Error (nm)	Maximum OPD Error (nm)	Mean OPD Error (nm)	Maximum OPD Error (nm)	
3F@120°	1.877	8.638	1.935	11.327	2.385
3F@90°	1.960	8.637	2.196	13.710	2.849
4F@90°	1.648	6.350	1.629	7.463	2.041
5F@90°	1.946	8.432	1.852	8.915	2.322
7F@90°	1.471	6.368	1.439	6.916	1.842
6+1F@60°	1.294	5.202	1.296	5.527	1.628

Table 3.2 Theoretical performance of PSAs (centre wavelength - 520 nm, bandwidth - 42 nm)

PSA	**OPD - 250 nm**		**OPD - 1250 nm**		**Std Dev Phase noise over 1250 nm OPD (σ_{φ}, nm)**
	Mean OPD Error (nm)	Maximum OPD Error (nm)	Mean OPD Error (nm)	Maximum OPD Error (nm)	
3F@120°	1.920	7.957	2.028	11.767	2.486
3F@90°	1.976	13.005	2.413	13.615	2.974
4F@90°	1.690	6.621	1.754	8.855	2.231
5F@90°	1.798	8.444	2.057	10.384	2.425
7F@90°	1.439	5.918	1.560	7.112	1.965
6+1F@60°	1.330	4.819	1.403	6.205	1.703

Table 3.3 Theoretical performance of PSAs (centre wavelength - 520 nm, bandwidth - 250 nm)

PSA	**OPD - 250 nm**		**OPD - 1250 nm**		**Std Dev Phase noise over 1250 nm OPD (σ_{φ}, nm)**
	Mean OPD Error (nm)	Maximum OPD Error (nm)	Mean OPD Error (nm)	Maximum OPD Error (nm)	
3F@120°	7.198	26.697	58.476	202.826	69.207
3F@90°	8.677	27.483	56.993	286.040	76.928
4F@90°	5.790	18.096	58.360	194.983	68.267
5F@90°	11.504	21.189	68.803	207.940	79.291
7F@90°	3.707	12.807	81.659	204.477	72.813
6+1F@60°	4.723	12.611	65.206	190.010	70.078

The capture of six plus one phase shifted interference frames takes a finite time and hence, it is also relevant to look at alternative PSAs that can produce similar quality phase measurements but with a smaller number of frames and hence, in a faster time. From the simulation experiment it can also be concluded, that 4F@90° and 6+1F@60° PSAs would provide better imaging solutions for thin and thick transparent biological samples, respectively. The theoretical phase noise floor is much better using 6+1F@60° PSA for the narrowband (FWHM, 1 - 42 nm), middle (FWHM, 1 - 150 nm), and broadband (FWHM, 1 - 250 nm) from a uniform illumination source at a centre wavelength of 520 nm (Figure 3.9 to Figure 3.11, page 48 - 50). From the given mesh plots, it can be inferred that moving from the bandwidth (FWHM) ≥ 70 nm can be problematic and after 100 nm fails to find correct solution for the phase distribution, especially with larger OPDs. It can also be concluded that using an illumination source of higher bandwidth (FWHM ≥ 100 nm) cannot be a better choice to image thick transparent samples. At this point, almost all the phase shift algorithms were failed to find correct phase distribution from the objects in sample.

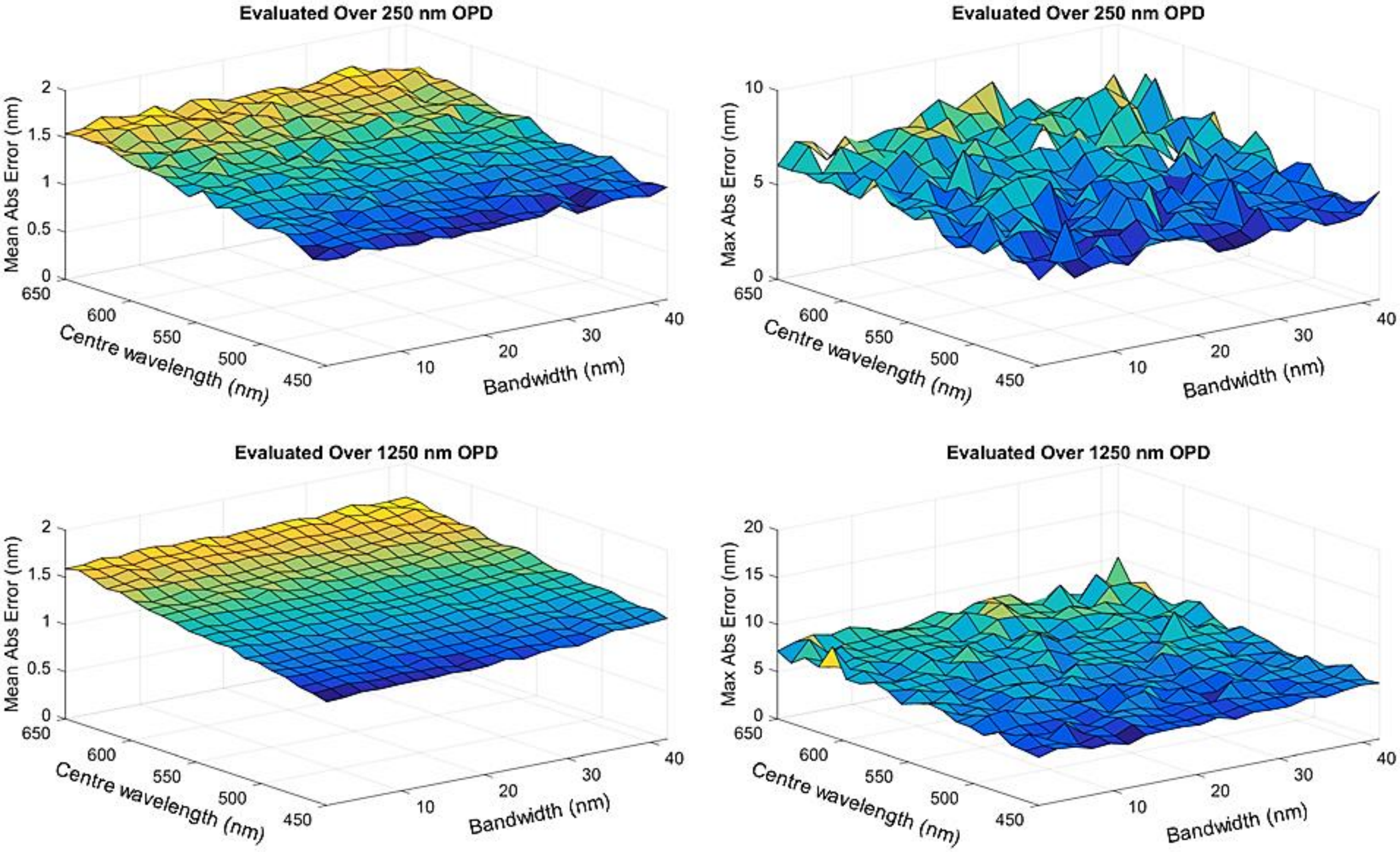

Figure 3.9 Theoretical phase noise using 6+1F@60° PSA, bandwidth (FWHM, 1 - 42 nm), centre wavelength (450 - 650 nm).

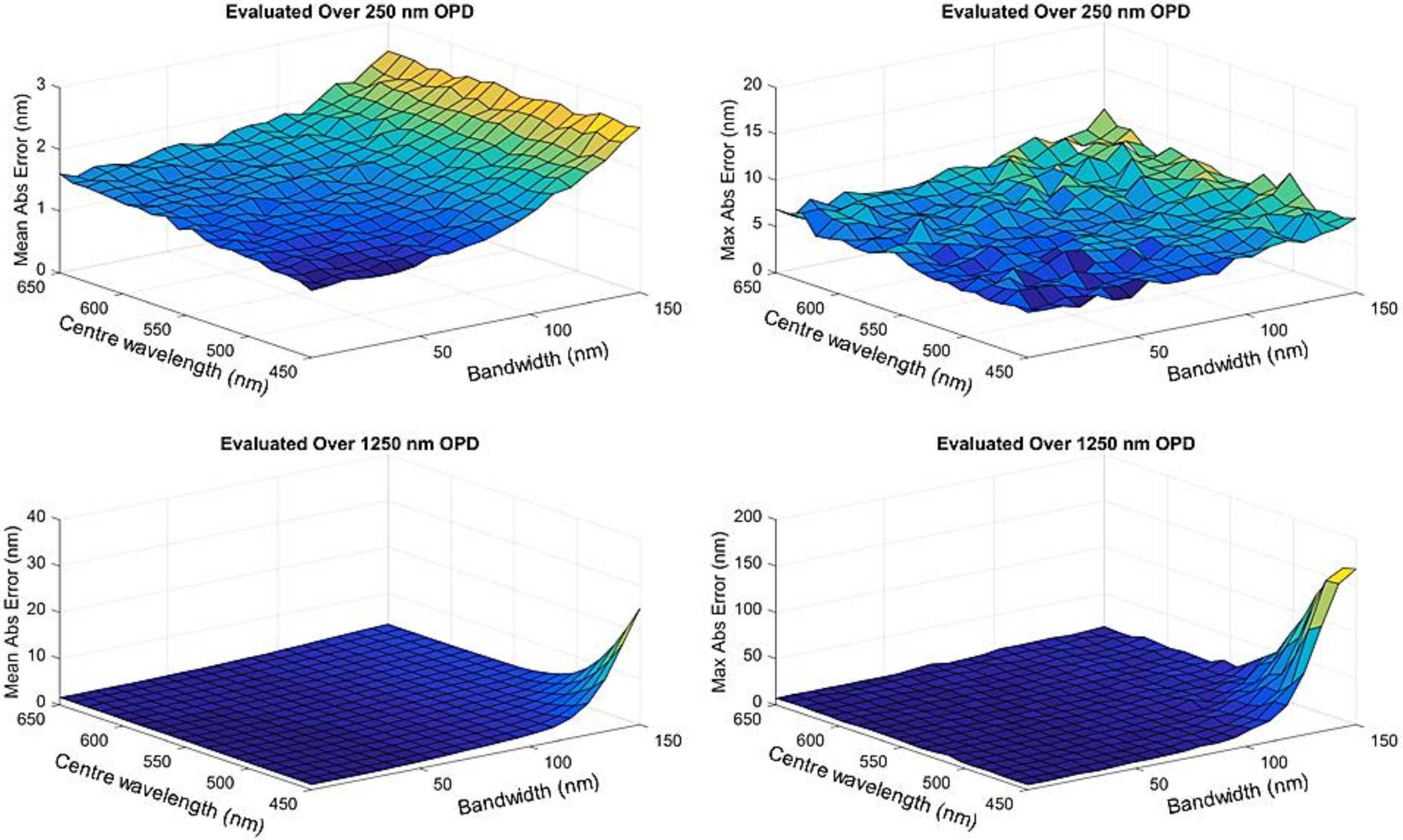

Figure 3.10 Theoretical phase noise using 6+1F@60° PSA, bandwidth (1 - 150 nm), centre wavelength (450 - 650 nm).

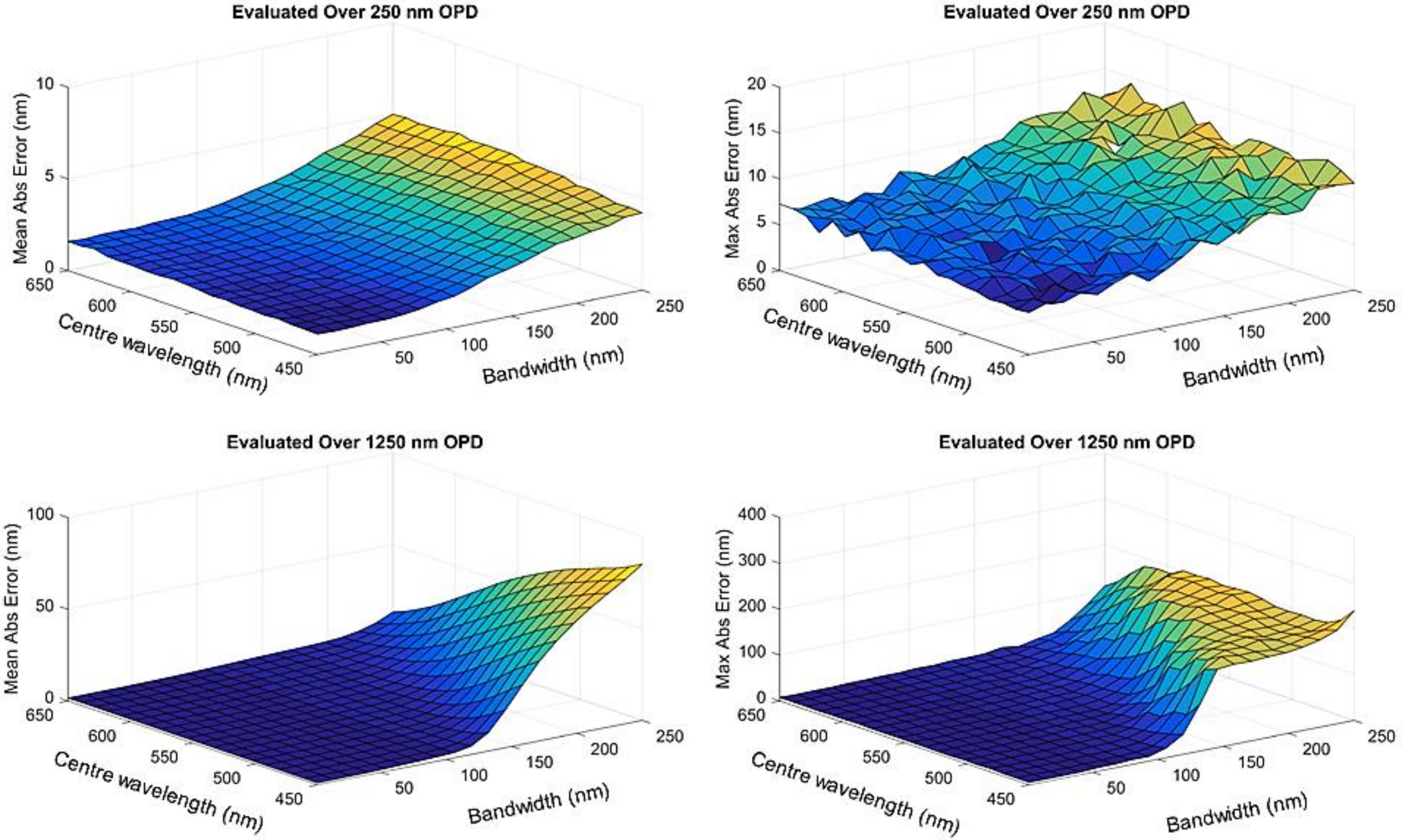

Figure 3.11 Theoretical phase noise using 6+1F@60° PSA, bandwidth (1 - 250 nm), centre wavelength (450 - 650 nm).

3.6 Summary

The chapter discusses the phase distortion in the illuminating wave front by typical objects in the sample, i.e. cells and cellular structures. The distortion in the wave front depends on the refractive index, thickness variation, structural organisation and composition of the specimen as discussed in Section 3.1. In general, scattering processes have not been considered explicitly in quantitative PCM. The effect of scattering will be dependent on the sample concerned as to whether scattered light contributes negatively to the halo effect or has a positive contribution in increasing the amplitude of what is considered here to be the ‘scattered wave’ but in practise comes about because of refraction at the boundaries between components in the sample. The general theoretical model for phase distribution from the cell and cell organelles was presneted in Section 3.2. The model considers an optical path difference range of either 250 nm (typical of a single cell holding only cytoplasm) or 1250 nm (typical of a single cell holding a nucleus and a few mitochondria). However, a realistic modelling was also performed in MATLAB (Section 3.3) to understand an optimum imaging solution for both thin and thick transparent biological samples. Section 3.3 gives brief information about the statistical parameters used in the simulations to make it realistic. The model has the flexibility to vary bandwidth and centre wavelength to examine the significant distributions using various PSAs. It is concluded that the phase reconstruction errors depend on the phase shift algorithm, bandwidth, and wavelength of the illumination source and that for measurements of both thin and thick biological samples the source bandwidth (FWHM) should be restricted to < 50 nm to obtain satisfactory measurements. The choice of phase shift algorithm depends on the phase resolution required. 6+1F@60° step algorithm offers best performance among those reviewed PSAs. However, 4F@ 90° step algorithm offers slightly increased noise performance (following Eq. (3.14)) but similar capabilities in measuring larger OPDs to 1250 nm as the contrast reduction obtained is more a function of the source bandwidth than the PSA used.

Chapter 4. OPTICAL DESIGN: LOW-COST QUANTITATIVE PHASE IMAGING MICROSCOPE

The prototype optical bench systems were constructed to show their practicality and application in understanding biological events. Two LQPIM optical system have been configured using standard optical components for imaging transparent phase objects from the biological origin. The fundamental philosophy is to utilise a low cost PZT phase shifting mechanism rather than the more prevalent SLMs, together with common path or otherwise approaches to separate the scattered and non-scattered light fields. Two LQPIM bench-top geometries, first with twin-machined concentric mirrors and second with LCAs are developed and discussed in this chapter for label-free cell imaging from the optical and biological samples (Section 4.5.2 and Section 4.5.3). An overview of the necessary optical components needed to configure bench-top optical systems and thereby achieving a working LQPIM system are given in Table 4.1. A stable configuration can be achieved by placing all the required components at precise positions relative to each other along the principal optical axis. The ability to control the component positions and their geometry determines the image field and Fourier field and hence, ultimately sets the performance of the imaging system.

Table 4.1 Optical components used in the design of the bench-top optics of LQPIM system

Catalogue Number	Specification of the optical component	Manufacturer
PLCN10XPH	10x C Plan Achromat Objective, Working distance - 10.5mm, NA - 0.25, FN - 22, Suitable for any coverslip thickness, and for phase contrast (PH1)	Olympus Ltd
RMS10X	10x Plan Achromat Objective, NA - 0.25, Working Distance - 10.6mm, Suitable for any coverslip thickness.	Olympus Ltd
CX-SLC	Slide Condenser lens, NA-1.25, FN - 20	Olympus Ltd
CX-PH1	Annulus Ring compatible with 10x and 20x Phase Contrast Objectives	Olympus Ltd
M530L3	Green Mounted LED, 1000 mA, 350mW (Min) Centroid wavelength from the manufacturer supplied spectrum 520 nm	Thorlabs Ltd
AC508-180-A	F - 180.0 mm, 2" Achromatic Doublet, ARC: 400- 700 nm, N-SSK5/ LAFN7	Thorlabs Ltd
AC254-300-A	F - 300.0 mm, 1" Achromatic Doublet, ARC: 400-700 nm, N-BK7/ SF2	Thorlabs Ltd
AC508-750-A	F - 750.0 mm, 2" Achromatic Doublet, ARC: 400-700 nm, N-BK7/ SF2	Thorlabs Ltd
CCM1-BS013/M	30 mm Cage Cube-Mounted Non-Polarizing Beam Splitter, 400 - 700 nm, N-BK7 - Grade A	Thorlabs Ltd
ACL2520U-A	Aspheric Condenser Lens, 25 mm, f - 20.1 mm, NA - 0.60 ARC: 350-700 nm, N-BK7/ SF2	Thorlabs Ltd
PF10-03-G01-10	1" (25.4 mm) Protected Aluminium Mirrors, Fused Silica	Thorlabs Ltd
scA1400-17gm	Basler CCD Camera, Resolution (1392 X 1040 Pixel), Pixel Size (6.45 μm x 6.45 μm), Frame Rate (17 fps), Mono, Interface (GigE), Video Output Format (Mono 8, Mono 16, Mono 12 Packed, RGB 8 Packed), Pixel Bit Depth (12 bits), Exposure Control (Programmable via the camera API), Synchronization (External trigger and Software), Quantum Efficiency (typically 58% (at 545nm), Dark Noise (typically 7,8 e), Saturation Capacity (typically 19ke), Dynamic Range (typically 67,7dB), Signal to Noise Ratio (42,7dB), Power Consumption (typically 3.5W), Sensor Vendor (Sony ICX285), Shutter (global shutter), Max. Image Circle (2/3"), Sensor Type (CCD), Sensor Size (8.98mm x 6.71 mm)	Basler AG
AG-LS25	Motorized Axes, Travel Range (12mm), Minimum Incremental Motion (0.05 μm), Maximum Speed (0.5 mm/s), Vertical Load Capacity (3N), Axial Load Capacity (2N), Holding Force (4N), Angular stability: Pitch (200 μ rad), Yaw (μ 200 rad)	Newport Corporation

4.1 Role of broadband illumination in QPI imaging

In practice, most interferometry-based techniques use monochromatic light, for example a laser. The long coherence length of the laser illumination gives good contrast interference fringes with some unwanted spurious fringes from the dust particles on the optical components and the sample surface. The matching of path lengths between the light beams from the two arms of an interferometer can be challenging, especially as the source bandwidth increases and coherence length reduces. The false information in the phase data introduced by spurious fringes is hard to avoid and relates to imperfections, damage, and / or contamination from optical surfaces. The speckles generated by laser illumination also degrades the image quality. White-light interferometry (WLI) can provide a more uniform illuminating wavefront without spurious interference fringes due to the short coherence length, however, a more precise path length matching is needed in the interferometer. WLI can be a powerful measurement tool for imaging label-free biological samples, when combined with modern computers and advanced analysis software.

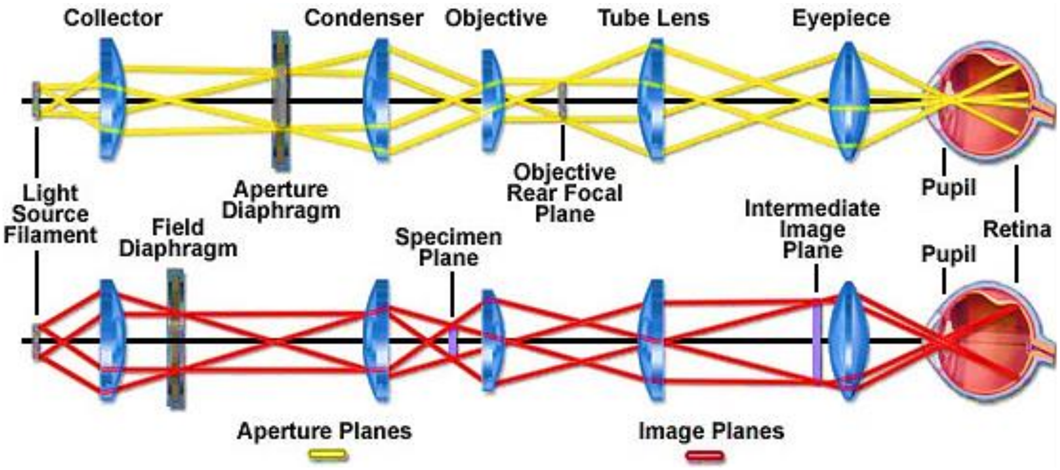

Figure 4.1 Aperture and image planes in Kohler illumination [g].

Kohler illumination is crucial optics to obtain a proper phase contrast image utilising a broadband or a laser source. In Kohler illumination, the image of a filament or a chip of an illuminating source is projected onto front focal plane of the condenser lens in the microscope

---

[g] http://zeisscampus.magnet.fsu.edu/articles/lightsources/lightsourcefundamentals.html, Assessed on 26/06/2015

with an aperture in place for spatial filtering of light (as sown in Figure 4.1) in order to give more uniform sample illumination. Furthermore, the front focal plane of the condenser lens is conjugated with the back focal plane of the objective lens in the microscope. This type of illumination provides a spatially uniform illuminating wavefront to illuminate objects in the specimen with diverse angles.

4.2 Spatial and temporal coherence of an illumination source

Spatial coherence can be defined as the correlation of intensities between two points at different locations across the full wavefront from the illumination source [100]. Temporal coherence is the correlation between the phase value of a light wave and itself delayed by a certain time interval. The temporal coherence of an illumination source depends on the chromatic composition of the illuminated light from the source. The spatial and temporal coherence between the scattered and non-scattered decomposed image fields from the sample can be maintained by precise placement of the optical components along the principal optical axis.

4.3 Magnification and resolution of the microscope

The magnification of the microscope (M_oM) can be defined as the size ratio between an object image and the original object and further, refers to the ability to visualise small objects by making them larger. For infinity corrected microscopes, as used here, the objective is used in combination with a tube lens to give the designated primary magnification whereas a secondary relay lens pair is used provide an additional magnification factor to achieve high magnification of the objects in sample. The magnification of a microscope can be measured using Eq. (4.1), where, f_1 is the focal length of the objective lens (i.e. 18 mm), f_2 is the focal length of the tube lens, f_3 is the focal length of the first relay lens and f_4 is the focal length of the second relay lens (refer Figure 4.2).

$$MoM = \left(\frac{f_4 \times f_2}{f_3 \times f_1} \right) \tag{4.1}$$

A magnification of 25x is achieved in the LQPIM system based on a standard 4f imaging system by utilising imaging and relay lenses in the optical configuration (Figure 4.2). A factor of 0.258 μm was calculated to measure object size in the image from Basler camera (Model: scA1400-17gm) having a pixel size of 6.45 μm using overall magnification of 25x.

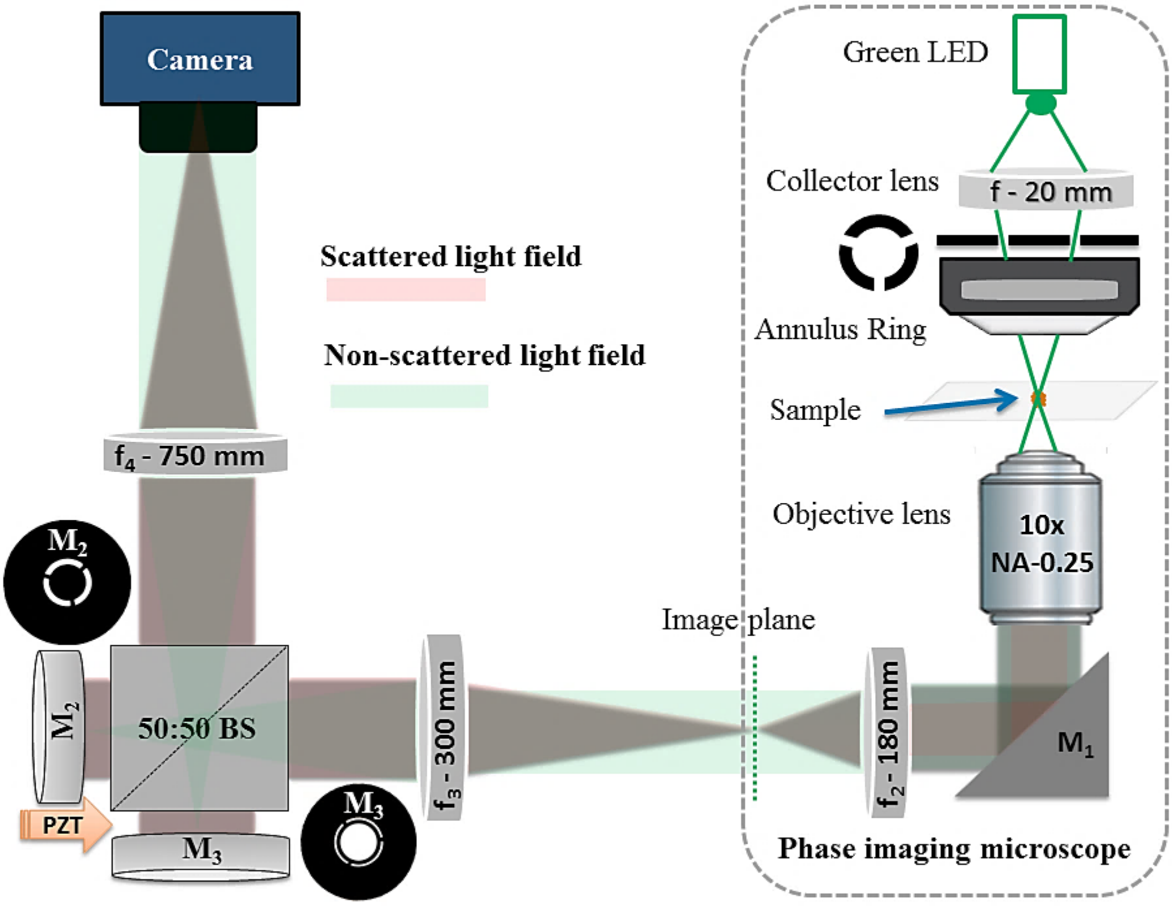

Figure 4.2 Schematic presentation of LQPIM system based on LCAs, f_2 - f_4 (imaging and relay lenses), M_2 - M_3 (mirrors with apertures in place) and BS (50/50 Beam splitter).

The resolution of the microscope (R) can be defined as the ability to distinguish or resolve two neighbouring objects precisely in space. The resolution of the microscope can be calculated as per Eq. (4.2) [h], where NA_{ol} and NA_{cl} are the numerical aperture of the objective and condenser lens, respectively, and λ is the wavelength of the illumination source.

$$R = \frac{1.22\lambda}{NA_{ol} + NA_{cl}} \tag{4.2}$$

Using Eq. (4.2), a spatial resolution of 0.431 µm was calculated for 0.25 NA 10x objective lens and 1.25 - NA condenser lens utilised in the PIM optics at an illuminating wavelength 530 nm. Further, the optical design preserves the resolving power of an optical system. The diameter of the observation field in the microscope can be defined as the field of view. The

---

[h] https://www.microscopyu.com/microscopy-basics/resolution. Accessed on: 02/08/2014

field number for utilised 10x objective lens in the optics is 22 and hence, a field of view (FOV) of 2.2 mm is calculated as per Eq. (4.3).

$$FOV = \frac{FN\_of\_objective\_lens}{Magnification\_of\_objective\_lens} \tag{4.3}$$

4.4 Calibration of phase stepper for phase shifting

In the context of microscopy, image of the objects formed at an image plane is the outcome of interference phenomenon [55]. Further, based on holographic imaging method an image can be classified as an interferogram [50]. An interferogram is the outcome of interference between the reference and the sample beam that holds valuable information, for example phase or wavefront distribution, morphological shape and size of objects in the sample. Three or more interferograms are needed for the analysis of phase distribution between the two interfering beams via PSI. Practically, the phase difference between two interfering beams can be quantified by recording intensity of the interference images while the phase difference between them can be changed in a consistent manner using a Michelson interferometer. The LQPIM bench-top optics configured in this research work utilises a phase shifting module (PSM) in the back focal plane for phase modulation between the scattered and non-scattered image light fields prior to the light fields being brought together at the CCD camera to form an interference image. The PSM was calibrated using a Michelson interferometer optics shown in Figure 4.3.

The optical system as shown in Figure 4.3, was configured to record the phase shifted interference intensity images at the focal plane of the output lens (OL, f = 150 mm). The reference mirror M_2 was linearly moved in controlled $\lambda/8$ steps to produce a phase shift of $\lambda/4$ or equivalently $\pi/2$ radian with the help of a PZT driven high precision linear stage (PT1/M - 25 mm Translation Stage with Standard Micrometer, Thorlabs). Four phase-shifted interferogram (Figure 4.4a) were recorded using a CCD camera and digitised by using a frame grabber with an in-house LabVIEW program [128]. The digitised frames were retrieved and processed in MATLAB [129] for measurement of the phase distributions at each and every pixel using Eq. (2.10). The mean phase shift angle (α) a measure of the accuracy of phase shifter was determined using Eq. (2.11) from the well-known Carré algorithm [48].

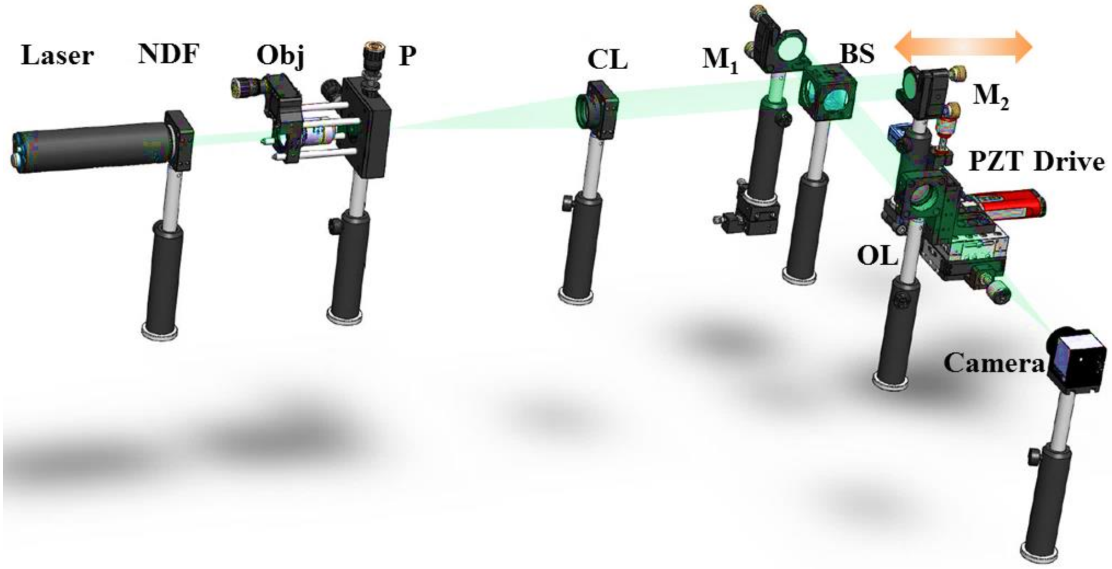

Figure 4.3 Schematic optics for the phase shifter calibration. NDF (Neutral density filter), Obj (Objective lens), P (Pinhole), CL (Collimating lens), BS (Beam splitter), M_1-M_2 (Mirror), OL (Output lens), PZT drive applied to mirror M_2.

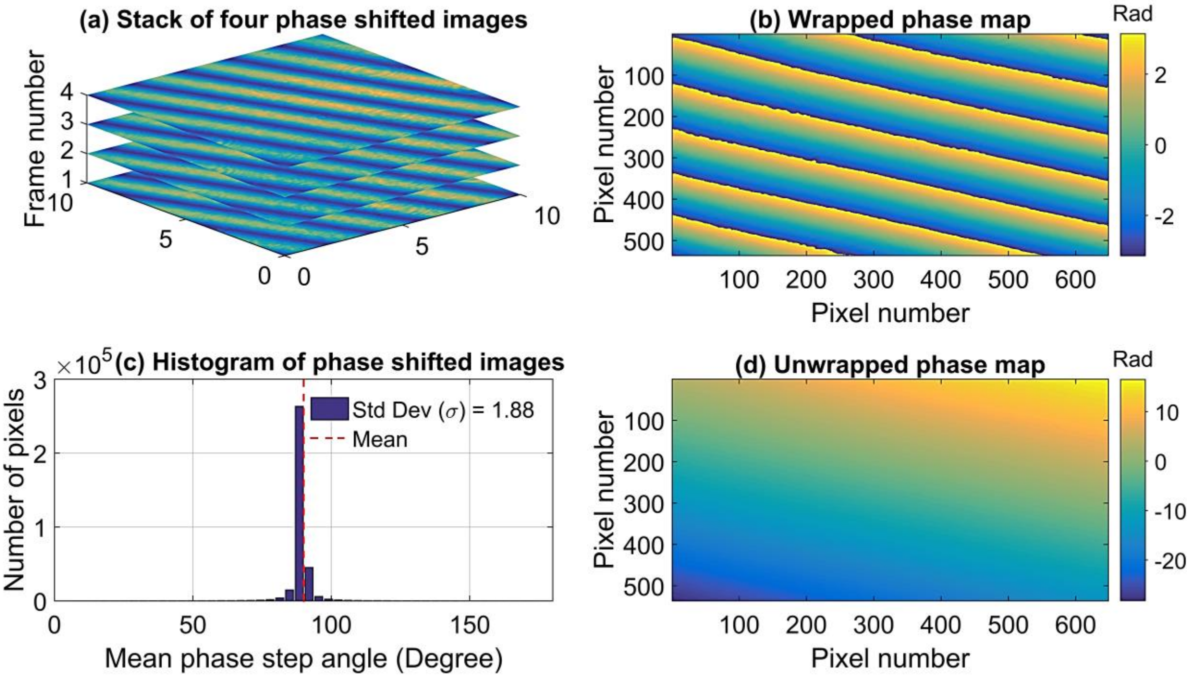

Figure 4.4 Processed phase-shifted images to check the accuracy of PSM.

The phase distribution thus calculated can be wrapped modulo 2π due to the nature of arctangent function (Figure 4.4b). Hence, a suitable phase unwrapping algorithm [45], [130] needs to be applied to get correct phase distribution (Figure 4.4d). The measured mean phase shift angle 90°±1.88 (mean ± Std Dev) confirms an accuracy of the phase stepper to introduce the predefined phase steps with appropriate accuracy between an interfering beams (Figure 4.4c). Mis-calibration, air turbulence and mechanical vibrations in the optical setup can affect the accuracy of the phase shifter. All these factors can contribute to an unknown phase shift and hence, introduces errors in the phase measurement experiment for the same optimised experimental conditions. The effect of these factors can be seen in Figure 4.5, where the standard deviation in the mean phase shift angle value is calculated much higher, i.e. 90°±5.24 with a wide histogram for the phase shift interference frames compared to one shown in Figure 4.4c. The effect of vibrations and air turbulence can be mitigated if all the phase-shifted frames are captured in a short time (i.e. typically $\leq$ 10 - 50 ms) and the interferometer module mounted on a separate sorbothane isolated platform can be isolated inside an opaque box.

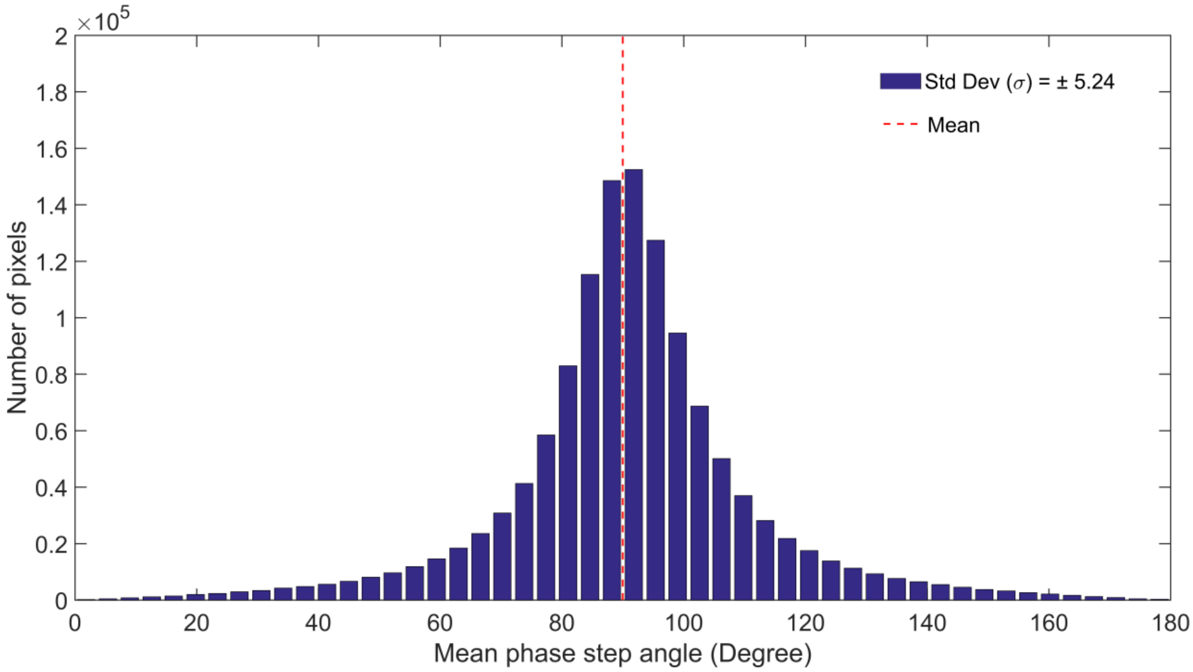

Figure 4.5 Histogram of phase-shifted interference images due to misalignment and mechanical vibrations.

4.5 Optical configurations of LQPIM system

A low contrast image of transparent label-free living cells can be seen while using an ordinary light microscope. A particular kind of optical light microscope is required to convert the intensity variations to phase, for example Zernike’s PCM [131]. The scattered image field passing through the phase plate built into the objective lens of the microscope at the specific numerical aperture is attenuated, out phased by $\pi/2$ radians compared to the transmitted beam from the rest of objective lens. Due to the visual artefacts and limitation of passive optical component, only a single $\pi/2$ phase modulation is possible and hence, only qualitative phase information can be retrieved. Furthermore, to study the fast-changing cellular dynamics of live cells in detail measurements with different phase shifts are required to capture entire scene of an event. Hence, to study the cellular dynamics of label-free cells LQPIM bench-top optics has been developed in this thesis. LQPIM system is based on Zernike's common-path phase contrast optics with an optical arrangement for phase shifting in the back focal plane of the microscope. It is a combination of two modules; first one is the phase imaging microscope (PIM) and second one is the phase shifting module (PSM) based on Michelson interferometer optics. The detailed information about PIM and PSMs optics can be found in Section 4.5.1, Section 4.5.2 and Section 4.5.3.

4.5.1 Phase imaging microscope

To meet the purpose of quantitative phase imaging a well-established Kohler illumination optics is used to illuminate the sample under LQPIM system. Kohler illumination is achieved by projecting the image of the LED chip (partially coherent) or a laser point source (coherent) onto the annular ring sitting in the condenser lens (CX-SLC, NA 1.25) using an aspheric condenser lens (ACL25416U, f - 16mm, NA - 0.79). The condenser annulus produces a narrow ring of illumination light field that is focussed through the sample. A standard plan achromatic phase contrast objective lens was selected to produce diffraction-limited infinity corrected images. The objective lens contains a phase plate at the same numerical aperture as the condenser annulus in order to apply a π/2 phase shift between the non-scattered (at the numerical aperture of the condenser annulus) and scattered waves (over the rest of the numerical aperture). The condenser lens suitably magnifies the illuminating light cone to over-fill NA 0.25 of the 10x objective lens. The condenser enables observations between 4x - 100x and in phase contrast mode when combined with a suitable annulus aperture. The condenser lens has two apertures, selected by an aperture slider and an iris lever helps the operation between dark field and bright field observation (Figure 4.6).

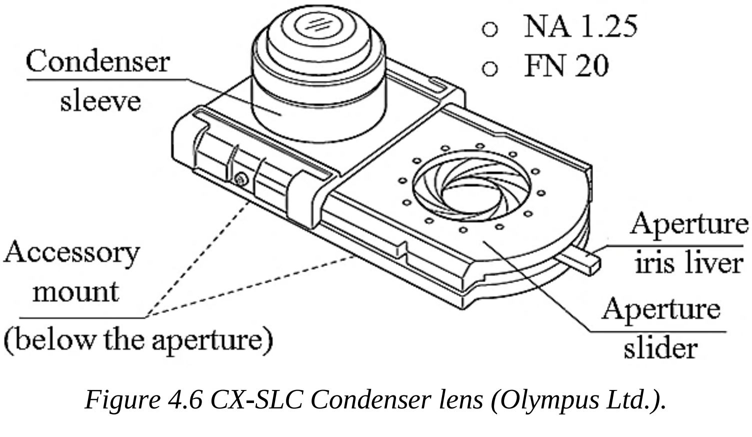

Figure 4.6 CX-SLC Condenser lens (Olympus Ltd.).

An achromatic doublet lens (AC508-180-A, f - 180 mm) was used as a tube lens to form the final image of objects in the sample at the image plane of the PIM optics. The bench-top optical geometry of the PIM provides 10x magnified image of the objects at the image (Figure 4.7). Furthermore, an added 2.5x magnification is also achieved from two relays lenses (f_3 - 300 mm and f_4 - 750 mm) utilised in phase shifting module to render an overall 25x magnified objects (Figure 4.13).

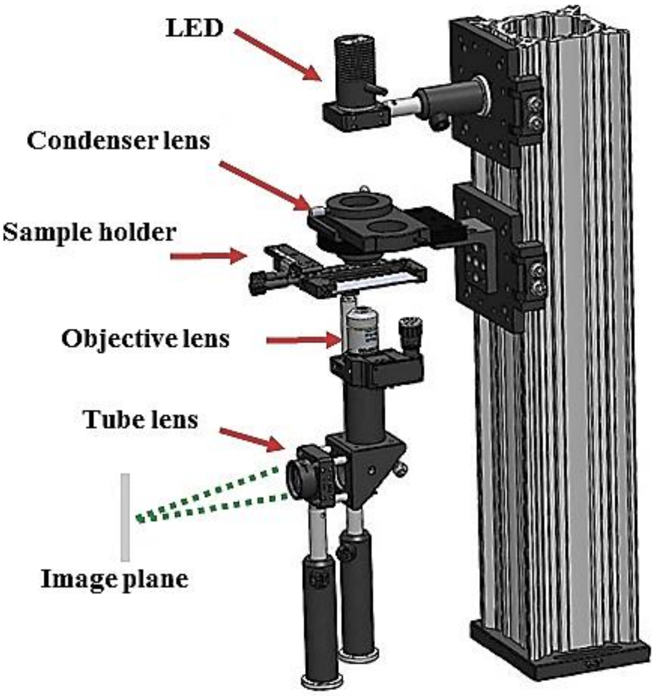

Figure 4.7 Phase imaging microscopy module.

4.5.2 LQPIM system based on twin-machined concentric mirrors

The PIM is an inverted microscope optically housed with twin-machined concentric mirrors in the PSM available in the back focal plane of the microscope for imaging optical transparent samples. A 2D sketch of the common-path LQPIM setup is presented in Figure 4.8. The size of the inner circular mirror (M_2) (5 mm Diameter, Stock No. #68-307, Aluminium Coated, λ/10 Mirror, Edmund Optics) and a corresponding hole (6.75mm diameter) in the centre of outer mirror (M_3) was calculated by imaging conjugated image planes using a standard 4f imaging system. A clear image of the conjugated annular ring (available in condenser lens) and the phase plate (inside objective lens) at the Fourier plane was recorded by the CCD camera with precise positioning of the lenses L_1 and L_2 (Figure 4.9). A magnification of 1.66x (approx.) from the PIM optics was also considered while measuring the dimensions from the image of the conjugated fields.

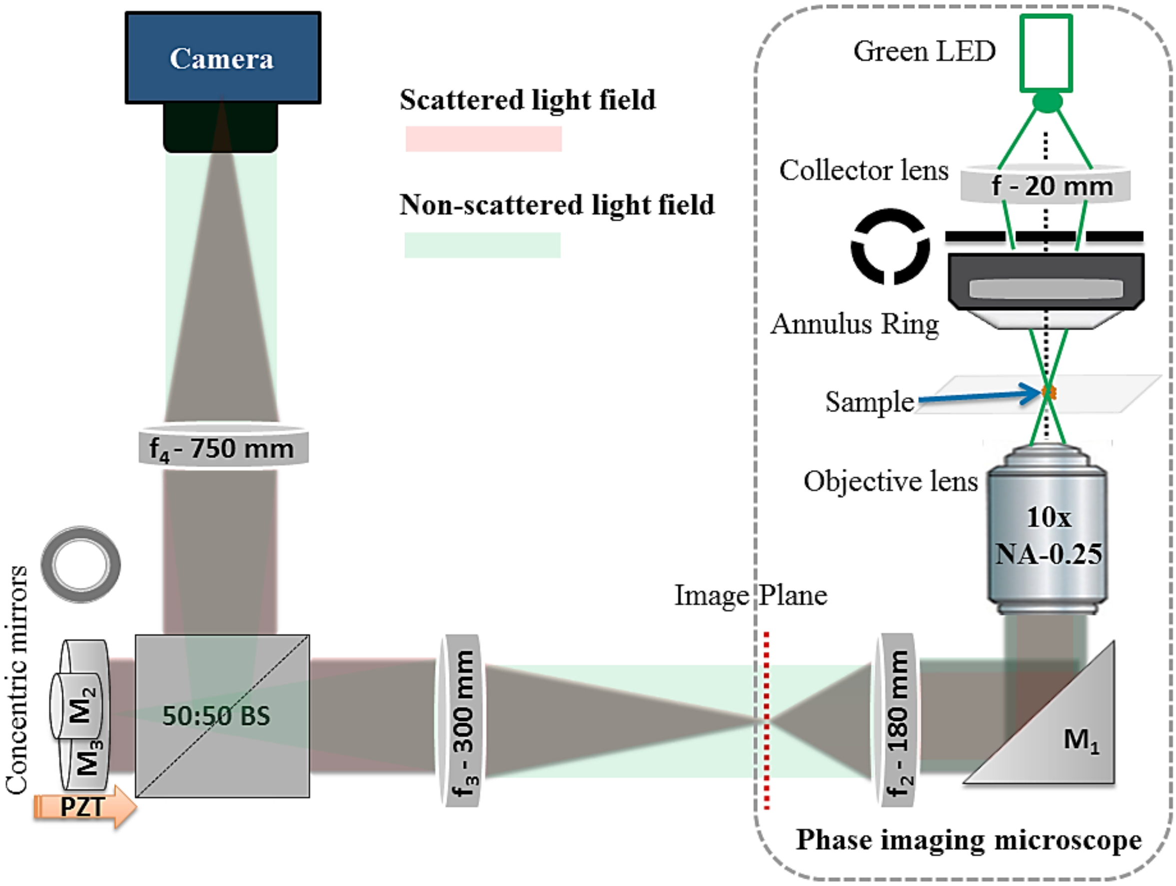

Figure 4.8 Schematic of common-path LQPIM system using twin concentric mirrors, M1-M_3 (mirrors), BS (Beam splitter) and PZT (Piezoelectric transducer).

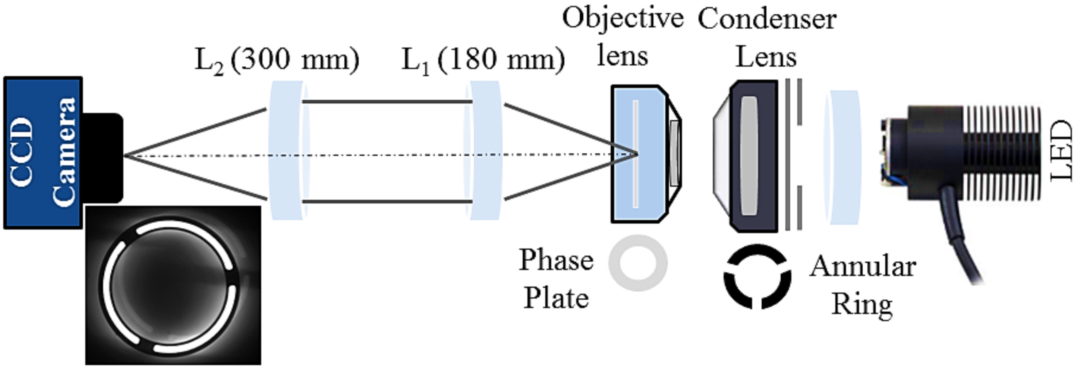

Figure 4.9 Conjugated annular ring (white) and phase plate (grey circle) at the Fourier plane.

The phase plate inside an objective lens is projected onto mirror M_3 hereafter known as the mirror annulus, and the remaining part onto the inner circular mirror M_2. A neutral density filter (0.2 optical density) was also applied to block the light outside of the arbitrary phase plate to balance intensity between the scattered and non-scattered image fields. The use of the mirrors in this way can be combined with a PZT driven high precision linear stage for phase stepping and hence, introducing a relative phase shift (Figure 4.10). The intensity sampling between above-mentioned image fields can be done as explained in Chapter 2, Section 2.4.2.

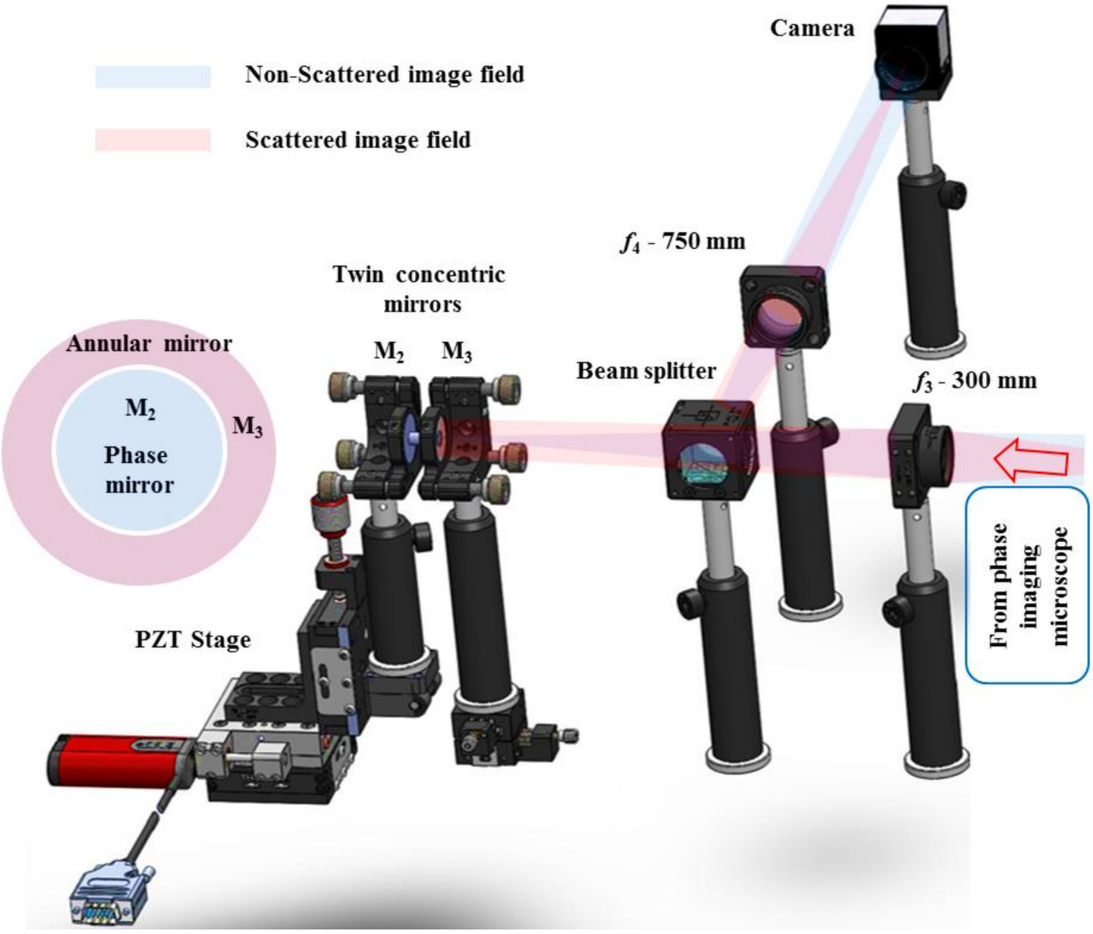

Figure 4.10 PSM based on twin concentric mirrors. M_2-M_3 *(Mirrors) and* f_3-f_4 *(focal length of relay lenses).*

The decomposed scattered and non-scattered image light fields were projected onto twin-machined concentric mirrors placed between the two relay lenses (f_3 and f_4) utilised in PSM at the Fourier plane of the LQPIM system for the introduction of predefined phase step. The spatial frequency components of the objects in the image field were laterally separated, reshaped and phase shifted by a fixed amount, for example π/2 from the twin concentric mirror setup. The phase delay between the scattered and non-scattered image fields was precisely modulated by driving the PZT installed in a high precision linear stage where mirror (M_3) was mounted using an NI-USB 6008 analogue output card. It is assumed that the PZT stack used had a linear characteristic between applied voltage and displacement which was confirmed by examination of the standard deviation of the phase shift angle, see for example the data reported in section 4.4. Finally, both image fields with added phase shift were superimposed at the CCD camera to produce a high contrast interference intensity image. The mathematical representation of the working principle of the LQPIM system based on twin concentric mirrors is presented in the Section 4.6. The complete bench-top optics of the LQPIM system based on twin concentric mirrors is presented in Figure 4.11.

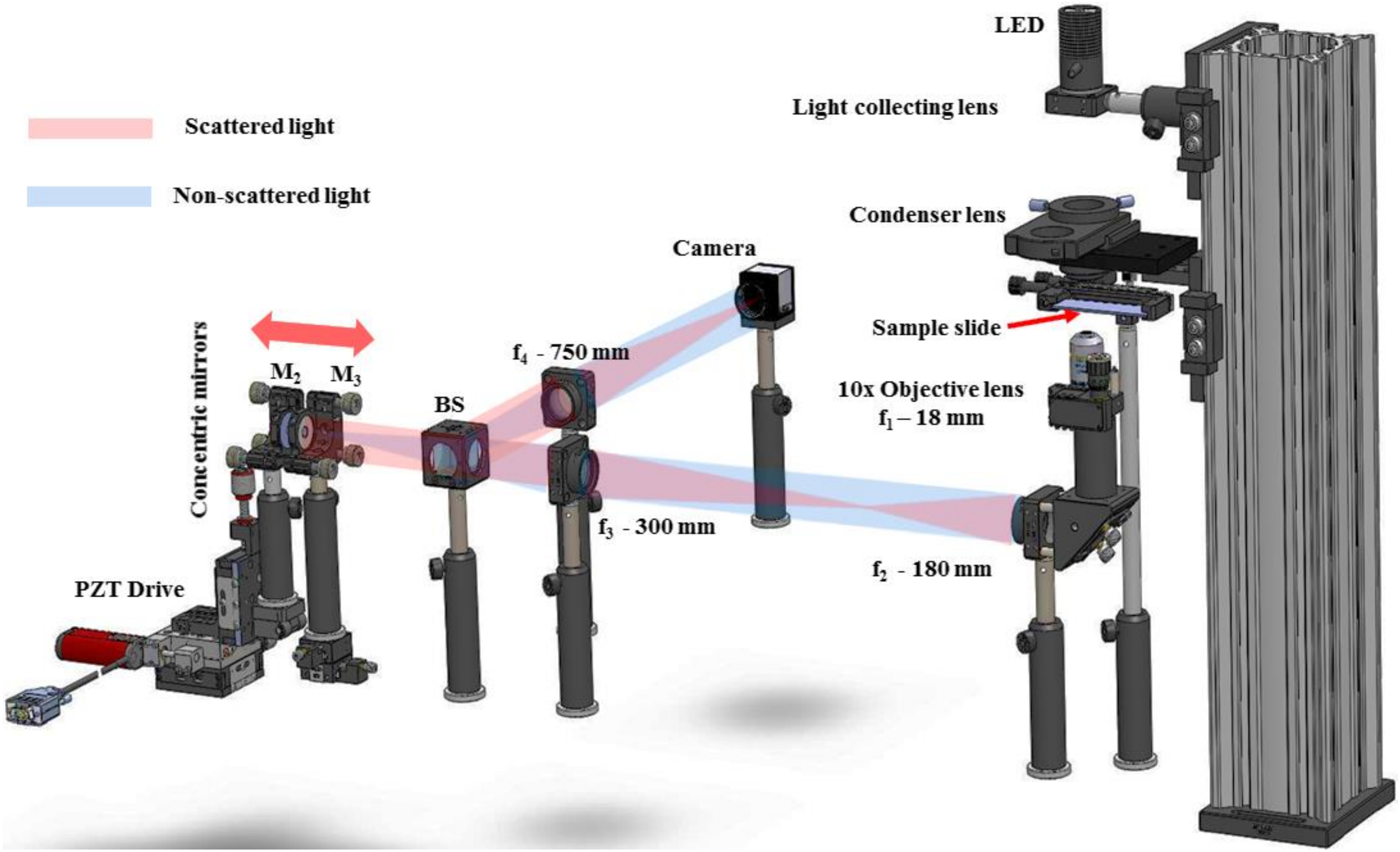

Figure 4.11 3D view of LQPIM system based on the twin-machined concentric mirrors in back focal plane. BS (50/50 Beam Splitter), LED (light emitting diode) and f1 - f4 (Focal lengths of imaging and relay lenses).

In practice, most commercial condensers position the illumination annulus at an intermediate numerical aperture of an objective lens. Therefore, the use of a mirror system with two-machined concentric mirrors further limit the NA of the system imaging system and therefore, worsen the lateral resolution. Another reason for worse lateral resolution could be the leakage of image fields in the space between the machined concentric mirrors. However, this approach has an advantage of common path optics, simple in design with less optical components and most importantly, the two-machined mirrors can replace the most expensive optical device, the spatial light modulator as used in other reported optical configurations [132]. The system developed is low-cost, approximately 10-15 percent of the cost of the quantitative microscopy methods based on phase modulations using an SLM [29] or wire grid polariser based camera used in the dynamic phase microscope [73]. In the twin-machined concentric mirror based LQPIM approach, the NA of the system was limited due to the available physical size of the mirror containing the central hole and varying the magnification in the relay system increased the sensitivity to tip and tilt mis-alignment of the two. The optical setup was also limited at the Fourier space to separate and modulate image fields efficiently; therefore, final interference image was affected. Furthermore, an outer part of mirror M_3 can be masked off at numerical apertures greater than that of non-scattered light field that was limiting the NA of the interference image. Difficulties in realising an experimental setup as well as limited NA meant that the phase maps obtained were of low quality. Hence, a more suitable approach that can spatially separate, modulate and reshape the scattered and non-scattered image fields at the Fourier plane inside a Michelson interferometer was developed. The description of the optics is presented in Section 4.5.3.

4.5.3 LQPIM optics based on laser-cut apertures

Laser-cut apertures (LCAs) were designed and applied directly onto the mirrors surfaces in the arms of Michelson interferometer in the PSM to solve the problem associated with twin-machined concentric mirror based phase shifting approach. The optimisation of the LCAs size was done precisely to mimic the functionality of the phase plate and the annular ring at the Fourier plane (Chapter 5, Section 5.2). In this case, a non-common path bench-top LQPIM system is configured as shown in Figure 4.12. The NA of the LQPIM optics is preserved such that the objective NA can be obtained in the interference images and the instability that can arise due to non-common path optics can be minimised by reducing the length of arms in the interferometer (Figure 4.12).

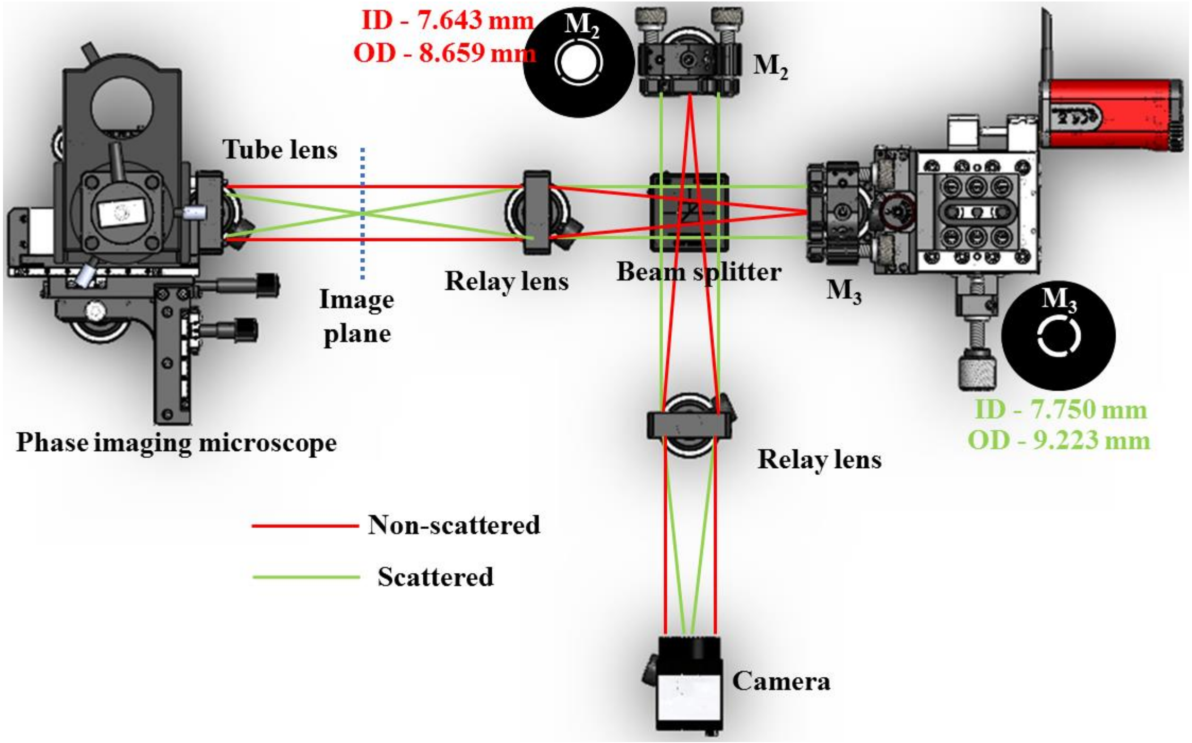

Figure 4.12 Ray optics of LQPIM system implemented with LCAs in PSM, M_2 - M_3 (Mirrors with respective LCA apertures)

The phase shifting components in LCA based optics are aligned on small breadboard installed with sorbothane feet (AV4, Thorlabs) with a proper shielding around Michelson interferometer using an opaque black hardboard (TB4, Thorlabs) to mitigate the possibility of errors due to mechanical vibrations and thermal air currents. The PSM with LCAs is a user-friendly robust method for phase shifting between the interference intensity frames from the scattered and non-scattered image light fields compared to the SLM based microscopy methods with negligible cost for phase stepping. In the LQPIM system, the user can introduce a predefined phase shift, for example $\pi/2$ or $\pi/3$ or $2\pi/3$ between the consecutive interference images by supplying a uniform increment step-wise voltage from the NI-USB6008 analogue output card. The PZT installed in a high precision linear stage holding the reference mirror (M_2) with an applied LCA phase mask was synchronised with CCD camera for phase stepping and image acquisition using an in-house LabVIEW program.

4.6 Working principle of LQPIM system

The complete 3D bench-top optics of LQPIM system based on LCAs applied in the arms of Michelson interferometer optics for phase shifting is presented in Figure 4.13. In this LQPIM optics, Koehler illumination was produced from a partially coherent source, $E(x,y) =$

$|E(x,y)|e^{i\varphi(x,y)}$ such as a green LED to illuminate the sample. The illuminating light field after passing through an annulus sitting in LQPIM condenser lens can be decomposed into scattered $[E_s(x,y)]$ and non-scattered $[E_{ns}]$ image light fields after passing through the objects present in the sample. The non-scattered light (from the background) was derived from the annulus in the condenser and passes through the phase plate in the objective lens onto mirror (M_2) while the scattered light (from objects in the sample) will be present across the entire Fourier plane (with varying amplitudes) on the mirror (M_3). It is accepted that it is not possible to obtain the entirety of these two waves independently of each other - part of the scattered light will overlap the image of the annulus in the Fourier plane together with the non-scattered image field. This is unavoidable - there is no plane in which these two beams can be fully separated in a Zernike phase contrast type setup. The phase plate inside the objective lens attenuates and out phased non-scattered light field by π/2 radians compared to the scattered light. The structural details of the objects in the sample modify the scattered image field while the non-scattered image field retains the background information. Both LQPIM optics based on twin-machined concentric mirrors or LCAs enables arbitrary user-defined phase shifts in the interference intensity images with help PSM in the back focal plane of the microscope. Therefore, both methods are capable of rendering quantitative phase maps from objects under examination. The quantitative phase image of the object can be approximated as an integral of refractive index difference between the test object and the surrounding medium and spatial variations in thickness across the specimen.

As shown in Figure 4.13, the non-scattered beam can be phase shifted at the Fourier plane before being combined with the scattered beam from the objects to form an interference image on the CCD camera. The mirror M_2 is moved in λ/4 steps such that the CCD camera could record all the phase shifted interference patterns. The intensity variations in the images were recorded on the CCD camera as a function of phase can be extracted as per Eq. (4.4).

$$I(x,y) = I_{ns} + I_s(x,y) + 2\sqrt{I_{ns}I_s(x,y)}\cos(\Delta\varphi(x,y) + n\varphi') \qquad (4.4)$$

where $\Delta\varphi(x,y)$ is the initial phase delay introduced by objects in the sample, φ' is the phase introduced experimentally in the sequential steps (*n = 0, 1, 2, 3, 4, 5.....n*) using the PSM available in LQPIM optics, $I_s(x,y)$ and I_{ns} are the intensity of scattered and non-scattered image light fields.

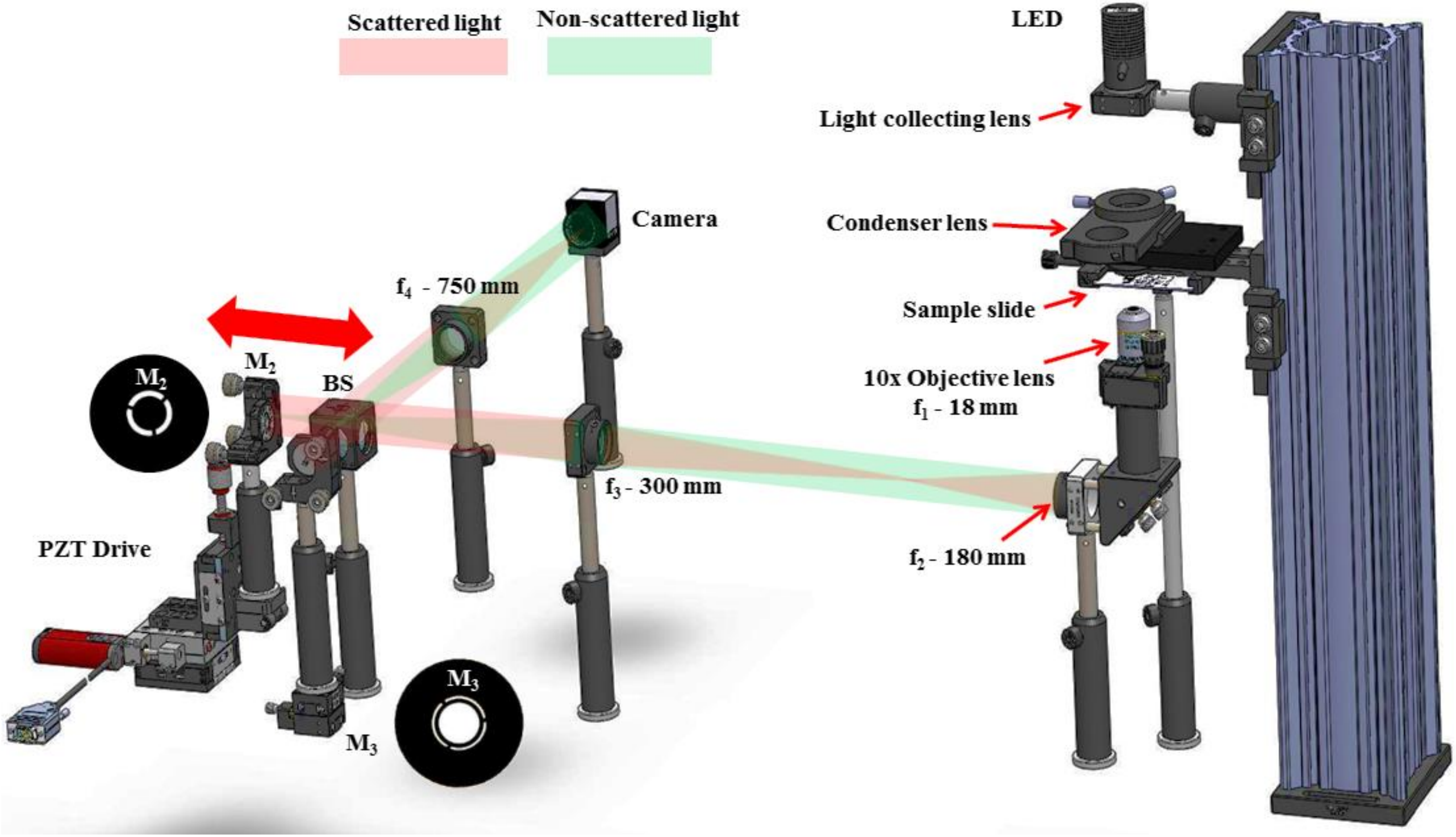

Figure 4.13 3D view of LQPIM system based on laser-cut aperture masks.
M_2 - M_3 (Mirrors with respective LCAs), BS (Beam Splitter), LED (light emitting diode) and f_1 - f_4 (Focal lengths of the relay lenses).

In this thesis work, several PSAs [97] are used to produce wrapped phase distributions from the recorded phase-shifted interference intensity images. The phase maps are used for performance assessment of LQPIM system. The phase distribution from the epidermis cells of *Allium cepa* presented in this thesis are reconstructed using $6+1F@60^{\circ}$ PSA. In this case, an irradiance pattern of the interference intensity in the phase-shifted images recorded at the CCD camera can be written mathematically from Eq. (4.5) to Eq. (4.11) using Eq. (4.4).

$$I_1(x,y) = I_{ns} + I_s(x,y) + 2\sqrt{I_{ns}I_s(x,y)}\cos(\Delta\varphi(x,y)+0) \tag{4.5}$$

$$I_2(x,y) = I_{ns} + I_s(x,y) + 2\sqrt{I_{ns}I_s(x,y)}\cos(\Delta\varphi(x,y)+\pi/3) \tag{4.6}$$

$$I_3(x,y) = I_{ns} + I_s(x,y) + 2\sqrt{I_{ns}I_s(x,y)}\cos(\Delta\varphi(x,y)+2\pi/3) \tag{4.7}$$

$$I_4(x,y) = I_{ns} + I_s(x,y) + 2\sqrt{I_{ns}I_s(x,y)}\cos(\Delta\varphi(x,y)+\pi) \tag{4.8}$$

$$I_5(x,y) = I_{ns} + I_s(x,y) + 2\sqrt{I_{ns}I_s(x,y)}\cos(\Delta\varphi(x,y)+4\pi/3) \tag{4.9}$$

$$I_6(x,y) = I_{ns} + I_s(x,y) + 2\sqrt{I_{ns}I_s(x,y)}\cos(\Delta\varphi(x,y)+5\pi/3) \tag{4.10}$$

$$I_7(x,y) = I_{ns} + I_s(x,y) + 2\sqrt{I_{ns}I_s(x,y)}\cos(\Delta\varphi(x,y)+2\pi) \tag{4.11}$$

where $I_1(x,y)$ to $I_7(x,y)$ are the intensity images, I_{ns} and $I_s(x,y)$ determine the DC and amplitude terms. The quantitative phase map of the epidermis cells of *Allium cepa* at each pixel point in the image is uniquely determined quantitatively as per [108] using Eq. (4.12).

$$\Delta\varphi(x,y) = \tan^{-1}\left(\frac{\sqrt{3}(I_2 + I - I_5 - I_6)}{-I_1 - I_2 + I_3 + 2I_4 + I_5 - I_6 - I_7}\right) \tag{4.12}$$

The cellular and sub-cellular structural organisation of the cell wall, cell membrane, the nucleus and nucleolus can be seen clearly in the epidermis cells of *Allium cepa* (Figure 4.14). In the phase measurement experiment, it is assumed that the integration period should be equal for all the captured frames by the detector and the phase shift between frames is known. The phase can be measured efficiently if the intensity signals modulate sufficiently at each pixel point in a detector between scattered and non-scattered image light fields. The modulation of the signals $[\gamma(x,y)]$ in the image field can be measured using Eq. (4.13).

$$\gamma(x,y) = \sqrt{Num^2 + Denom^2} \tag{4.13}$$

where Num and $Denom$ are the numerator and denominator, respectively from any PSA to calculate the wrapped phase maps and their values can be taken as per the utilised PSA (e.g. numerator and denominator terms from Eq. (4.12) can be used here).

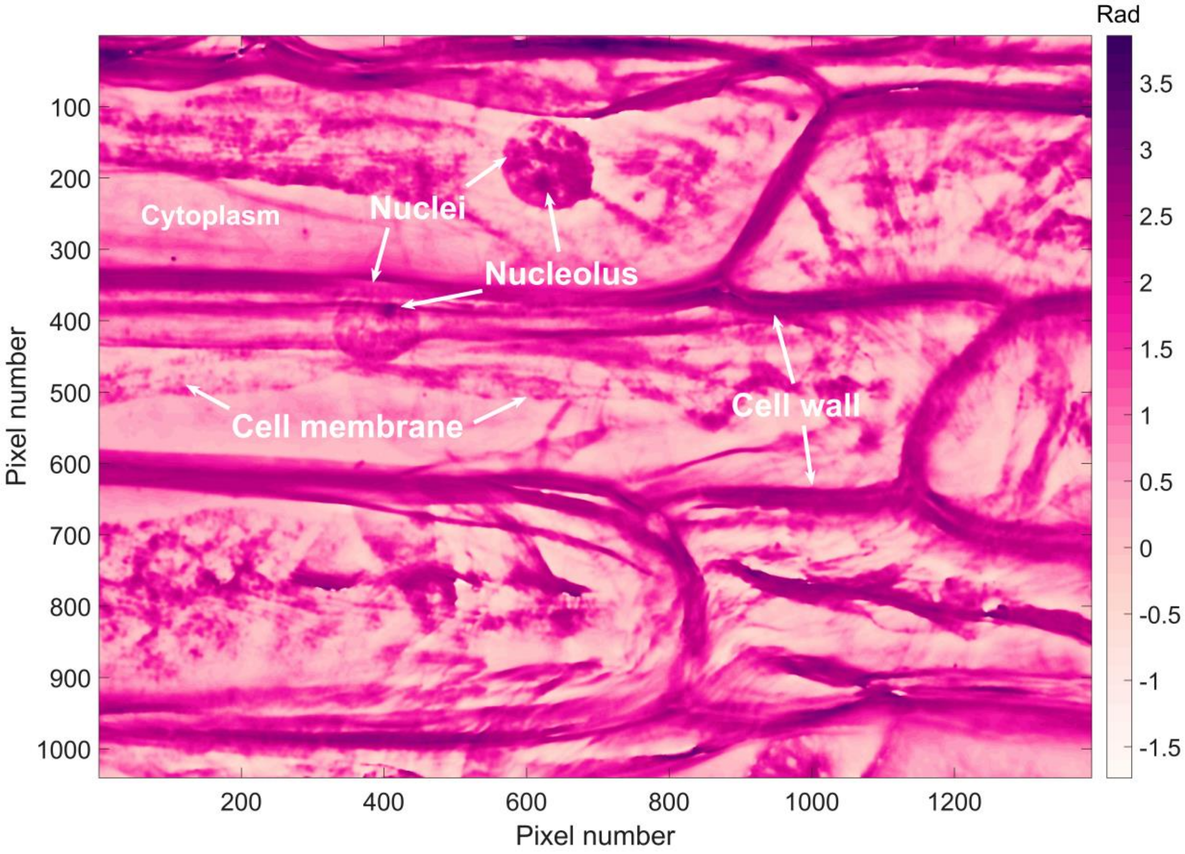

Figure 4.14 Quantitative phase image of epidermis cells of Allium cepa using 6+F@60°PSA from LCA based LQPIM system.

The phase distribution from the objects measured in this way enables the calculation of other valuable information, for example the change in optical path length, height of the objects and their refractive indices in certain cases. Spatial variations in the thickness and index of refraction of the objects in sample attenuates and causes in delay in illuminating light field passing through them and leads an OPD change compared to reference beam passes through the background / or surrounding fluid. The thickness $[t(x,y)]$ of the test object can be quantified after knowing the phase of the wavefront as per Eq. (4.14) and assuming that the refractive index difference is known as is the case for some of the results presented here (see section 5.5.1).

$$t(x,y)=\frac{\Delta\varphi(x,y)\lambda}{2\pi\left[n_o(x,y)-n_b(x,y)\right]} \tag{4.14}$$

Using this technique, a direct measurement of the test object relative to the reference surface can be possible. The overall height variations can be extended to larger than one fringe due to the nature of the arctangent function to calculate a phase i.e. wrapped modulo 2π. Therefore, a suitable phase unwrapping algorithm needs to be applied to get contiguous phase values across the sample [130], [133]. Furthermore, a 'null field' can be measured with no sample to compensate for any aberrations or alignment issues in the interferometer.

4.7 Image acquisition and image processing

The phase shifted interference images as required by a PSA were captured and stored using an in-house LabVIEW program. LabVIEW software gives simple block diagrams for non-specialist users to control the hardware of interest for a specific application. The front panel in LabVIEW is the output of the block diagrams. The block diagram window gives the programming environment to write specific codes for image processing [128]. The designed LabVIEW program controls and synchronises both the CCD camera using a frame grabber and the PZT installed in the high precision liner stage using a NI-USB-6008 analogue output device. At the start of imaging, the in-house software triggers the CCD camera to capture a single image, then changes the analogue output voltage from NI-USB-6008 card (driving the PZT) and then waits for 0.3 millisecond before capturing the next frame to allow the mirror position to stabilise and so on for the rest of the image sequence (Figure 4.15). In exploring the operation of the PZT the achieved phase steps in each of the PSA algorithms has been determined as both a mean and standard deviation of applied phase shift, see section 4.4. Similar quality results were obtained with all PSAs implying that over the range used (7 frames at 90°) the PZT could be assumed to operate linearly. 16-Bit phase-shifted interference images in the .png format were digitised and stored utilising a frame grabber. For the samples examined here, a post-processing approach could be adopted, however, it would be feasible to display wrapped phase maps in real time from the Labview program; phase unwrapping as a computationally intensive operation may be problematic to operate within a single frame period. The stored interference phase shifted images were processed in MATLAB to reconstruct the phase maps of the objects using a suitable PSA. The MATLAB code is presented in Appendix B.1. The phase maps were obtained after applying a phase unwrapping algorithm as described in [92]. The flow chart of unwrapping processes can be found in [134] is given (Figure 4.16).

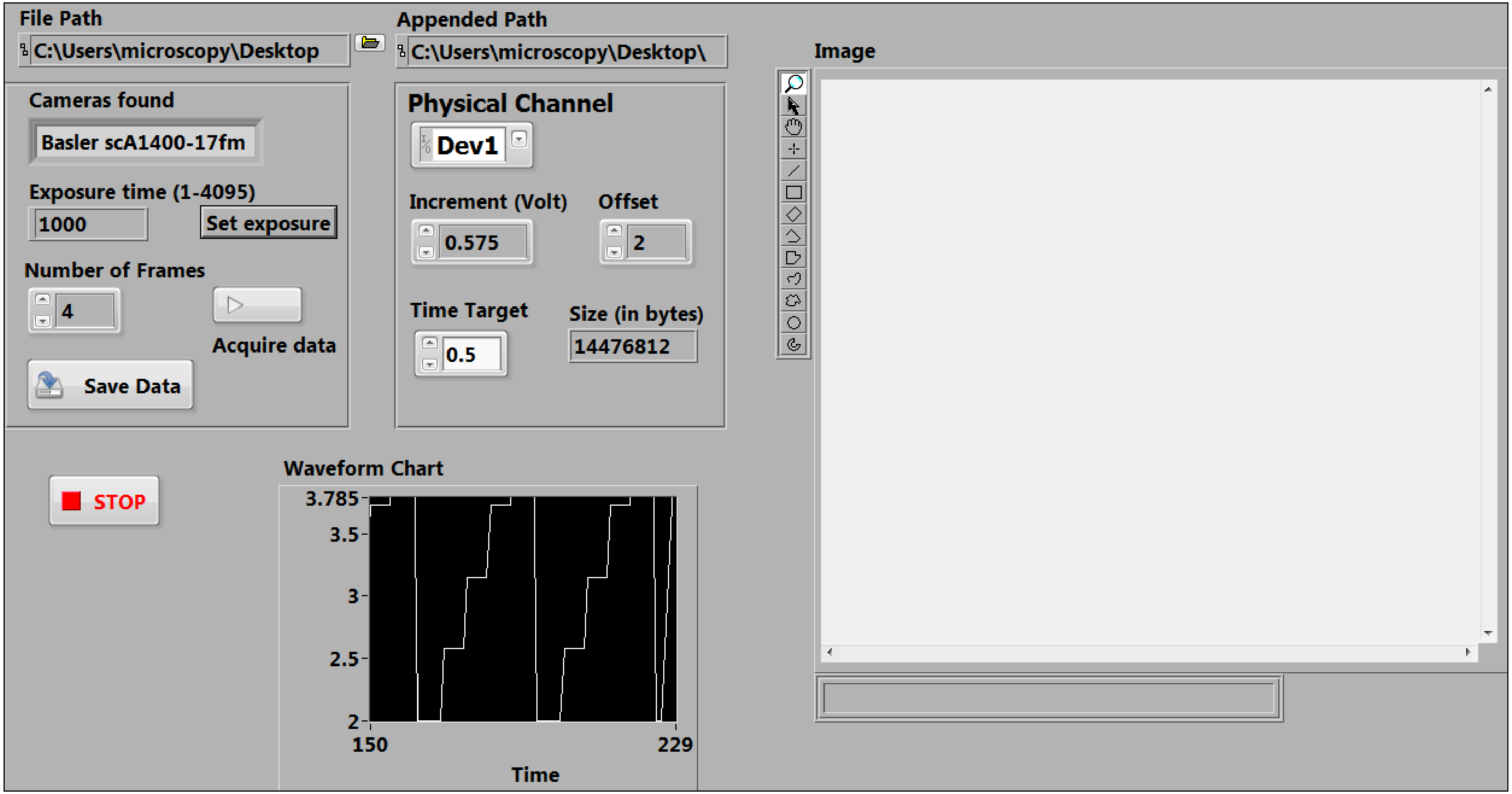
File Path: C:\Users\microscopy\Desktop

Appended Path: C:\Users\microscopy\Desktop\

Cameras found: Basler scA1400-17fm

Exposure time (1-4095): 1000

Number of Frames: 4

Physical Channel: Dev1

Increment (Volt): 0.575

Offset: 2

Time Target: 0.5

Size (in bytes): 14476812

Figure 4.15 Front panel view of an in-house LabVIEW program

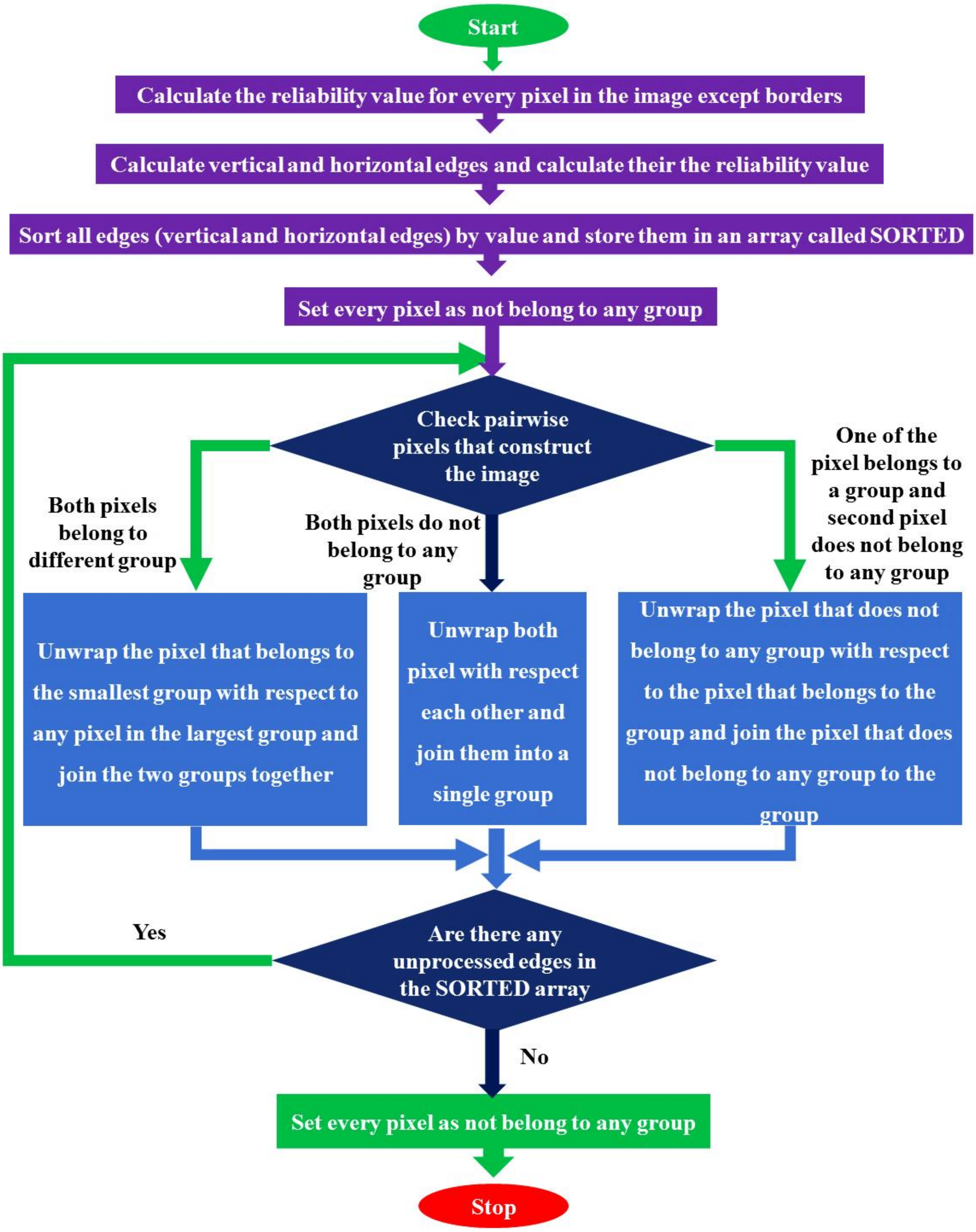

Figure 4.16 Flow chart of phase unwrapping process

4.8 Role of ‘halo effect’ in phase measurement

In the case of PCM, in general, ‘halo’ or ‘shade off’ artefacts can be seen around the edges of the phase objects in the image due to the large optical path length gradients across the objects in sample. Positive phase contrast produces a bright ring due to higher index of refraction objects than the surrounding medium while a dark ring is due to the low refractive index objects in the case of negative phase contrast. The appearance of either bright or dark rings around the edges is known as the 'halo' or 'shade off' artefact. Transparent biological samples produce a complex image due to a variety of cellular and sub-cellular structures with broadly fluctuating refractive indices. An example of the 'halo artefact' is shown in Figure 4.17, the regions are over enhanced and made relatively bright around (a) Human erythrocytes (red blood cells) and (b) HeLa cells cultured on glass coverslips.

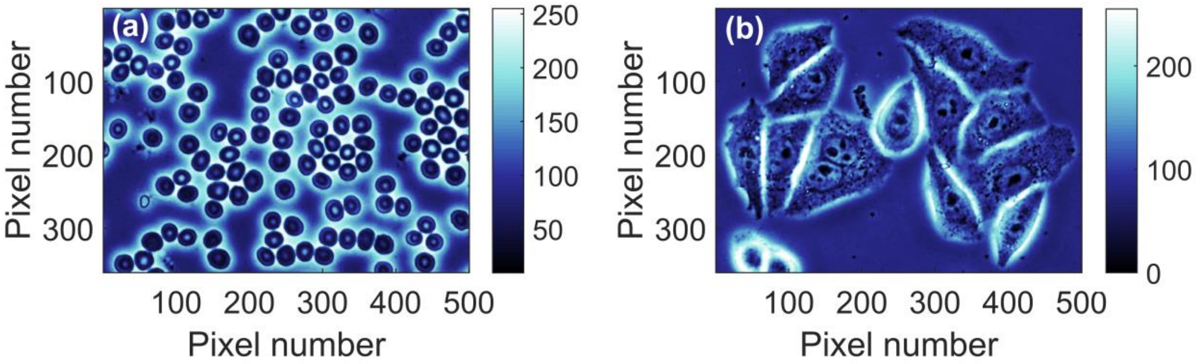

Figure 4.17 Halo artefact image from a phase contrast microscopy [e].

Technically, in the PCM the non-scattered or 0th order surround wave projected onto the phase plate inside the objective lens is 25 to 40% smaller than the actual width of the phase plate [49]. This is done to ensure that the phase plate affects the entire non-scattered wave and thus, it experiences reduction in amplitude and retardation in phase. Consequently, the phase plate also transmits a small amount of the scattered light from the specimen especially for larger objects. The larger objects, for example the nucleus and cells diffract light into small diffraction angles producing low-frequency waves compared to thin fine structures, for example the semi-permeable membrane and cause 'halo or shade-off' effect. The diffracted wavefront from the larger objects produce narrow angles due to which it falls within the object aperture occupied by the phase plate, as a result the image experiences artefacts around edges of objects.

To understand the effect of the 'halo artefact' on the image quality and phase determination problem in PCM microscopy, a mathematical model was simulated in MATLAB. The model considers a 0th order light wave passing through the sample that is assumed not to be diffracted or become attenuated by the objects in the sample and is referred to as non-scattered wave E_{ns} while the diffracted light from the objects is termed the scattered wave E_s (Figure 4.18).

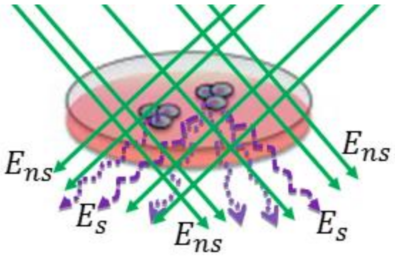

Figure 4.18 Light waves passing through a specimen.

To account for a small part of the scattered light that passes though the annulus ring at small diffraction angles typically from the larger objects an additional wave E_{sa} is also considered. All the waves are allowed to contribute to produce an interference. The interference between the scattered and non-scattered light waves forms the usual phase contrast image. However, the interference between the scattered and the low frequency scattered light-wave is an unusual phenomenon that produces a 'halo artefact' around the edges of objects in the specimen. The interference of all these light waves can be written mathematically as per Eq. (4.15).

$$I(x,y)=[A_{ns}e^{i\varphi_{ns}}+(A_s e^{i(\varphi_S+\varphi_j)}+A_{sa}e^{i\varphi_{sa}})]\times[A_{ns}e^{i\varphi_{ns}}+(A_s e^{i(\varphi_S+\varphi_j)}+A_{sa}e^{i\varphi_{sa}})]^* \qquad (4.15)$$

where $E_s = A_s e^{i(\varphi_s+\varphi_j)}$, $E_{ns} = A_{ns}e^{i\varphi_{ns}}$ and $E_{sa} = A_{sa}e^{i\varphi_{sa}}$ are the light fields that are scattered, non-scattered and scattered within the NA of the annulus ring, respectively. The MATLAB simulations quantify the uncertainty in the wrapped phase values as a function of intensity ratio between the two beams (Figure 4.18). The vertical axis shows the phase resolution expressed as a fraction of a fringe, i.e. 100 implies a phase resolution of 1/100th of a fringe to one standard deviation. It can be seen that the conventional interference intensity ratio between E_{ns} and E_s waves has almost no effect on the phase resolution; this is expected as the PSA is independent of these intensities. Furthermore, the phase resolution falls sharply downwards with increase in the amplitude E_{sa} with respect to E_{ns}. This is because the E_{sa} field will not be phase modulated with the non-scattered wave, however, will contribute interferometrically. The analysis emphasises the importance of matching the annulus size as accurately as possible to the phase plate and twin mirror / LCA sizes in order to minimise the effect. A 'halo' will be introduced implicitly in a Zernike PCM irrespective of the approach used to separate the scattered and non-scattered light fields and hence will affect the performance of SLM based PCMs in the same way.

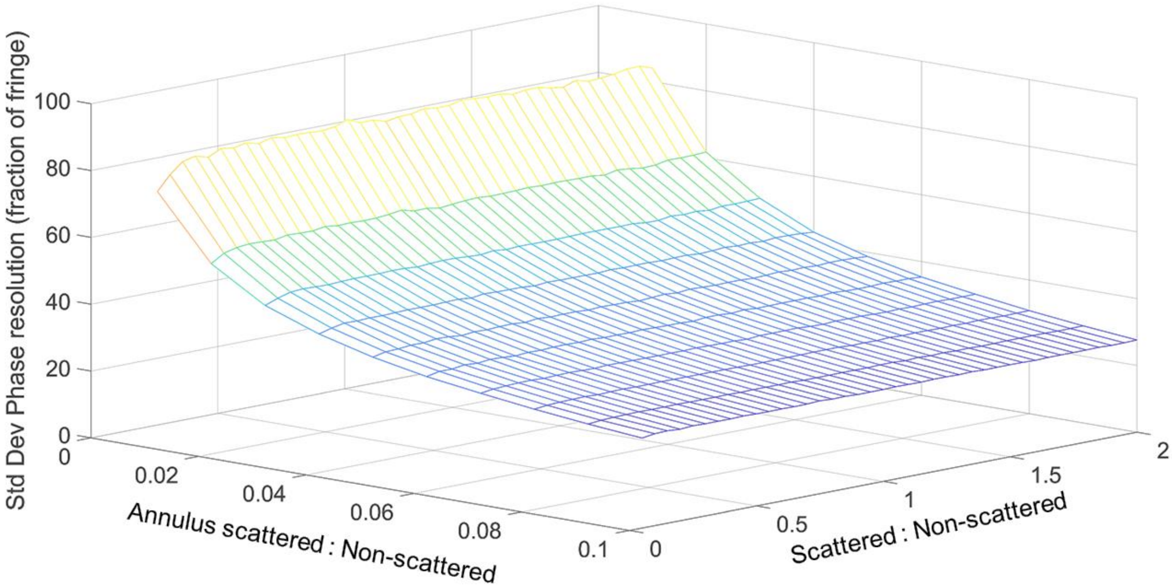

Figure 4.19 'Halo effect' on phase resolution by QPI microscopy as a function of intensity ratios

4.9 Summary

In this chapter, an optical design of the LQPIM system with the PSM optics either with twin concentric mirrors or with LCAs applied in the arms of a Michelson interferometer for phase modulation is discussed. Information on the optical components used in the bench-top geometry is also provided. The working principle of LQPIM system was mathematically derived based on two-beam interference phenomenon. The acquisition of the phase shifted interference images and their processing to extract phase distributions form the objects in the samples were presented. The role of the 'halo' or 'shade-off' effect on the phase extraction was also discussed.

Chapter 5. RESULTS AND DISCUSSION

This chapter presents the results obtained from a flexible LQPIM system and quantification on their phase measuring performance on optical thin and thick samples. Phase maps from a biological sample are presented to illustrate the capabilities of the twin-concentric mirror approach. The chapter deals with Michelson interferometer optics with laser cut apertures (LCAs), initially reporting on the optimisation of the size of LCAs based on measurements from resolution target. Glass beads were also utilised to assess the performance in measuring longer OPDs than have hitherto been reported using a quantitative phase measuring microscopes. The microscope with green LED illumination was used to image thin and thick optical label-free samples. The capability to resolve spatially fine cellular and sub-cellular structures of biological origin will be presented. Quantitative comparisons are made to explore the performance with narrowband laser illumination as well as using LEDs illumination for broadband and across the various phase stepping algorithms previously considered in this thesis (Chapter 3, Section 3.3). In all of the results, a standard 10x objective was used (without phase plate) to demonstrate the versatility of the approach and hence, the location of the non-scattered light field is defined by the annulus ring in the condenser.

5.1 Phase imaging using LQPIM optics based on twin concentric mirrors design

The LQPIM system based on twin concentric mirrors was tested on a Pinus leaf (a test sample slide) which had been stained to make it suitable for bright field imaging as well as phase contrast. Figure 5.1a) shows a bright field image using the full NA of the objective and shows clear structural features of the cells because of the staining applied. A single phase contrast image is seen in Figure 5.1b) where the effective NA of the scattered light is limited by the physical extent of the inner circular mirror in the optical setup. The phase shifted interference images were processed in MATLAB to reconstruct the phase distribution from the structural components of the Pinus leaf. The accuracy of the phase shift was evaluated by measuring the mean phase shift angle (α). An acceptable value of 90° ± 2.6 (Mean ± Std Dev) (Figure 5.2c) was achieved from the four phase stepped images recorded at the CCD camera. 4F@90° PSA was utilised to measure the phase distribution induced by the structural components of the Pinus leaf (Figure 5.2d). The structural features from the Pinus leaf cannot be easily quantified due to the poor NA utilisation in the twin concentric machined mirrors system that limited the lateral resolution of the system and was particularly challenging for the sample that contains many high-resolution structural features (compare Figure 5.1a) and Figure 5.2 b) and d).

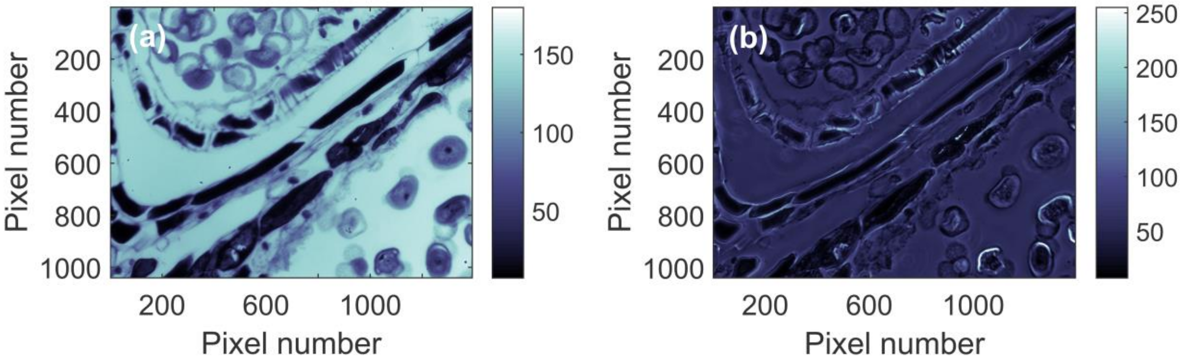

Figure 5.1 Structural features in Pinus leaf (a) – Bright field image, and (b) – Contrast enhanced image.

In the concentric mirror approach, the scattered light field from the inner mirror was modulated sufficiently but not from the outer edges of the phase plate (arbitrary) beyond the NA of the illuminating annulus on the circular mirror M_3 (Figure 4.10). Furthermore, the interference image captured by the CCD camera in image plane of LQPIM were not able to render the quantitative phase map of objects in the sample due to leakage of the scattered image into the space between twin-concentric mirrors and to the region on the outer circular mirror beyond the NA of the illuminating annulus. The use of custom condenser annular apertures that position the direct non-scattered light at the outer edge of the objective's NA would enable the system performance to be optimised while only using two mirrors.

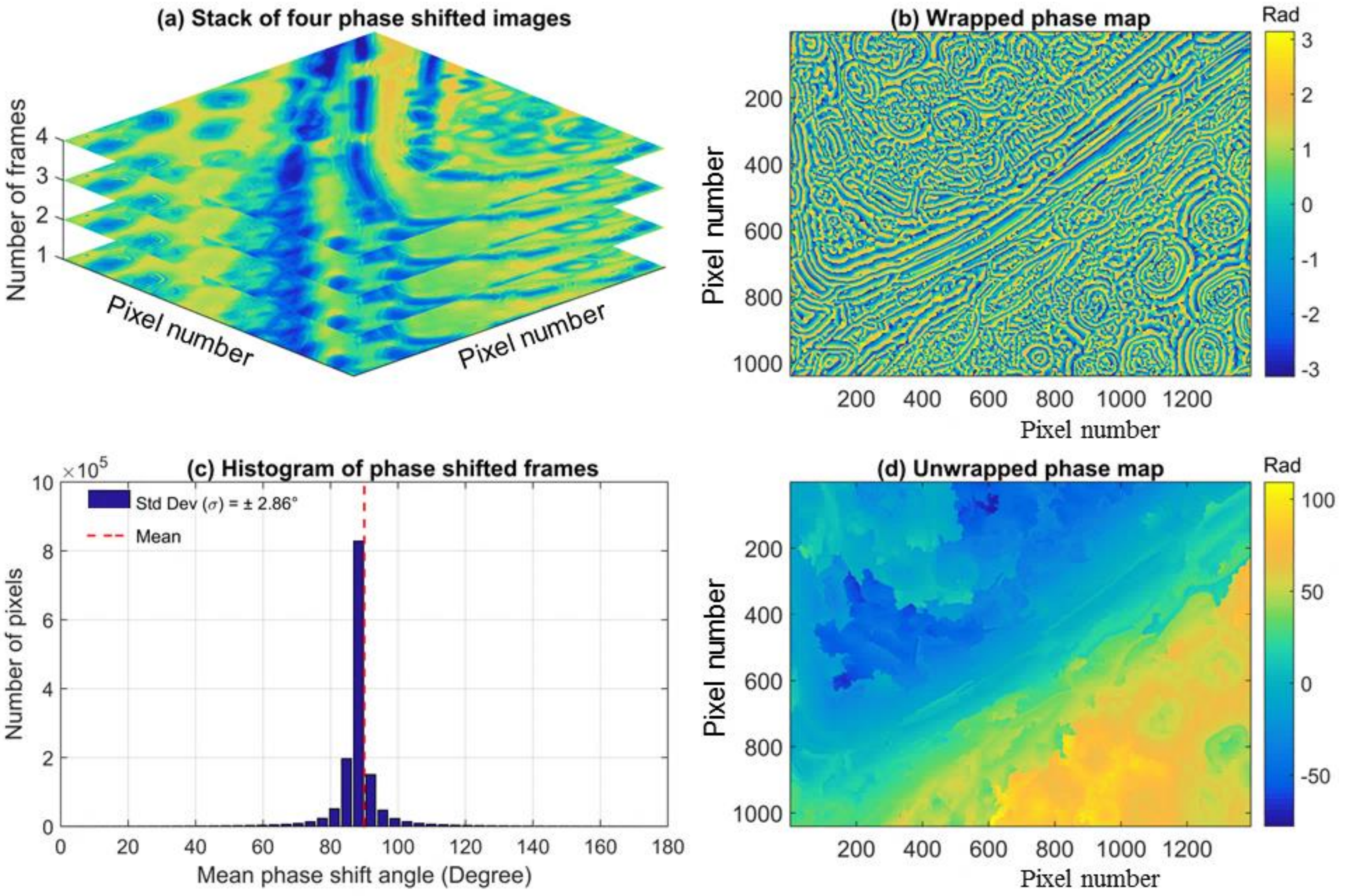

Figure 5.2 QPI data obtained using a Zernike-type LQPIM system based on twin concentric mirrors PSM from Pinus leaf.

5.2 Phase imaging using LQPIM system based on laser-cut apertures: aperture optimisation

In recent years, most of the QPI microscopy methods have been developed based on the use of a spatial light modulator, for example DPM, SLIM, WDT [16]. In these methods, the SLM was used either as a phase filter or as the phase shifter to modulate the scattered image field compared to the non-scattered field. The SLM based phase shift module in the back focal plane, of course, provides a common-path interferometry optics but have several limitations.

Firstly, to generate a distinct phase shift using an SLM, a precise calibration and optimisation of the SLM display are needed [103]. The optimisation can be a very complicated, high computation cost and time-consuming process. Standard SLMs offer up to 2π modulation across the visible spectrum but increasingly higher retardation devices to 6π are commercially available (https://holoeye.com/spatial-light-modulators/slm-pluto-phase-only/).

Secondly, the user needs to identify the precise location of the pixels corresponding to the fixed size of phase plate on the SLM display computationally [29]. Only selected pixels to modulate the phase between scattered and non-scattered image light fields at the SLM display are needed to be addressed with defined grayscale values to produce a phase change.

Thirdly and most importantly, the optimisation of the phase only SLM is not very robust because it introduces wavefront distortations due to the surface curvature [135] of the device itself that need to be compensated before being implemented. Furthermore, the calibration file used to produce a phase shift of $\pi/2$ will not be suitable for introducing phase shift of $2\pi/3$ or $\pi/3$. To achieve such discrete phase steps a new calibration will be required.

Finally, Michelson interferometer optics for SLM calibration cannot be accommodated easily in biological laboratories due to the need for specific optical components and very high-cost SLM device. It is also very clear from the literature that SLM based microscopy optics have been implemented with only three frames [136] or four frames at $\pi/2$ phase shift algorithms [29], [43], [96]. However, the performance with higher numbers of frames PSAs have not been reported yet in the context of microscopy and microscopy related applications – particularly for larger OPD ranges beyond those that occur from a single cell.

A robust and user-friendly low-cost phase shifting module is developed in this thesis (Chapter 4, Section 4.5.2 and Section 4.5.3) to reduce the cost of the microscopy optics for quantitative phase microscopy. The phase shifting modules were implemented in the back focal plane of PIM optics (Figure 4.7). The complete bench-top optics thus developed is described as low-cost quantitative phase imaging system. The PSM based on LCAs can introduce user-defined phase steps at the Fourier plane as required for any PSA (Figure 5.3). The PSAs failed to reconstruct the phase distributions from the high special frequency objects in the case of the twin concentric mirror approach due to poor cross talk between the scattered (from objects in sample) and non-scattered (from the surrounding background) image fields. The cross-talk between these fields can be minimised by applying aperture masks onto the arms of Michelson interferometer. Furthermore, the physical size of the aperture masks, equivalent to the annular illumination ring and the phase plate (in the case of a phase contrast objective in standard PCM) are very important to mask and mimic the light fields at the Fourier plane.

The physical dimensions for the annulus ring (CX41, Olympus) in the condenser (ID- 3.37mm and OD- 3.71mm) were known as per the data provided by the manufacturer, but then the data for the phase plate was not disclosed. Therefore, the image of the conjugated Fourier planes of the microscope where the annular ring and phase plate (10x phase objective lens, NA 0.25) were superimposed and an image was captured using a standard 4f imaging system at the CCD camera (refer Figure 4.9). The images of the initial and optimised LCAs are given in Figure 5.3. The physical positioning on top of each other in the Fourier space facilitates a high contrast phase image from the objects in sample, a critical requirement in PCM. The physical size of the apertures was measured from the pixels in the image to produce aperture masks using a laser cutter (VLS6.60, Universal laser systems). The measured size of the phase plate and the annular ring were supplied to the laser cutter for cutting the apertures masks from a thin black opaque construction paper (≤ 0.3 mm thick).

The aperture applied to M_2 is designed to isolate the non-scattered waves corresponding to the NA of the condenser annulus. The aperture at M_3 is configured such that the scattered waves at an NA lower and higher than that of the condenser annulus are reflected. The operation of each laser cut aperture was confirmed by inserting additional relay lens optics to form an image of the spatial frequency plane from each mirror in turn, see Figure 5.3a) - d). The geometry of the initial laser cut apertures were determined by calculation and gave the optical fields shown in Figure 5.3 a) and b) for the scattered and non-scattered fields respectively. There is crosstalk of the scattered light being observed in Figure 5.3b) which is intended to reflect only the non-scattered waves. Optimised geometry laser cut apertures were identified from these images resulting in the scattered and non-scattered fields in Figure 5.3c) and d) respectively. It can be seen that the crosstalk present in Figure 5.3b) has been removed in Figure 5.3d). The scattered light seen in Figure 5.3c) is from an increased area of the spatial frequency domain than in Figure 5.3a) and hence also has greater energy. Interference contrast can be maximized by balancing the irradiance of the scattered and non-scattered image fields and can be achieved by further reducing the open area of the aperture for the non-scattered waves (at M_2, Figure 5.3d). Phase shifts between the two waves are obtained by a PZT installed in a high precision linear stage, thus the system is very low-cost. The lateral resolution is determined by objective lens as the NA of the scattered waves is not restricted.

The non-common path setup is sensitive to mechanical and environmental disturbances but these effects can be minimized by reducing the length of the arms in the interferometer and with appropriate shielding around the beamsplitter, M_2 and M_3. Individual images of each LCA were obtained by using a blackout material in each arm of the interferometer in turn to capture the scattered and non-scattered intensity images separately at the CCD camera for assessment purposes (Figure 5.3). The sets of phase-shifted images from mirror M_2 and M_3 were used to extract several valuable parameters in order to quantitatively assess the performance of each LCA, for example two-beam intensity ratios ($\gamma \approx 1$) mean modulation depth across the full image field, and the standard deviation (σ) in the mean phase shift angle (α). These parameters play a very important role in the reconstruction of the phase maps of the objects present in the sample. A summary table of these performance metrics for each set of LCA apertures is presented in Table 5.1 with the optimum capability being that given from the aperture set 5 and 7.

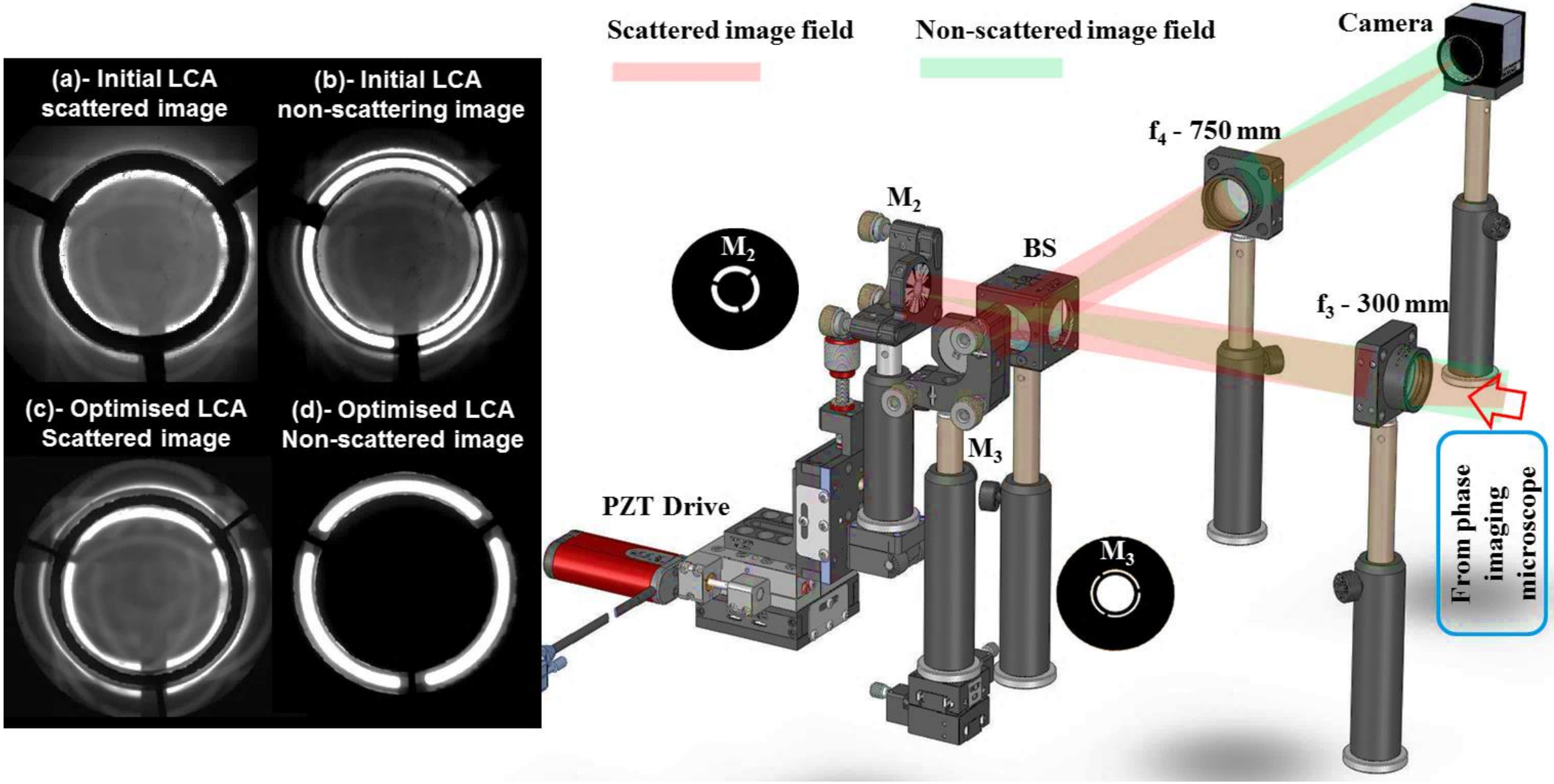

Figure 5.3 Phase Shift Module optics in a low-cost phase imaging microscope (right hand side); (a)-(b) the spatial frequency domains from the initial laser cut apertures corresponding to the scattered and non-scattered waves respectively; (c)-(d) the corresponding fields obtained from optimized laser cut apertures.

Table 5.1 Aperture size evaluation for high visibility and modulation depth

S. No.	**Phase ring size (mm)**		**Annular Ring size (mm)**		**Mean modulation depth (Grayscale)**	**Mean phase shift angle** $\boldsymbol{\alpha = \text{mean} \pm \text{std}}$	**Mean Intensity (direct light)**	**Mean Intensity (scattered light)**	**Visibility ratio** $\boldsymbol{\gamma \approx 1}$
	ID	OD	ID	OD					
1	7.780	9.670	7.749	8.885	395	90° ± 2.472	893	764	0.856
2	7.349	9.439	7.749	8.885	328	90° ± 2.840	836	652	0.779
3	7.349	9.239	7.749	8.885	387	90° ± 2.040	726	634	0.874
4	7.349	9.000	7.749	8.885	292	90° ± 2.526	793	636	0.802
5	7.750	9.223	7.749	8.885	402	90° ± 1.907	710	698	0.983
6	7.750	9.223	7. 742	8.675	371	90° ± 2.410	893	764	0.856
7	7.750	9.223	7.643	8.659	474	90° ± 2.223	769	698	0.907

5.3 Image processing

The phase map of the objects under examination were reconstructed from the sequential phase-shifted intensity interference images with respect to a suitable PSA. It was found experimentally that a 3x3 pixel-averaging filter applied to the phase stepped interference images gave benefits to the phase noise present in the images whilst not affecting the spatial resolution significantly. Hence, an averaging (3x3) Gaussian filter was applied as part of the image processing to produce the results in this chapter. The histogram of phase values from a full-field unwrapped image can provide information at every pixel in the image captured by a CCD camera. The histogram-based image filtering process was established to remove outliers from the unwrapped phase maps and hence, an optimised contrast in the resulting images was achieved. An example of an unwrapped phase map is presented in Figure 5.4 in the form obtained directly from the phase unwrapping algorithm.

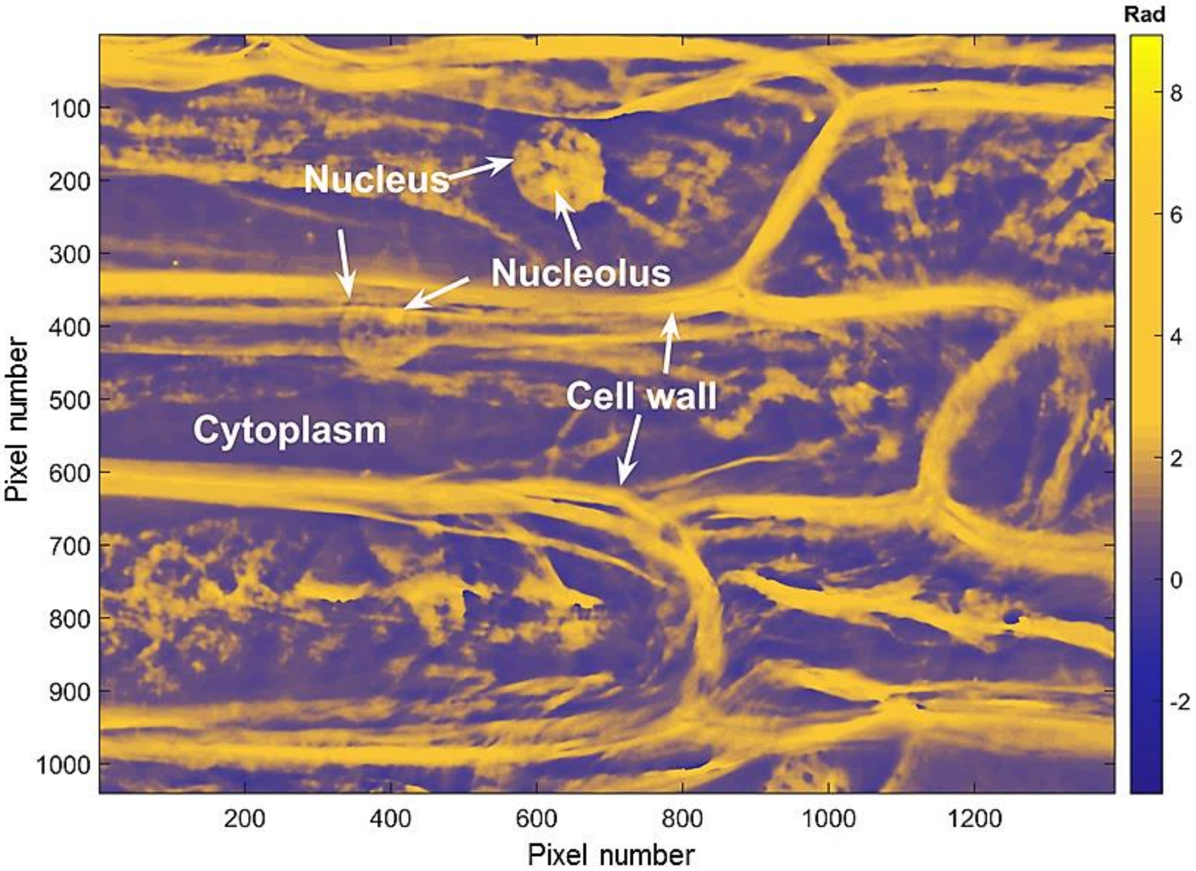

Figure 5.4 Phase image of epidermis cells of Allium cepa.

The spatially fine structural features of *Allium cepa* can be seen in the above quantitative phase image was produced using 6+1F@60° PSA. The contrast is not good enough to make visible some minute structural features, especially high quantity spatial frequency structures. The probable reason could be the presence of outlier frequencies that has not been removed during unwrapping process that are still present in the image. The outlier signals can be removed in the Fourier domain using the histogram based image processing. To increase the contrast and visibility of spatially fine cellular and sub-cellular structures, firstly the image was Fourier transformed and shifted in the centre. Secondly, a pupil function was applied to cut off the high-frequency signals and finally, the inverse Fourier transform was performed to get the final filtered image. The histogram of the phase data per bin after removing high-frequency outliers is shown in Figure 5.5.

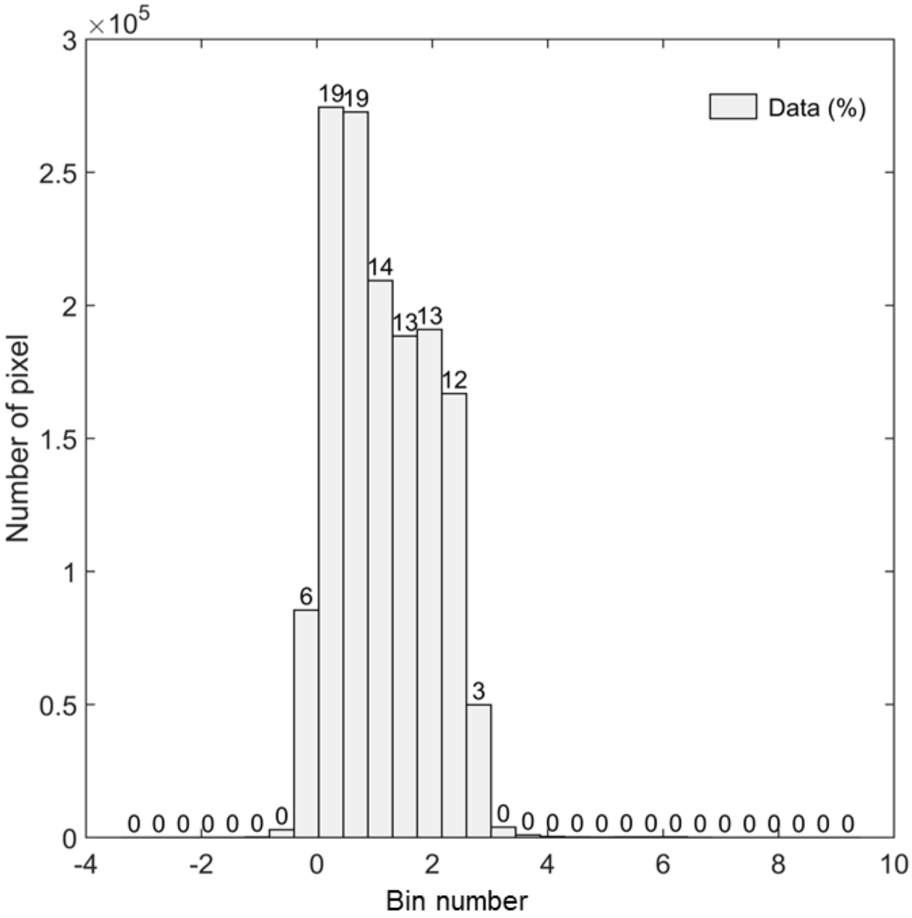

Figure 5.5 Histogram of phase map shown in Figure 5.4.

Based on the data a threshold was selected to remove the outliers from the given image (Figure 5.4), for example phase values ≤ -0.528 and ≥ 3.31 radians were set to NaN (not a number). The phase data was replotted to check the success of the applied threshold. This operation produces holes in the image due to NaN values (Figure 5.6).

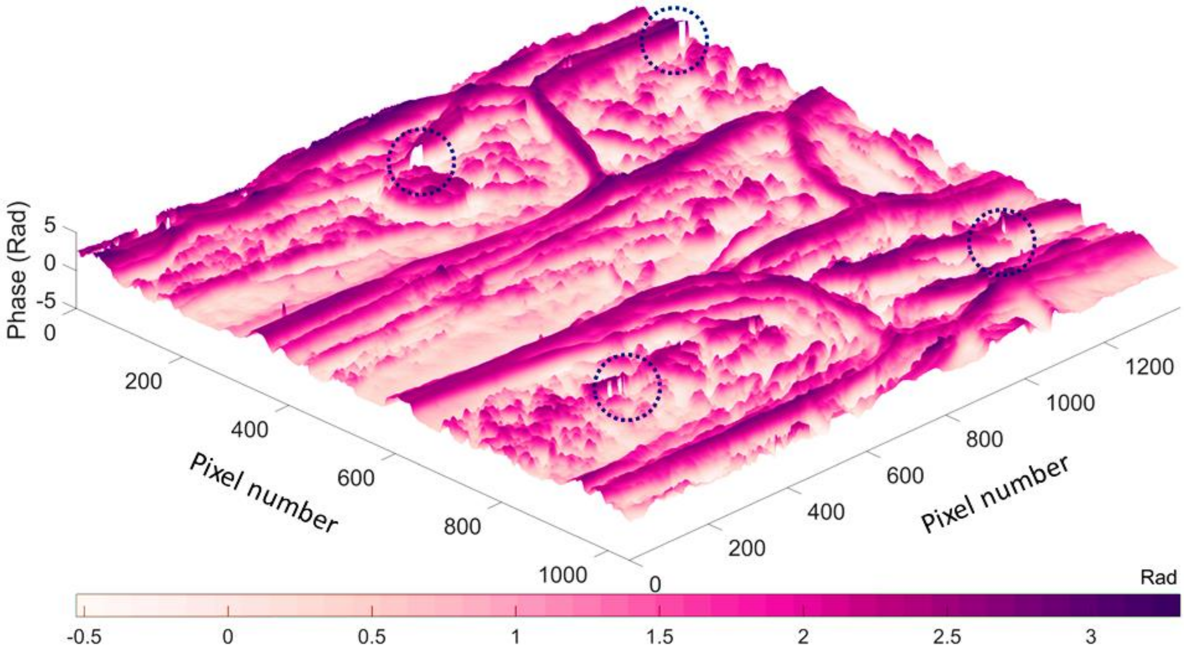

Figure 5.6 Phase map of Allium cepa cells with not a number (NaN) values highlighted in black doted circles.

A suitable computational approach was applied to fill the holes, for example the inpaintn function in MATLAB. The holes were filled based on extra or interpolating the local neighbouring pixel points in the image [137], as a result, high contrast phase image was obtained (Figure 5.7). A similar procedure was followed to produce high contrast quantitative phase maps of the objects in this thesis.

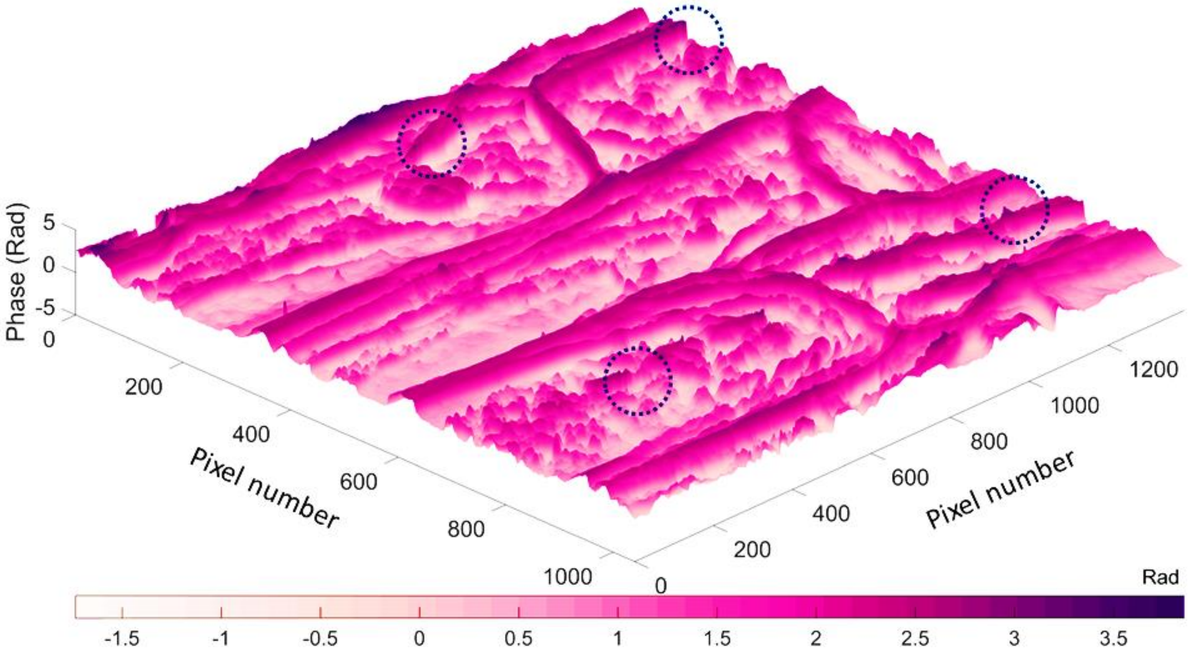

Figure 5.7 Fixed phase map of Allium cepa cells values highlighted in black doted circles.

5.4 Assessment of spatial resolution from LQPIM system

The spatial resolution limits the smallest structural features that could be sensed by an imaging system. The spatial resolution and the phase resolution worsen when random interferograms are produced from the scattered image field with imperfections in the optics and unwanted reflections from the various optical surfaces in the imaging system. Broadband light sources, for example from LEDs of either single colour or white-light can help to reduce speckles and coherent noise and hence, give improved spatial and phase resolution. Furthermore, background subtraction from a null sample field also helps to achieve good phase sensitivity over the measurements [138]. For the spatial resolution assessment purpose the NBS 1963A Test chart (R1L3S5P, Thorlabs) was illuminated under LQPIM system, and full field phase-shifted interference intensity images were recorded onto the CCD camera. Each line and space pair together on the NBS 1963A Target are called a cycle. The space between each line is equal in width to the line itself. Part of a 36 cycles/mm group consisting of five horizontal and five vertical lines on the test target were observed in the field of view. The 6+1F@60° PSA and other PSAs were used to reconstruct the phase maps. The uniform area on bright and dark strips in the phase image was selected to calculate the phase resolution from LQPIM system. The white line marked in Figure 5.8 occupies 431 pixels in the image that measures 4 full cycles in the group of 36 cycle/mm of the resolution test chart.

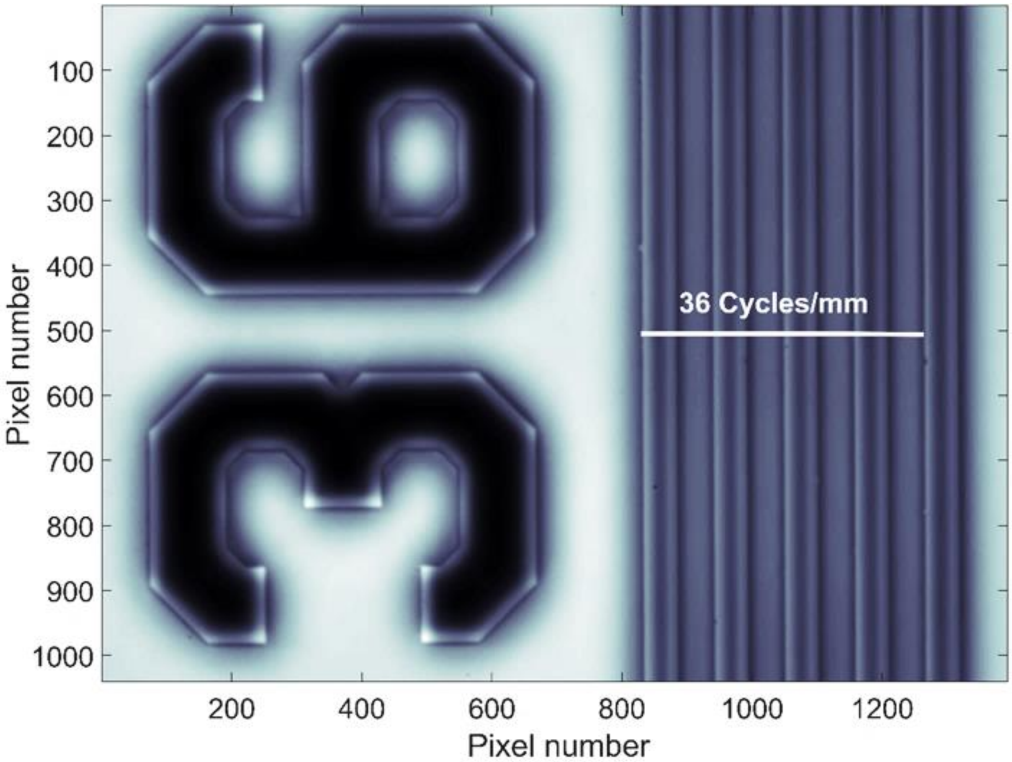

Figure 5.8 NBS 1963A Test chart with 36 Cycle/mm Marker (spatial resolution is 0.258 µm/pixel in object space, see section 4.3).

A scaling factor of 0.258 µm was calculated using the pixel size of the CCD camera (6.45 µm x 6.45 µm, Resolution – 1392x1040 pixels) and the magnification (25x) of LQPIM system. Therefore, 431 pixels for the white line corresponds to 111.198 µm. Further, these pixel values covers 4 full cycles of the test chart for the 36 cycles/mm group that measures 0.028 mm, hence, a standard value of 112 µm was expected. Using the measured and standard values for 36 cycles/mm group in test resolution chart an error of 0.716 % was predicted in the spatial resolution from LQPIM system.

5.5 Thickness measurement using LQPIM system

After determining the unwrapped phase distribution from the objects in the specimen the structural thickness variations can be retrieved using Eq. (5.1). The analysis requires values for the index of refraction for each structural component in the sample compared to the fixed index of refraction for the background medium/fluid. A known sample, for example glass beads (10 - 30 µm diameter, and RI - 1.51, Polysceinces, Inc) was used as the standard phase objects to measure the thickness variations from the measured phase distributions. A small pinch of glass bead powder was thoroughly mixed in glycerol (RI - 1.46572) to give the fine distribution of beads in the sample. A few drop of glass bead sample was placed on a glass slide using an Eppendorf micropippettor and a glass coverslip was placed and sealed with nail varnish. The 2D and 3D surface maps of the glass beads were reconstructed based on the captured phase-shifted interference intensity images with respect to a suitable PSA (Chapter 2, Section 2.5). Phase persuaded by the glass bead is directly proportional to the thickness $[t(x,y)]$ of the glass bead and difference in the index refraction of the glass bead and the surrounding fluid, for example glycerol in this case. The phase change can be calculated as per Eq. (5.1).

$$\Delta\varphi(x,y) = \frac{2\pi}{\lambda}\left(n_{gb} - n_{gly}\right)t(x,y) \tag{5.1}$$

where $\Delta\varphi(x,y)$ is the measured phase, λ is the wavelength of illumination source, n_{gb} is the refractive index of glass bead, n_{gly} is the refractive index of glycerol and $t(x,y)$ is the thickness of glass bead. A phase change of 11.93 radians, 12.17 radians, 14.97 radians and 16.54 radians were measured for 23.478 µm, 23.99 µm, 29.412 µm and 31.476 µm diameter beads, respectively (Figure 5.9), where the bead diameters were found directly from the (x,y) in the image.

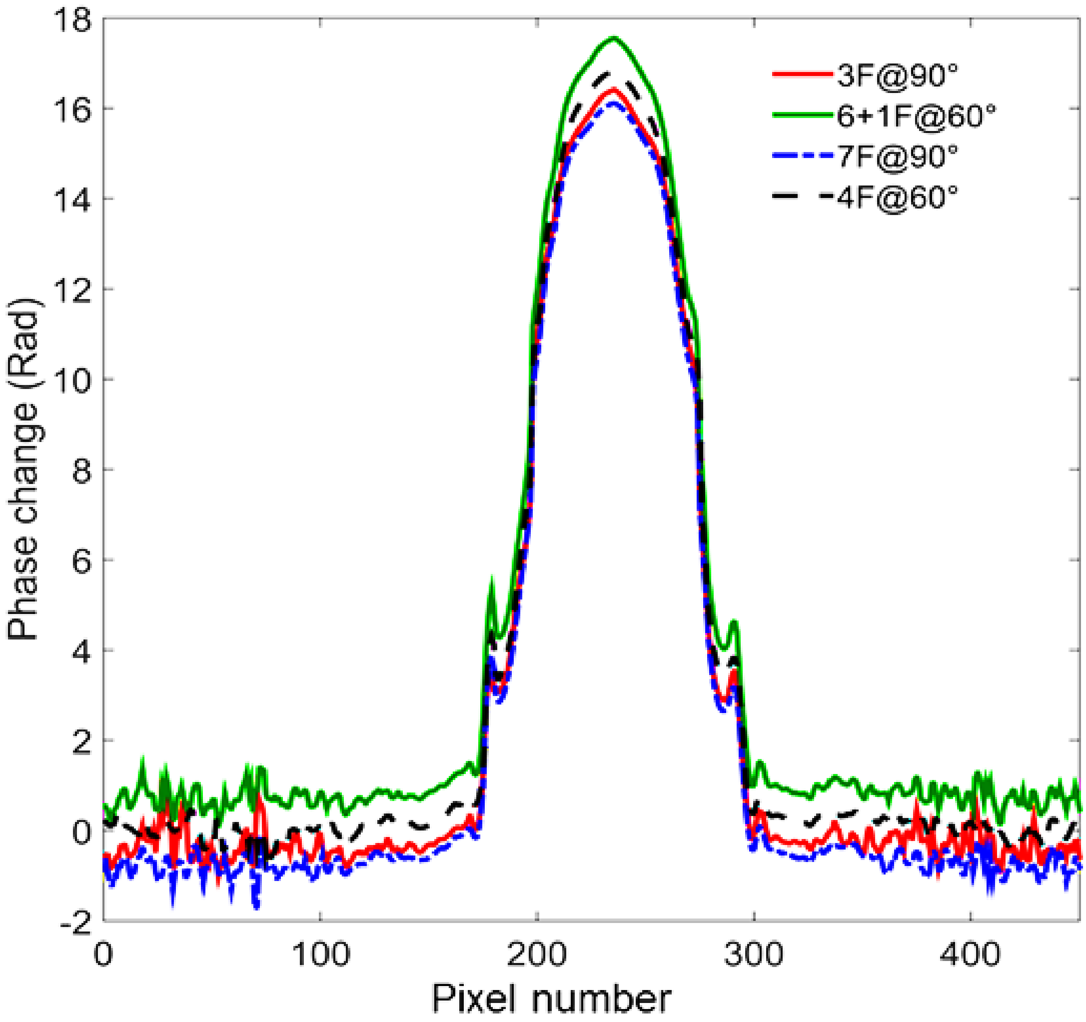

Figure 5.9 Phase profile of thick glass bead against pixel number on the CCD camera.

5.5.1 Uncertainties in the phase measurement

Errors in the experiment can be quantified by associating an uncertainty with each measurement. The quantification can be approximated based on either absolute uncertainty or percent uncertainty in the measured data from an object or source. In my case, the measured phase may experience uncertainties caused by various parameters, for example the refractive index of glycerol and that of the glass bead, a non-uniform size distribution of the beads due to manufacturing defects as well as the finite resolution of phase shift algorithm and the shot noise in the captured interference images. The uncertainties need to be identified and compensated in order to establish a good performing microscope. For this purpose, the theoretical and measured phase profiles for the glass beads over the measured size range are plotted in Figure 5.10.

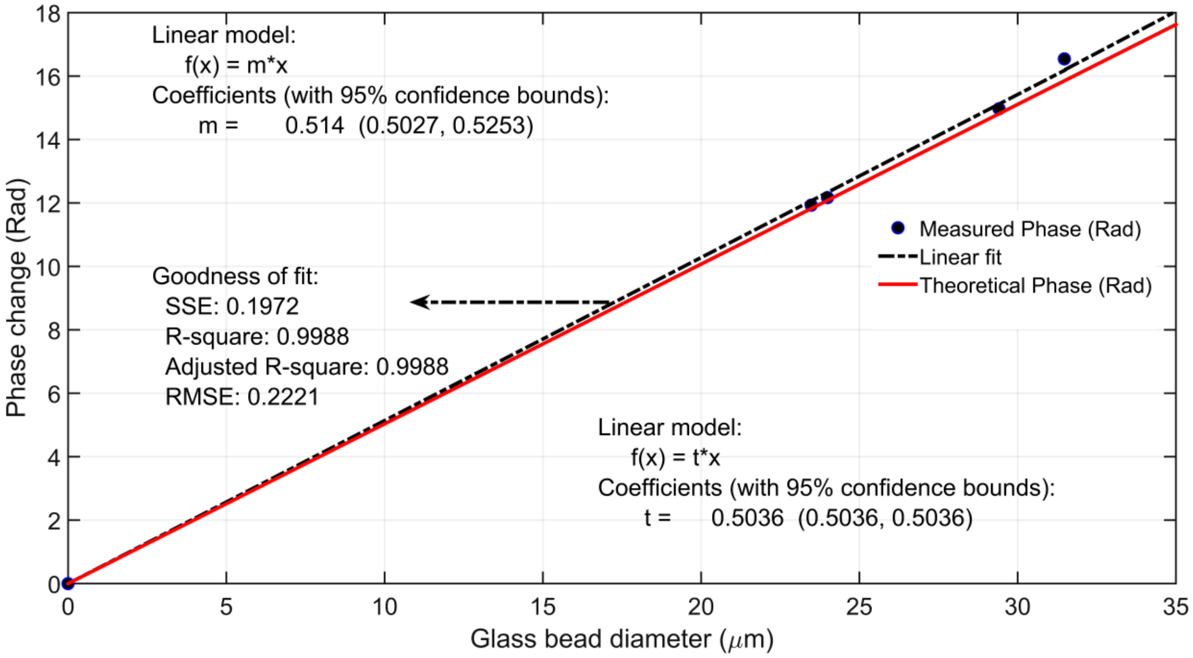

Figure 5.10 Theoretical and measured phase profile from the glass beads

The small fractional variations in these parameters are derived mathematically to determine the uncertainty in the calculated phase. Let one consider an uncertainty in phase calculation caused by the variation in diameter of the glass bead (i.e. thickness). The partial differentiation with respect to the thickness using Eq. (5.1) can approximate an uncertainty due to non-uniform size distribution of glass beads and it can be expressed as a fractional uncertainty as per Eq. (5.4).

$$\frac{\partial \Delta\varphi}{\partial t} = \frac{2\pi}{\lambda}\left(n_{gb} - n_{gly}\right) \tag{5.2}$$

$$\frac{\partial \Delta\varphi}{\Delta\varphi} = \frac{\frac{2\pi}{\lambda}\left(n_{gb} - n_{gly}\right)\partial t}{\frac{2\pi}{\lambda}\left(n_{gb} - n_{gly}\right)t} \tag{5.3}$$

$$\frac{\partial \Delta\varphi}{\Delta\varphi} = \frac{\partial t}{t} \tag{5.4}$$

Similarly, the partial differentiation of Eq. (5.1) with respect to index of refraction can also approximate for the uncertainty caused by the index of refraction. The uncertainty persuaded in the measurement can be approximated as per Eq. (5.6).

$$\Delta\varphi = \frac{2\pi}{\lambda}t(x,y)n_{gb} - \frac{2\pi}{\lambda}t(x,y)n_{gly} \tag{5.5}$$

$$\frac{\partial\Delta\varphi}{\Delta\varphi} = \frac{\partial n_{gb}}{(n_{gb} - n_{gly})} \tag{5.6}$$

The overall percentage uncertainty from all the sources mentioned here can be approximated using Eq. (5.7) assuming that each uncertainty is uncorrelated. A theoretical fractional error of 2.03% was determined based on Eq. (5.7) and assuming that the uncertainty in diameter measurement from the (x, y) image is 1 pixel at each end and the uncertainties in the refractive indices are half the least significant digit of the values quoted.

$$\frac{\partial\Delta\varphi}{\Delta\varphi} = \sqrt{\left(\frac{\partial t}{t}\right)^2 + \left(\frac{\partial n_{gb}}{n_{gb}}\right)^2 + \left(\frac{\partial n_{gly}}{n_{gly}}\right)^2} \times 100 \tag{5.7}$$

A total uncertainty of 2.065% was calculated from the theoretical and experimental phase measurements from the best fit slope in Figure 5.10. Further, other factors, for example mechanical vibrations, temperature fluctuation and environmental perturbation could also affect experimental data and may cause unavoidable uncertainties. The quantification of phase measurement was done from the phase-shifted interference image of the glass beads. A theoretical phase change of 15.8514 radian was expected from 31.476 µm diameter bead as per the standard value of refractive index but for the same diameter bead 16.54 radian phase change is measured (see, Figure 5.11) which is $\approx 4\%$ higher than the expected phase value. The same trend was followed by 23.478 µm, 23.99 µm and 29.412 µm diameter beads in the sample that confirms systematic error in the measured phase data (Figure 5.9). There are several possible reasons for the systematically higher phase change measured experimentally, notably the refractive index of glycerol is strongly dependent on low levels of water concentration (5% water content gives a refractive index change of 0.008) [i] and may be present in the experiments reported here. For the materials investigated there will also be some dependence on temperature with the refractive indices reducing as temperature increases. There are also steep phase gradients around the edges of the beads and multiple scattering of light may occur within the sample and from the surroundings. The steep gradients at the bead edge are a cause for concern for the phase unwrapping algorithm; however, as can be seen from the experimental phase profiles in Figure 5.9, the deviations observed are not of sufficient magnitude to give an unwrapping error. It is also possible that 'halo or shade-off'

---

[i] http://www.aciscience.org/docs/physical_properties_of_glycerine_and_its_solutions.pdf. Accessed on 04/10/2017.

effects will be present around the edges of the glass beads in the sample caused by unusual beam bending at the edges. In PCM, ‘halo or shade off’ effect is a general problem in the phase images due to overlapping of the scattered and non-scattered light fields in the Fourier plane. Such problems were not seen with biological data because the spatial gradients in optical thickness around the edges of the cellular and subcellular thin structures were much smaller. The biological sample was much thinner (OPD ≤ 120 nm) compared to that for the glass beads (OPD ≥ 1250 nm).

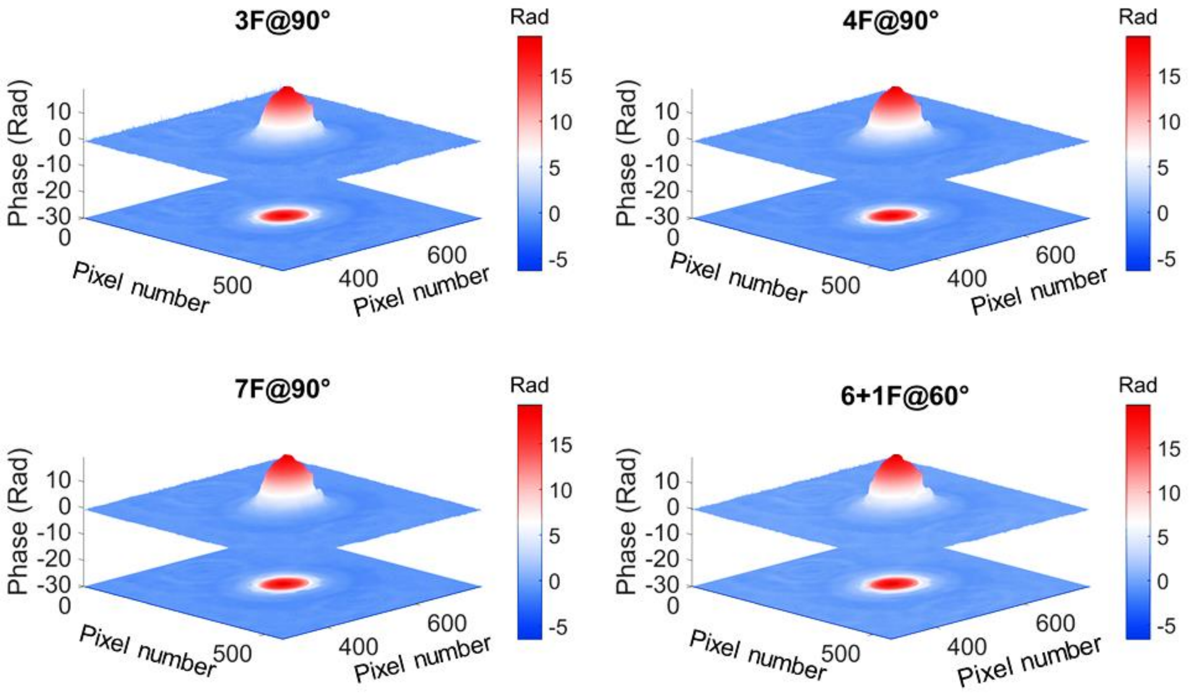

Figure 5.11 2D and 3D phase maps of glass bead (31.476 µm, diameter).

5.6 Implementation and assessment of PSAs in LQPIM system

The PSM attached in the back focal plane of LQPIM optics offers an opportunity to implement several numbers of pre-defined phase steps experimentally. The nominal phase step, for example $\pi/2$ or $\pi/3$ or $2\pi/3$ can be implemented as required by a particular PSA to calculate the phase distribution and to reconstruct 2D and 3D surface of the objects in sample. The phase values in the experimental data can be affected by shot noise, bandwidth, wavelength of the illumination source, mechanical vibrations and the aberration in the optics as well as sample temperature and water content. The detailed information on the phase measurement under green light illumination from a LED and a laser can be found in Section 5.6.1 and Section 5.6.3, respectively.

5.6.1 Phase noise assessment under green LED illumination

A green LED was used to illuminate the NBS 1963A Test chart under Kohler illumination optics of LQPIM system for the phase sensitivity analysis. The pre-defined phase shifted interference intensity images were recorded at the CCD camera using an in-house LabVIEW program. The recorded phase shifted intensity images corresponding to a PSA, for example 3F@90°, 3F@120°, 4F@90°, 5F@90°, 7F@90° and 6+1F@60° were processed in MATLAB to reconstruct the phase map. Phase noise was assessed by generating a cubic fit to the phase map of resolution test chart down a column of pixels corresponding to a line in the test chart (Figure 5.12) and evaluating the standard deviation of the residual errors [45]. Overall, 6+F@60° PSA has shown superiority in the reconstruction of 2D and 3D phase maps of structures on NBS 1963A Test chart such as digits and strips of the chrome coating. 1/1664th of a fringe noise was measured in column 1077 using the $6+1F@60^\circ$ PSA compared to 1/1338th of a fringe for 4F@90° PSA (Table 5.2, Figure 5.12 and Figure 5.13). A summary sheet of the PSAs assessed under green LED illumination is presented in Table 5.2.

Table 5.2 Performance of PSAs under green LED illumination (λ - 530 nm, FWHM - 42 nm).

PSI Algorithm(s)	**3F@90°**	**3F@120°**	**4F@90°**	**5F@90°**	**7F@90°**	**6+1F@60°**
Mean phase shift angle (α)	90.83°	120.66°	90°	90°	90°	60.14°
Std Dev in phase shift (σ)	$\pm 2.21^\circ$	$\pm 2.39^\circ$	$\pm 1.94^\circ$	$\pm 1.31^\circ$	$\pm 2.10^\circ$	$\pm 2.58^\circ$
Mean modulation $[\gamma(x,y)]$ of image field (grayscale)	380	448	437	437	433	537
Minimum modulation over row 210 (grayscale)	10	8	8	13	8	13
Phase noise for column 1077 (σ_φ, fringe fraction)	1/1001	1/915	1/1338	1/1438	1/1481	1/1664
Phase resolution for column 1077 (nm, λ = 530nm)	0.385	0.383	0.382	0.357	0.358	0.317

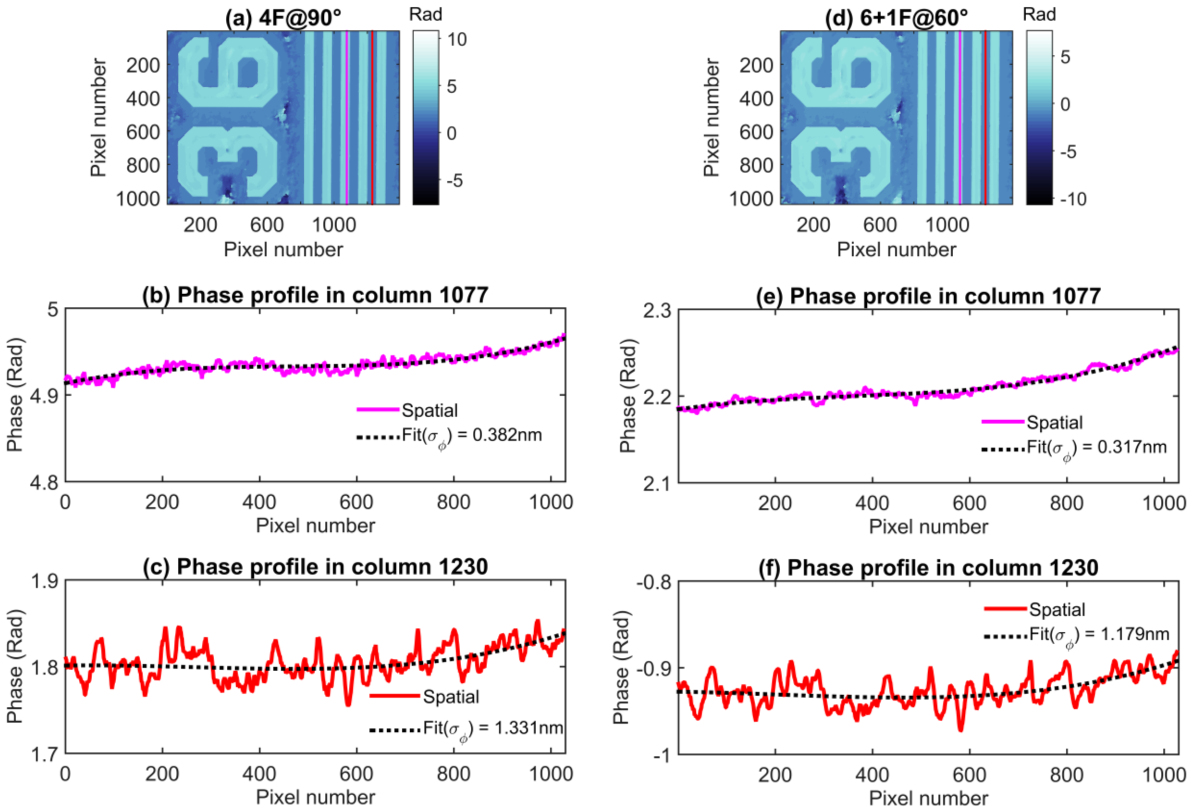

Figure 5.12 Phase resolution for column 1077 and 1230 under green LED illumination. In figure, pink line corresponds to column 1077 and red line corresponds to column 1230.

From Table 5.2 and Figure 5.13, it can be concluded that 4F@90° PSA and 6+1F@60° PSA offer better performance in terms of phase noise resolution and acquisition time (number of frames required) compared to the other listed algorithms. Phase noise sensitivity of 0.317 nm and 0.382 nm to one standard deviation were measured for column 1077 with utilising 6+1F@60° and 4F@90° PSAs, respectively for the test chart. These value are well-matched to the phase resolution of 0.3 nm achieved in the case of the SLIM method [29]. The noise level of 0.317 nm across the image field represents the limit of resolution in measurement of the optical path length. Furthermore, broadband illumination gives an advantage of speckle-free imaging to resolve fine spatial structures at nanometer scale. A better spatial resolution is achieved using a PSA with a higher number of frames and with smaller phase steps (i.e. 6+1F@60° PSA). A comparative assessment of the phase resolution achieved using various PSAs is presented in Figure 5.13 for column 1077 of the reconstructed unwrapped phase map of the test chart. The NBS 1963A Test chart used for the assessment of the phase sensitivity is, technically, an intensity object rather than a pure phase object. The spatial resolution and phase measurement for the strips and ‘36’ digit on the test chart are possible compared to a background area without no marking.

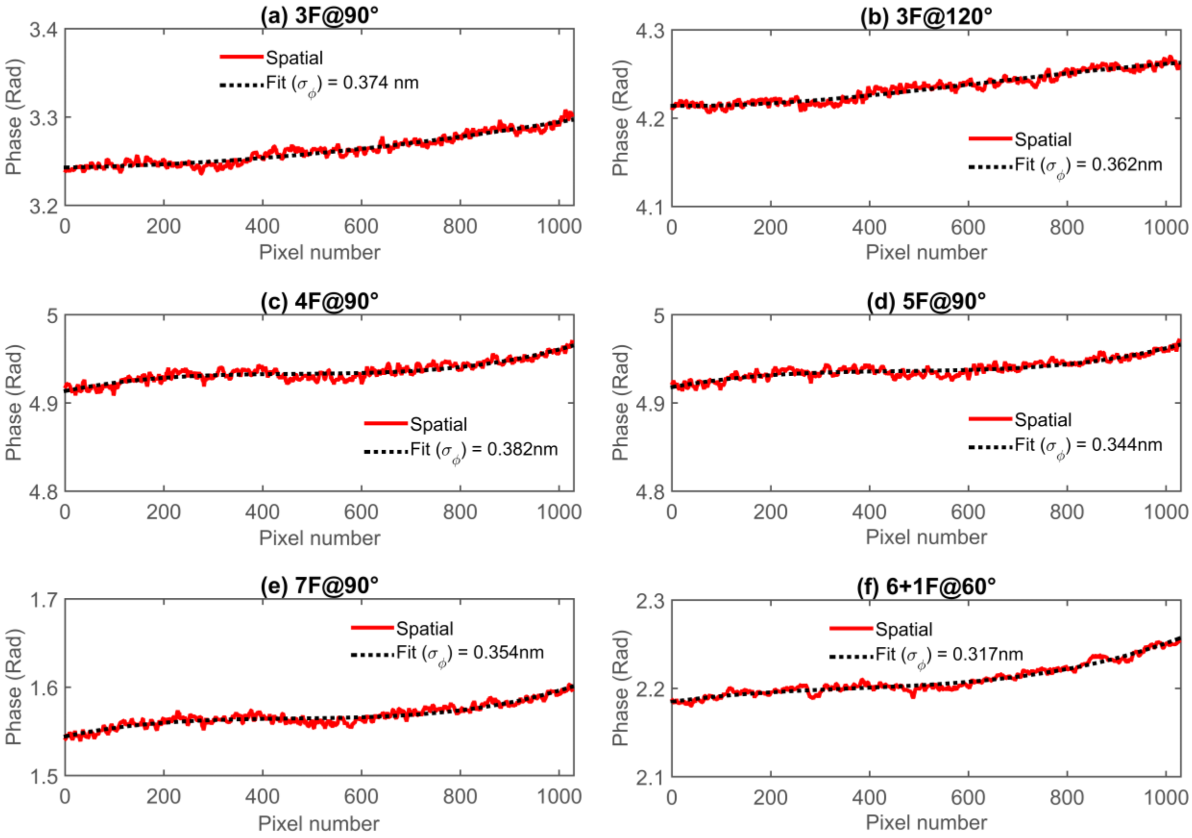

Figure 5.13 Phase noise analysis in column 1077 of NBS 1963A Test chart under green illumination from an LED.

The phase measurement depends on the scattered and the non-scattered intensity image field from the objects and their surroundings that provides modulation between them. However, some PSAs were failed to reconstruct the phase map in the areas where the intensity modulation is low (i.e. < 10 greyscale). In Figure 5.14, phase resolution problem can be seen in the central part (the region that is furthest from any markings) and the edges in the phase image, where the intensity modulation are poor or no scattering and light straight away coming from glass surface rather than a chrome coating surface. Such type of problem will not be present in the case of biological samples because if there is no cells or structural components present in the sample but has cytosolic fluid that contains metal ions, cofactors and mitochondria (typically 1000-2000 in members). Hence, the big wrap over points will not be there, however, steep gradients due to large variations in index of refraction and false warp over points may case similar problems. Such type of problems can be avoided by preparing sample slide using refractive index matching fluids, for example, glycerol or microscopy immersion oil.

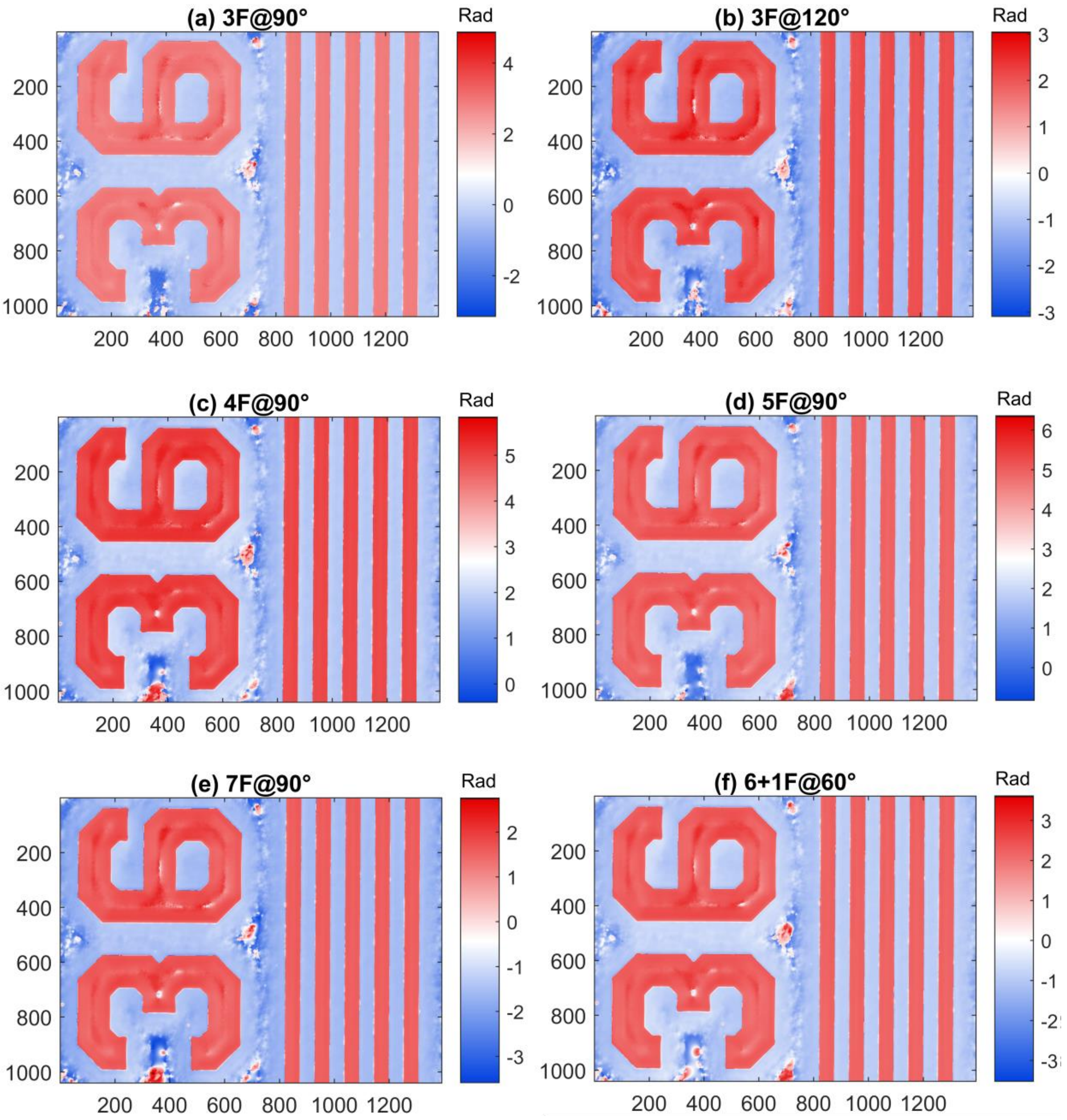

Figure 5.14 2D reconstructed phase maps of NBS 1963A Test chart using various PSAs under green LED illumination, x and y axis represents pixel numbers in all images.

5.6.2 Phase and thickness measurement from the biological samples using LQPIM system

The label-free epidermis cells of *Allium cepa* were used as an object of interest to assess the phase measuring capability from biological samples by LQPIM system. The sample slide was illuminated under the Kohler illumination mode of the microscope. The scattered and non-scattered image fields decomposed by the objects in the sample were received via the standard objective lens (10x, 0.25 NA) in the back focal plane at the PSM for spatial separation, reshaping and phase modulation in the Fourier plane of the microscope. The phase shifted interference intensity images from PSM were captured by the CCD camera available in the LQPIM system. The CCD camera and PSM were digitally programmed and synchronised using an in-house LabVIEW program to capture and store temporal phase-shifted interference intensity data continuously without losing any frame. The stored images were retrieved and processed in MATLAB using PSAs described in [48], [97] to render 2D and 3D quantitative phase maps at nanometre scale of the spatially fine transparent biological structures on the sample slide, for example cell membrane, cell wall, the nucleus the and nucleolus (Figure 5.15).

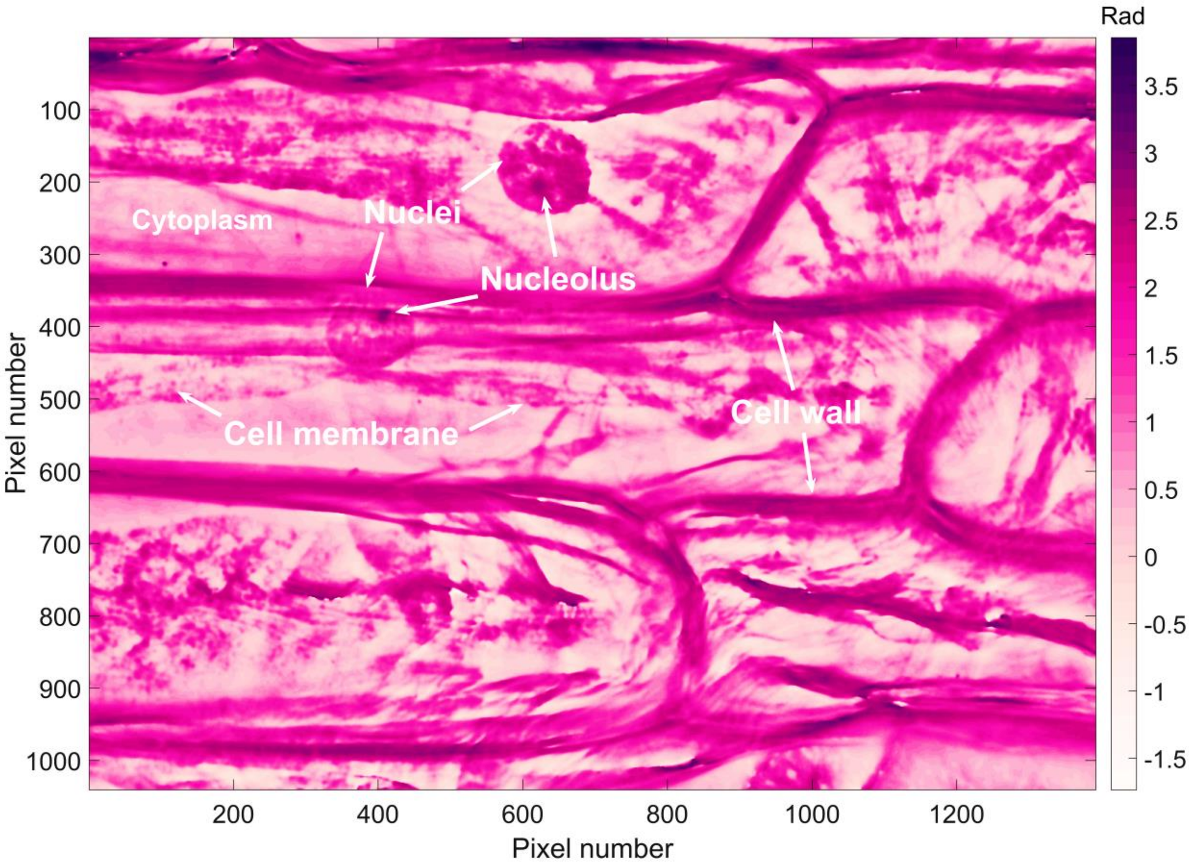

Figure 5.15 Quantitative phase map of epidermis cells of Allium cepa rendered using 6+1F@60° PSA.

A voltage of 0.32 V, 0.43 V and 0.61 V can be applied to move the PZT installed in the linear stage to produce phase steps equivalent to $\pi/3\,,\pi/2\ and\ 2\pi/3$ radians respectively, at the Fourier plane utilising PSM. The sequential interference intensity images were recorded to measure phase values and to reconstruct 2D and 3D surface maps of spatially fine biological structures. A good performance was observed from 6+1F@60° PSA compared to the other PSAs based on a qualitative inspection of the unwrapped phase maps (see Figure 5.16). If the signal modulation depth is low, for example a value < 10 - 15 grayscale, the phase unwrapping algorithm struggles to quantify the phase jumps and hence, were failed to produce an appropriate phase map. Nearly zero-fringe modulation between scattered and non-scattered image light fields, dirt on the sample slide and vibrations in the optical geometry can affect the signal modulation depth in phase imaging microscopy. A clear evidence of phase unwrapping process failure can be seen in the south-west area of Figure 5.16(b) (between rows 750 and 100 and column 0 to 500), where the phase was reconstructed using 3F@120° PSA.

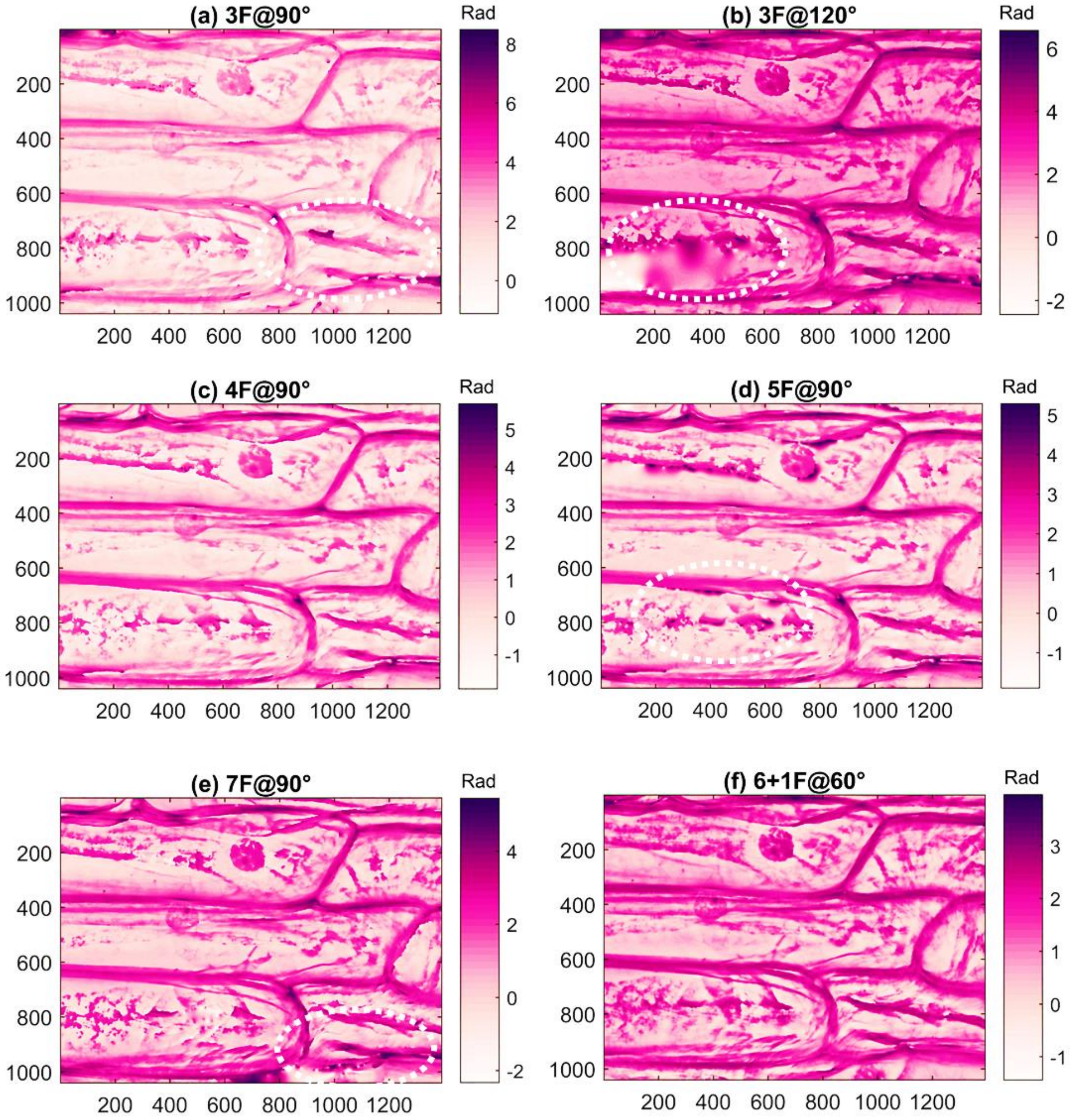

Figure 5.16 Phase maps of epidermis cells of Allium cepa reconstructed using various PSAs under green LED illumination, x and y axis represents pixel numbers in all images

The phase unwrapping problem can also be seen in the southwest area along the cell wall at row 1000 and column 0 to 200 Figure 5.16(c-e), where the phase maps are reconstructed using 4F@90°, 5F@90° and 7F@90° PSAs, compared to the southwest area in Figure 5.16(f). In

Figure 5.16(f), the phase map is reconstructed using 6+1F@60°. Errors in phase unwrapping from some parts of the cell are highlighted in white oval shapes in Figure 5.16a), d) and e). The phase unwrapping problem can also be seen in the southwest area (Figure 5.16c – e), where the phase maps are reconstructed using 4F@90°, 5F@90° and F@90° PSAs compared to the south-west area in Figure 5.16(f) where phase map was reconstructed using 6+1F@60° PSA. Interestingly, almost all the biological samples are transparent and hence, do not alter the light amplitude significantly but modulate the phase sufficiently to extract the information about structural organisation, density, index of refraction and thickness precisely. LQPIM system is capable of rendering quantitative cellular and sub-cellular structures from epidermis cells of *Allium cepa* (Figure 5.17).

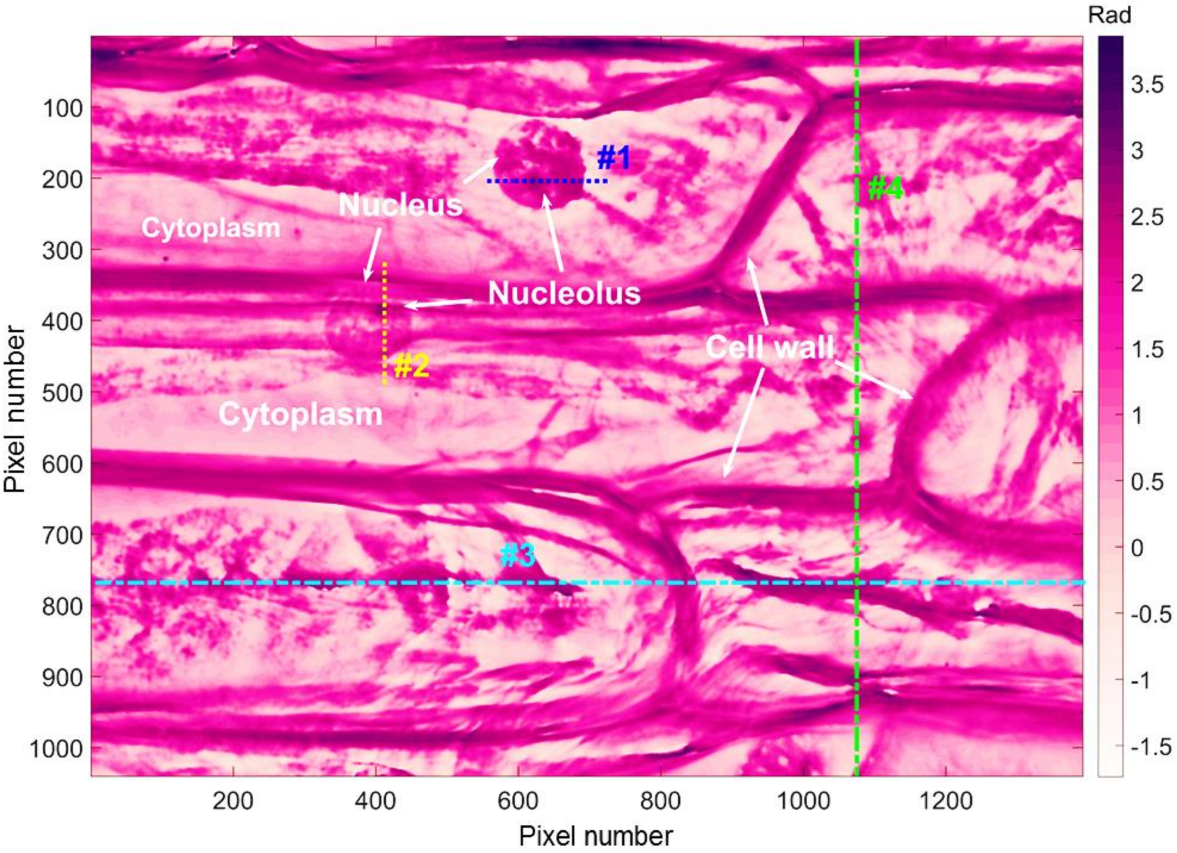

Figure 5.17 Phase map of epidermis cells of Allium cepa containing spatially fine structures using 6+1F@60° PSA. #1, #2, #3 and #4 area are presented in Figure 5.18 and Figure 5.19 for further analysis.

Phase variations induced by fine spatial objects are comparable with measured data available in the literature [139]–[141]. The #1 (Figure 5.18) and #2, #3 and #4 (Figure 5.19) areas mentioned in the phase image of *Allium cepa* (Figure 5.17) are used for the comparative assessment of phase measuring performance by 3F@120°, 4F@90° and 6+1F@60° PSAs. A better phase distribution of the nucleus was achieved using 6+1F@60° PSA compared to

3F@120° and 4F@90° PSAs. A phase change of 2.721 radians and 2.753 radians were measured for the nucleus and the nucleolus, respectively using 6+1F@60° PSA (Figure 5.18).

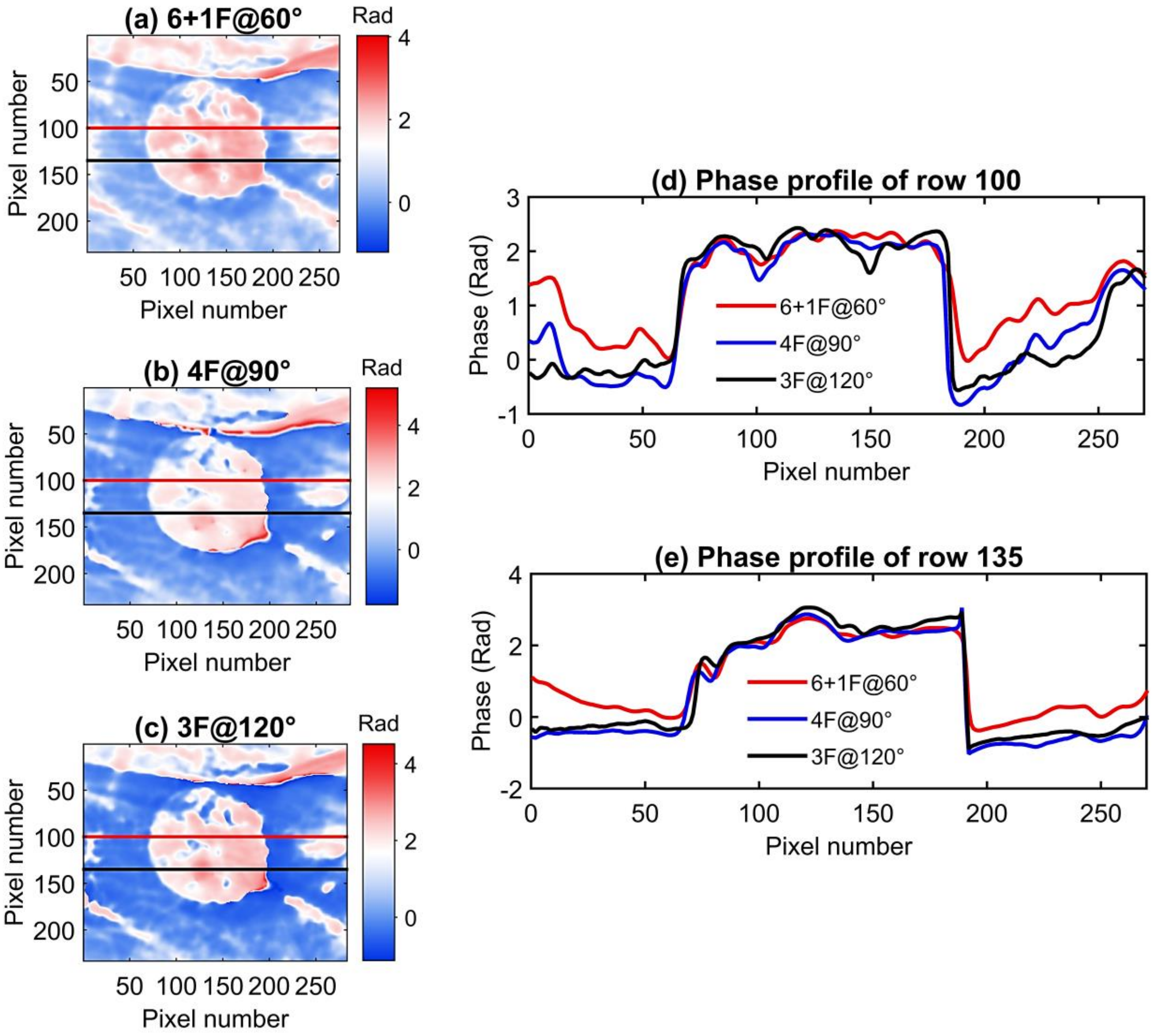

Figure 5.18 Cross-section phase profile of the nucleus (#1 area in Figure 5.17).

The phase distribution in #2, #3, and #4 area were measured using 3F@120°, 4F@90° and 6+1F@60° PSAs for the comparative analysis. In Figure 5.19 (phase profile of #3), both 3F@120° and 4F@90° PSAs have struggled to provide a continuous smooth phase distribution from 10 - 250 pixels due to larger discontinuities or false identified wrap over points, for example around pixel 350. The PSA 3F@120° has a large region between pixels 775 and 930 which shows an approximately 2π discontinuity compared to the other two data sets and is also clearly an unwrapping error. Other discontinuities and discrepancies in the unwrapped phase profiles in Figure 5.19 do not show the classical phase jumps of 2π. It is hypothesised that this can occur when an absolute phase change between pixels is less than the threshold of π required to identify a wrap-over point but the complexity of the object and proximity of other similar magnitude phase jumps, for example around the cell wall, combine to give inconsistencies of around π radians in the unwrapped phase between the PSAs. Furthermore, the phase distribution for 3F@120° PSA is consistently higher in Figure 5.19 due to an offset in the phase either from the PSA itself or from the starting point for phase unwrapping. Note that the data from PSAs have an offset due to algorithm design. It can be concluded from # area analysis that $6+1F@60^{\circ}$ PSA has performed well compared to other two PSAs at the best.

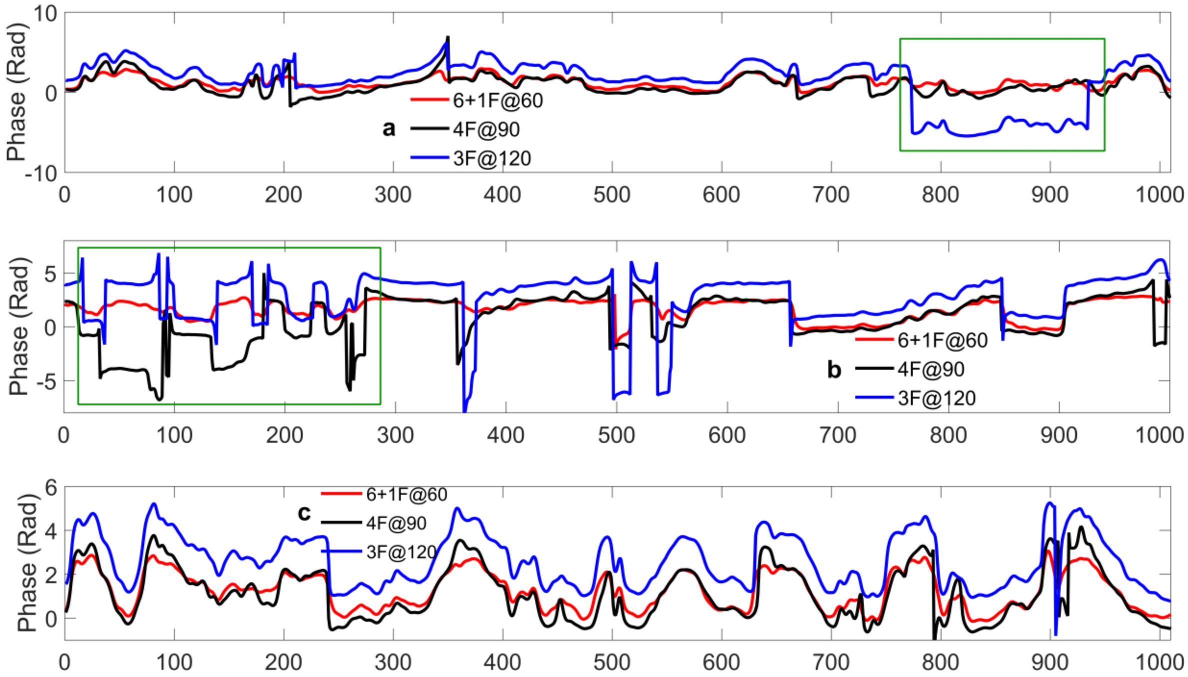

Figure 5.19 Cross-section profile of #2, #3 and #4 area outlined in Figure 5.17.

The phase change $[\Delta\varphi(x, y)]$ or thickness $[t(x, y)]$ variations from the cellular and sub-cellular organelles and structures were measured using Eq. (5.1). The refractive index values $(n = 1.36 - 1.39)$ for cytoplasm, $(n = 1.355 - 1.365)$ the nucleus, $(n = 1.375 - 1.385)$ for nucleolus of animal cells [74], [117] and $(n = 1.41 - 1.52)$ for the cell wall of flowering plants [141] were utlised for measuring spatially fine structures in epidermis cells of *Allium cepa* at sub-nanometre phase noise resolution (0.31 nm). An average phase change of 2.721 radians and 2.753 radians was persuaded by the nucleus and nucleolus, respectively (Figure 5.18 and Figure 5.20).

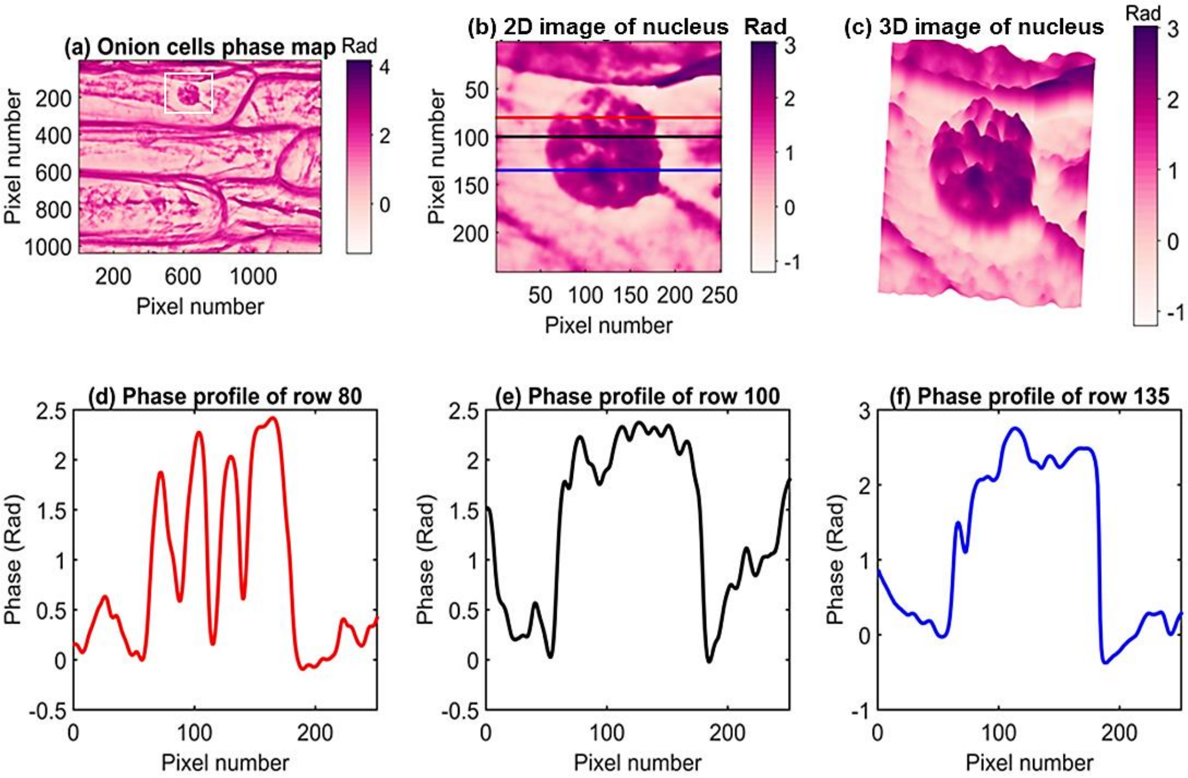

Figure 5.20 Quantitative phase map of epidermal cell of Allium cepa and a cross-section phase profile of the nucleus.

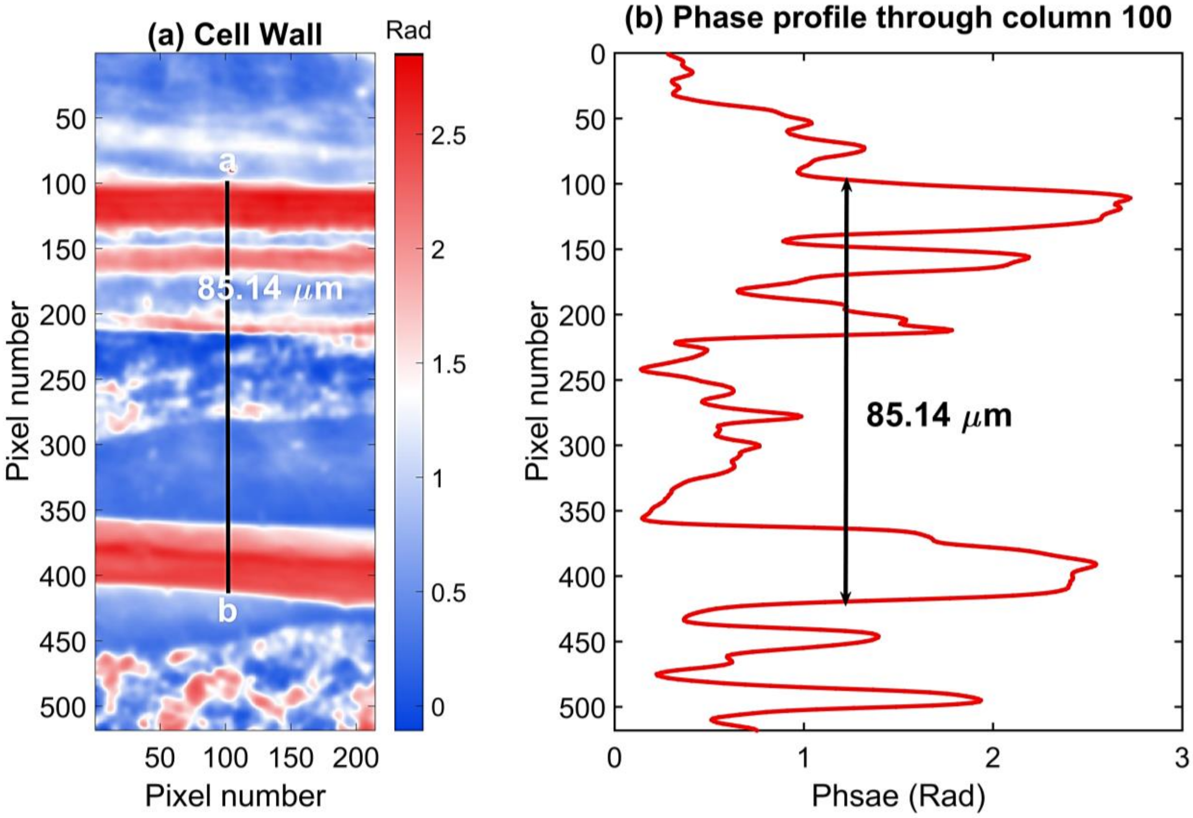

Figure 5.21Measured cell wall of Allium cepa.

The thickness 13.674 µm and a width 85.24 µm of the cell wall was also measured (Figure 5.21). The spatial nucleus diameter of 29.928 µm from *Allium cepa* was measured which is very close to 30 µm diameter nucleus reported for onion cells and plant cells [142]. Furthermore, there is a possibility of measured value being smaller than the actual size due to the squeezing of the objects in sample while preparing a sample slide for microscopic observation. The measurement of the thickness and phase values from the *Allium cepa* are acceptable in comparison with the available optically measured values in the literature [139], [143], [144] due to good transverse resolution of LQPIM system (assessed in Section 5.4).

5.6.3 Phase noise assessment under green laser illumination

A narrowband green laser illumination was also implemented in Kohler illumination mode to illuminate the sample to explore the dependency on coherent sources. The green laser (Elforlight G4 model, λ – 532 nm) was operated in a single longitudinal mode giving a coherence length of approximately 100 meters. The laser beam was projected onto a diffuser installed on a Maxon DC motor (Part Number: 256086, RE 10, Precious Metal Brushes, 0.75 Watt, 14000rpm, 2.4V) through an objective lens (10x, 0.25 - NA) to produce a prominent bright illumination spot on the diffuser. The motor speed was also controlled to give at least one complete revolution during the camera integration period. A high numerical aperture condenser lens (ACL12708U-A, NA - 0.78) was used to fill the receiving end of a multimode fibre (FG600AEA, NA - 0.22, 600 µm) and produce a focused bright spot on the output end (Figure 5.22).

The bright spot thus produced was further projected onto an annular ring sitting in the condenser of the microscope. The spatially filtered laser illumination from the annular ring is projected onto the sample via the high numerical aperture condenser lens (1.25 - NA) to illuminate the samples under LQPIM system. The speckles in laser illumination can be daunting in any microscopic investigation including phase measuring microscopy. In LQPIM optics, with laser illumination a diffuser was rotated at high speed (i.e. 13000rpm) in path of the incoming laser beam to average out the speckle noise. As a result, speckle-free laser illumination was produced. An effect of the rotating diffuser on averaging speckles can be seen in Figure 5.23b compared to the static diffuser (Figure 5.23a) in same illumination optical setup. Even in the case of a rotating diffuser, the unwrapped phase map obtained from the test chart shows the presence of parasitic fringes (from coherent reflections) running approximately horizontally through the centre of the field of view that are not present when using LEDs that have much lower coherence lengths (≤ 10 µm).

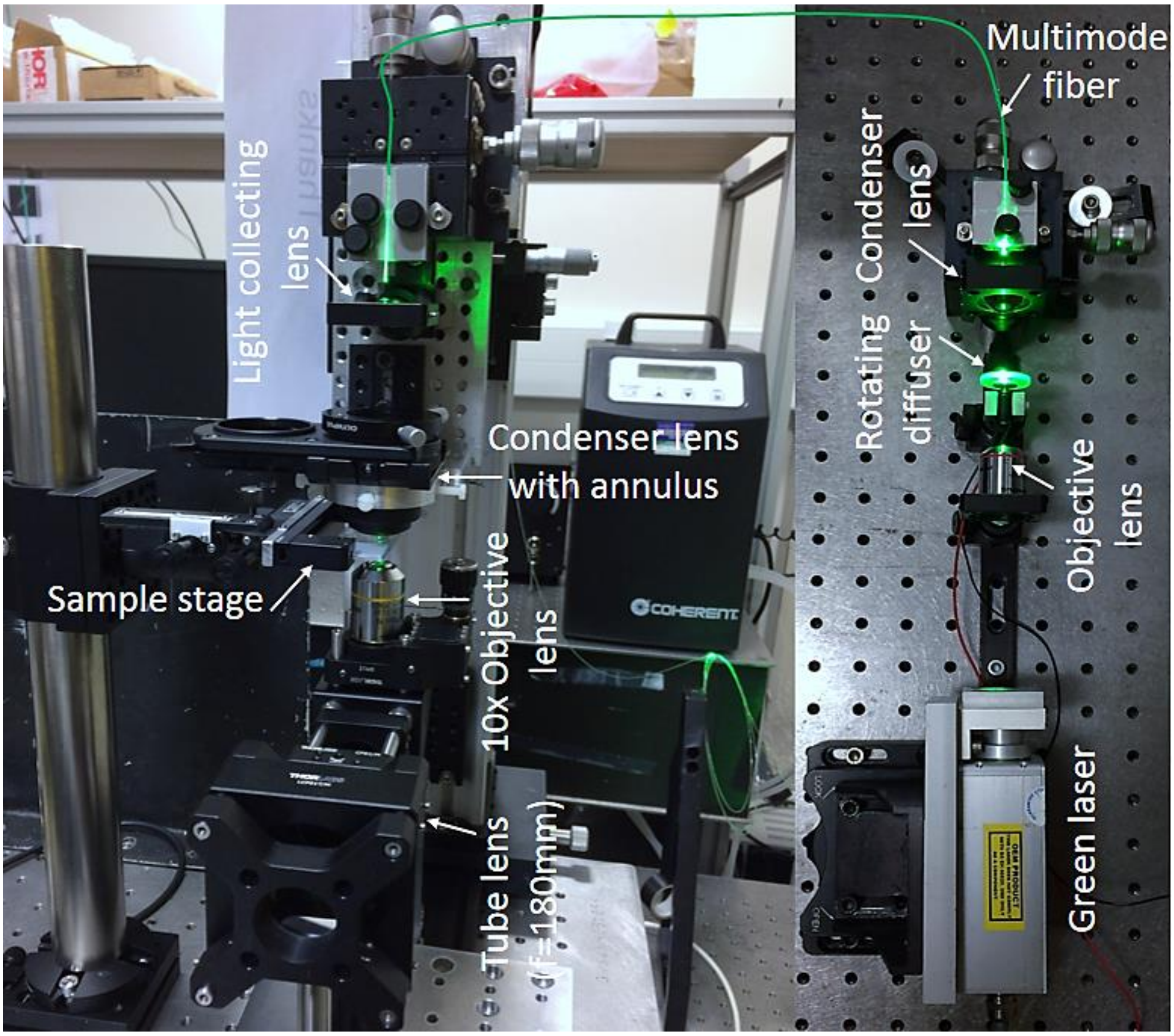

Figure 5.22 Representative laser illumination module implemented in LQPIM optics.

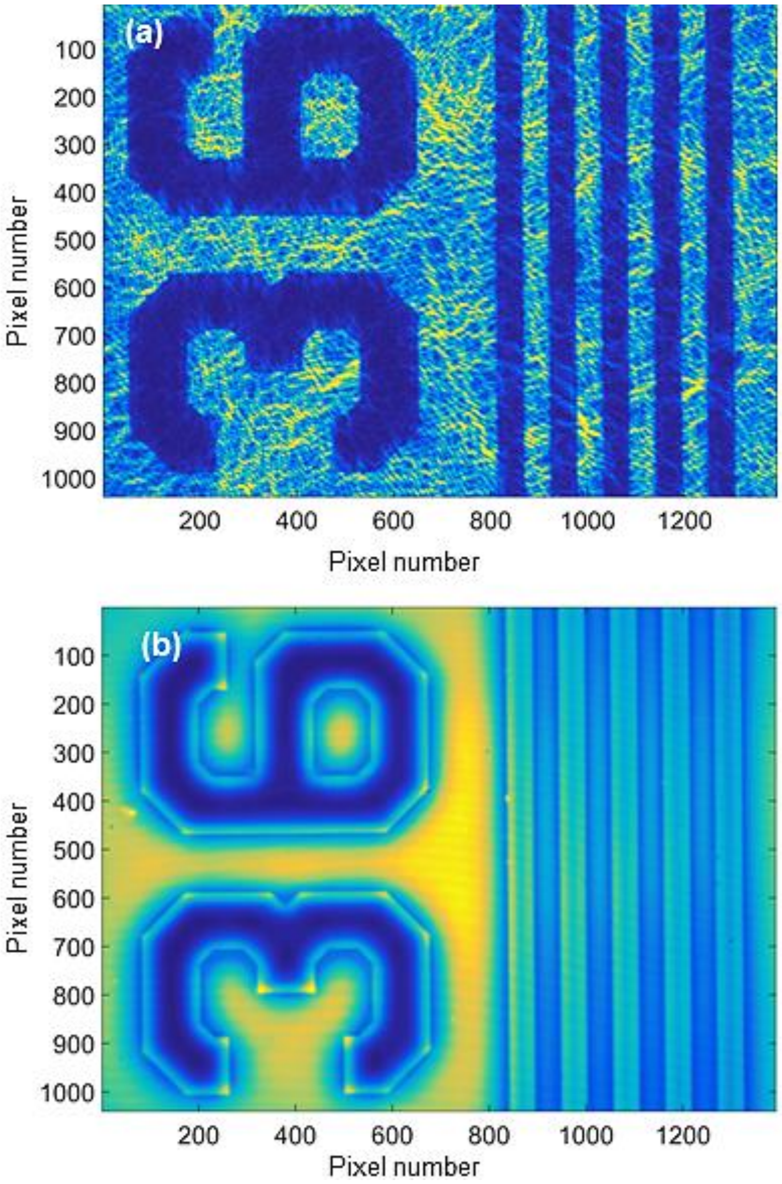

Figure 5.23 Effect of laser speckle noise in the image field of resolution test chart, (a) Static diffuser and (b) Rotating diffuser.

The exposure of 4.6 ms for laser illumination was controlled at the CCD camera using a neutral density filter (0.2 optical density) in the illumination part of the LQPIM system. The motor speed was also controlled to give at least one complete revolution to diffuse out the illumination beam from the diffuser and match with integration time at the CCD camera. The phase resolution capability of various PSAs in the presence of laser illumination was also evaluated. Their performance on phase measurement is summarised in Table 5.3. The phase noise of 0.512 nm (Figure 5.24) was measured for column 1077 using 6+1F@60° PSA and typically ≈ 2 times higher than 0.318 nm phase noise (achieved for the green illumination from LED, Figure 5.12). Furthermore, a reduced phase resolution of 1.520 nm and 1.581 nm for column 1235 corresponding to no marking stripe on the test chart was also persuaded by

4F@90° and 6+1F@60° PSAs, respectively (Figure 5.24). These values are larger than the corresponding values obtained under green LED illumination (Figure 5.12).

Table 5.3 Performance of PSAs in the presence of green laser illumination (λ – 532 nm).

PSI Algorithm(s) **Parameters**	**3F@90°**	**3F@120°**	**4F@90°**	**5F@90°**	**7F@90°**	**6+1F@60°**
Mean phase shift angle (α)	89°	118°	90°	90°	90°	61°
Std Dev in phase shift (σ)	± 2.23°	± 2.84°	± 2.88°	± 2.41°	± 2.88°	± 2.73°
Mean modulation of the image field (grayscale)	479	554	533	542	547	550
Minimum modulation over row 210 (grayscale)	12	13	14	15	13	16
Phase noise for column 1077 (σ_φ, fringe fraction)	1/ 594	1/940	1/764	1/821	1/892	1/909
Phase resolution for column 1077 (nm, λ - 532nm)	0.893	0.564	0.693	0.645	0.594	0.583

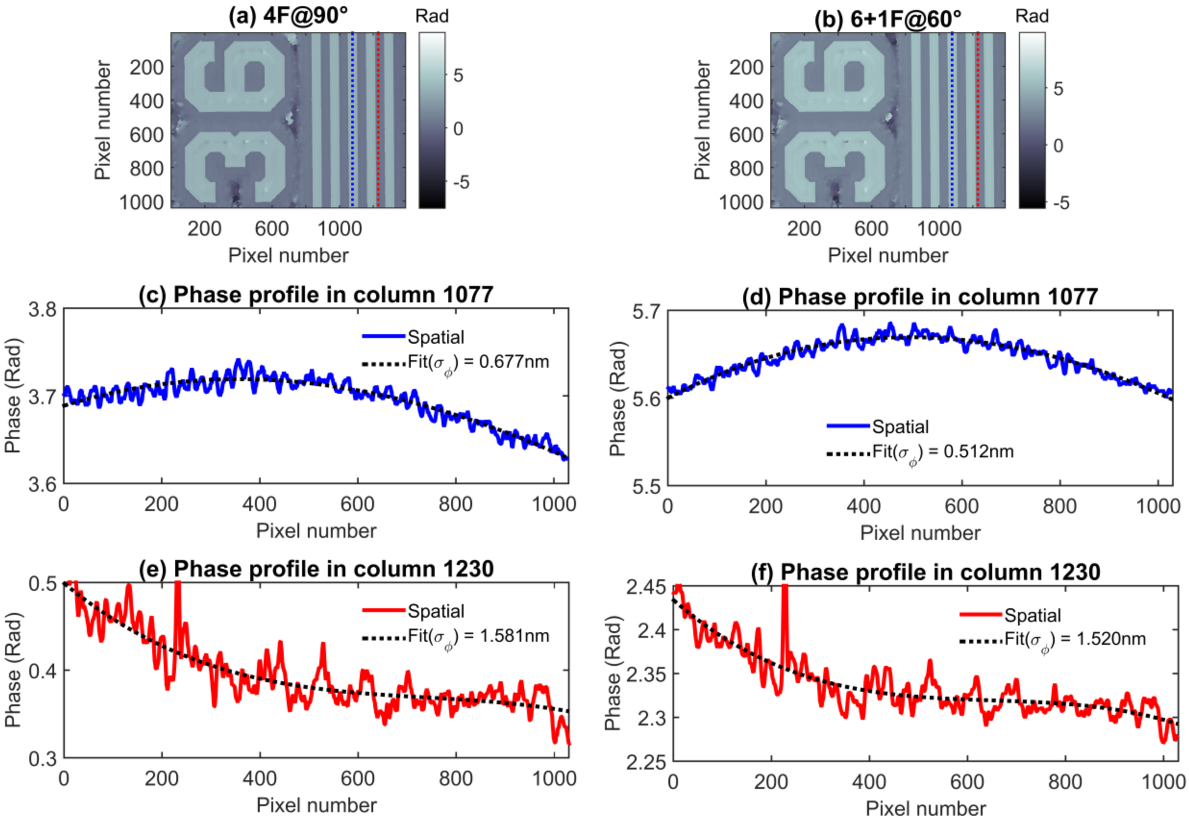

Figure 5.24 Phase assessment of NBS 1963A Test chart under green laser illumination.

The laser illumination in principle can provide a better resolution but the speckle noise and spurious fringes due to the long coherence length degrades the quality of an image and hence, phase resolution level was higher under green LED illumination. In contrast, broadband light has an advantage of short coherence length (approximately 8 µm, FWHM - 42 nm) that limits the opportunity for spurious fringes to produce an artefact in the interference image. In the case of laser illumination, the spot size (600 μm^2) illuminates the sample compared to a spot size of 1000 μm^2 in the case of green LED illumination. The laser beam have a limited field of view due to the narrow beam diameter hence, a noise problem can be seen around edges of the NBA 1963A test chart data (Figure 5.24 and Figure 5.26).

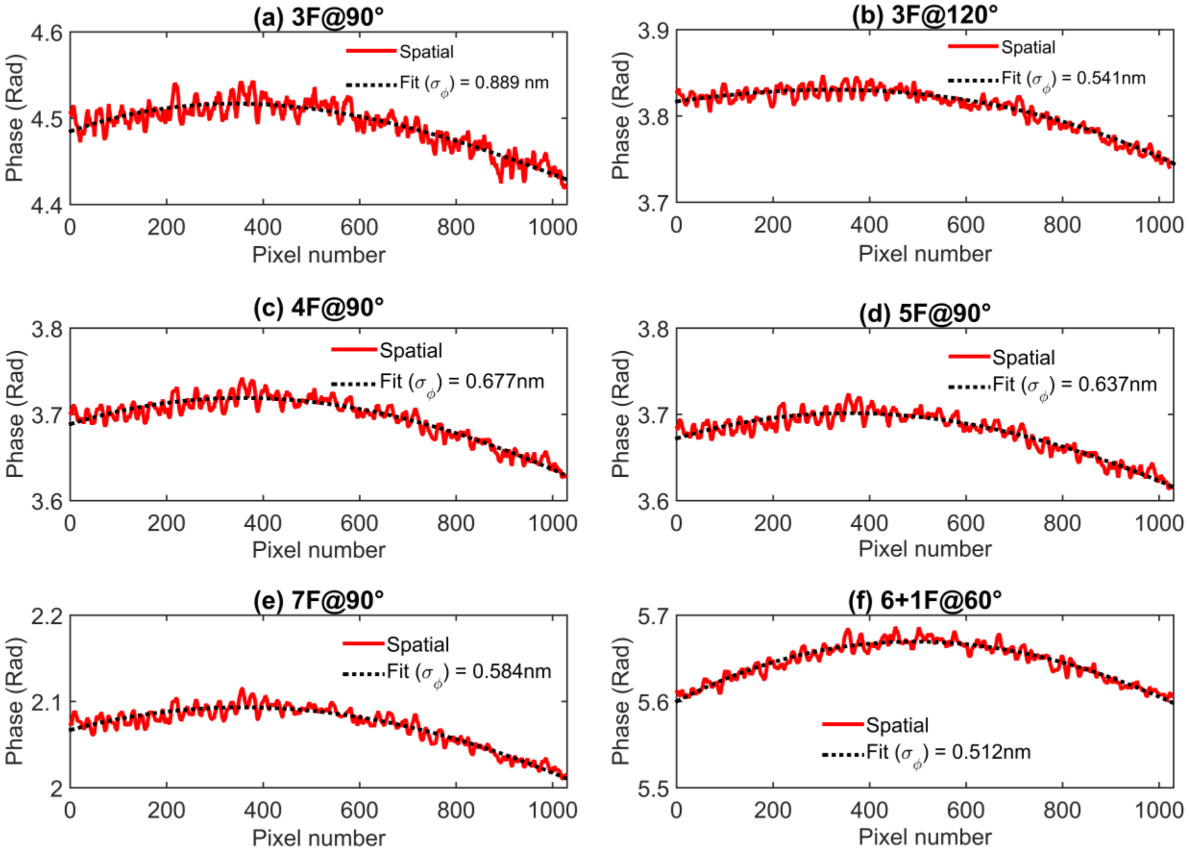

Figure 5.25 Phase resolution assessment in column 1077 under green laser illumination.

The rotating diffuser in the illumination optics renders an opportunity to produce a uniform scattered light field compared to green LED. Therefore, a better modulation depth in the full image field was apparent for all the measurements (Table 5.3). An assessment of the phase resolution competency of selected phase shift algorithms is presented in Table 5.3 and Figure 5.25. The reconstructed 2D phase map of the NBA1963A test chart under green laser illumination are presented in Figure 5.26 for the comparative assessment. The reconstruction of the phase map depends on utilised PSA, modulation depth between the scattered and non-scattered image fields and the accuracy of the phase step.

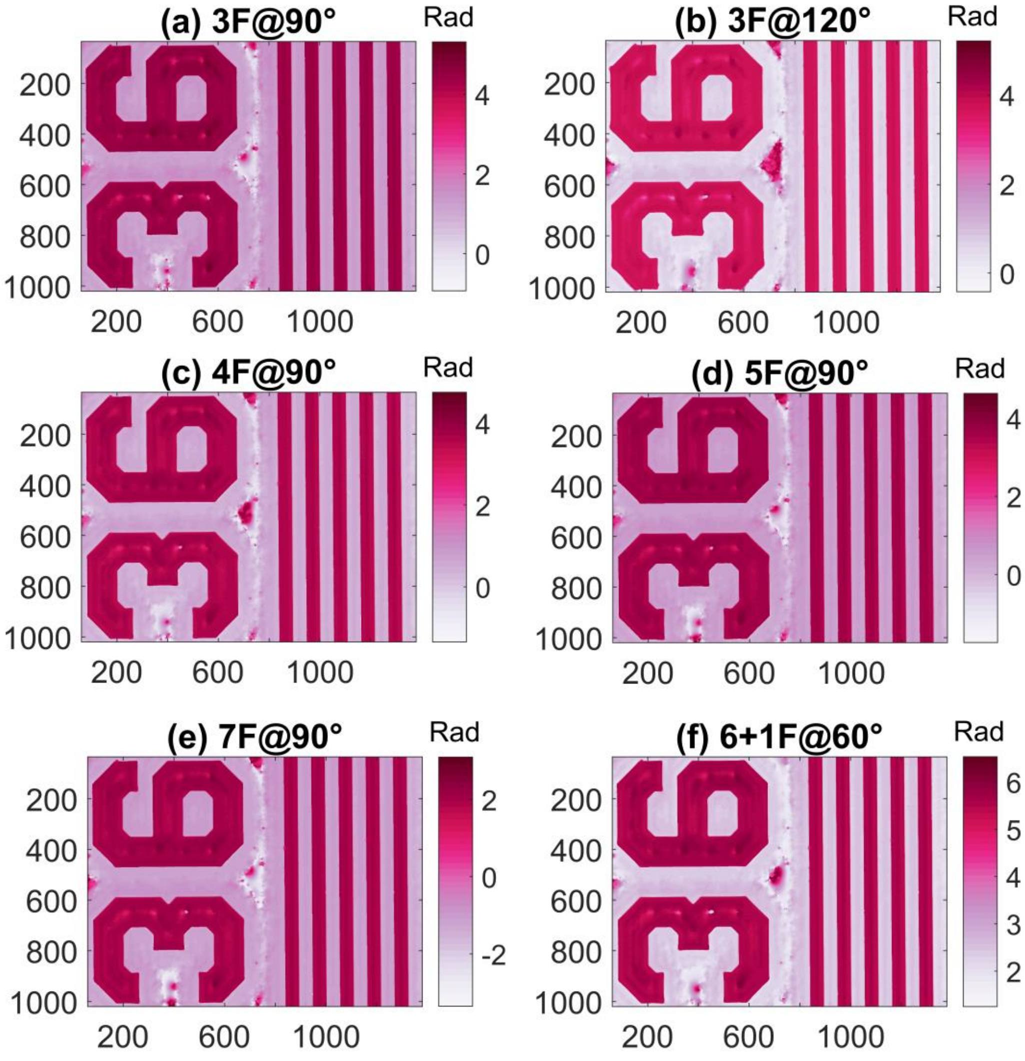

Figure 5.26 Reconstructed 2D phase maps of NBS 1963A Test chart under green laser illumination. x and y axis represents pixels numbers in all images.

5.6.4 Phase measurement from the biological samples using green illumination from a laser

The laser illuminated LQPIM system with a rotating diffuser was also evaluated by imaging biological sample, for example epidermis cells of *Allium cepa*. The unwrapped phase maps from each PSA are given in Figure 5.27 and a larger version of that obtained using the 6+1F@60° PSA is given in Figure 5.28, all obtained with laser illumination and the rotating diffuser. These data are from a different field of view compared to that with green LED illumination. Similar structures are seen in the laser illuminated data as were described previously. The nucleolus is particularly clear at row 850 of Figure 5.28, whereas that at approximately row 350 is less clear but still evident. These variations are dependent on the particular cells being examined. Structures at the top of the cell at row 150-350, column 200-1200 are also evident (but to a lesser extent) in the data from Figure 5.17 with LED illumination at row 150-300 and columns 1050-1300. These rows and column values belongs to the semi-permeable thin membrane, cytosolic fluid and high refractive index organelle mitochondria (1.48) [115].

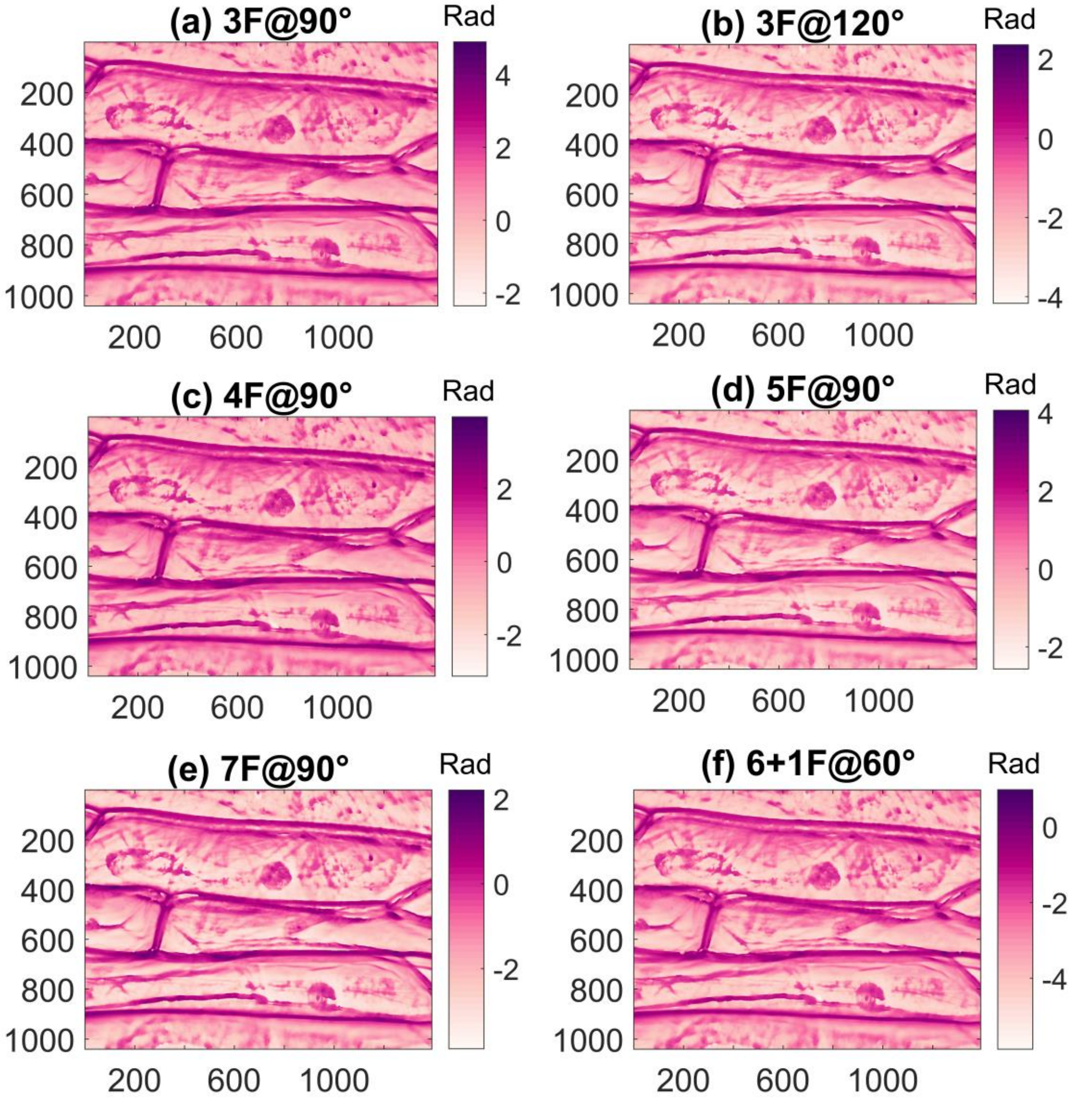

Figure 5.27 2D reconstructed phase maps of onion cells under green laser illumination, x and y axis represents pixel numbers for all images.

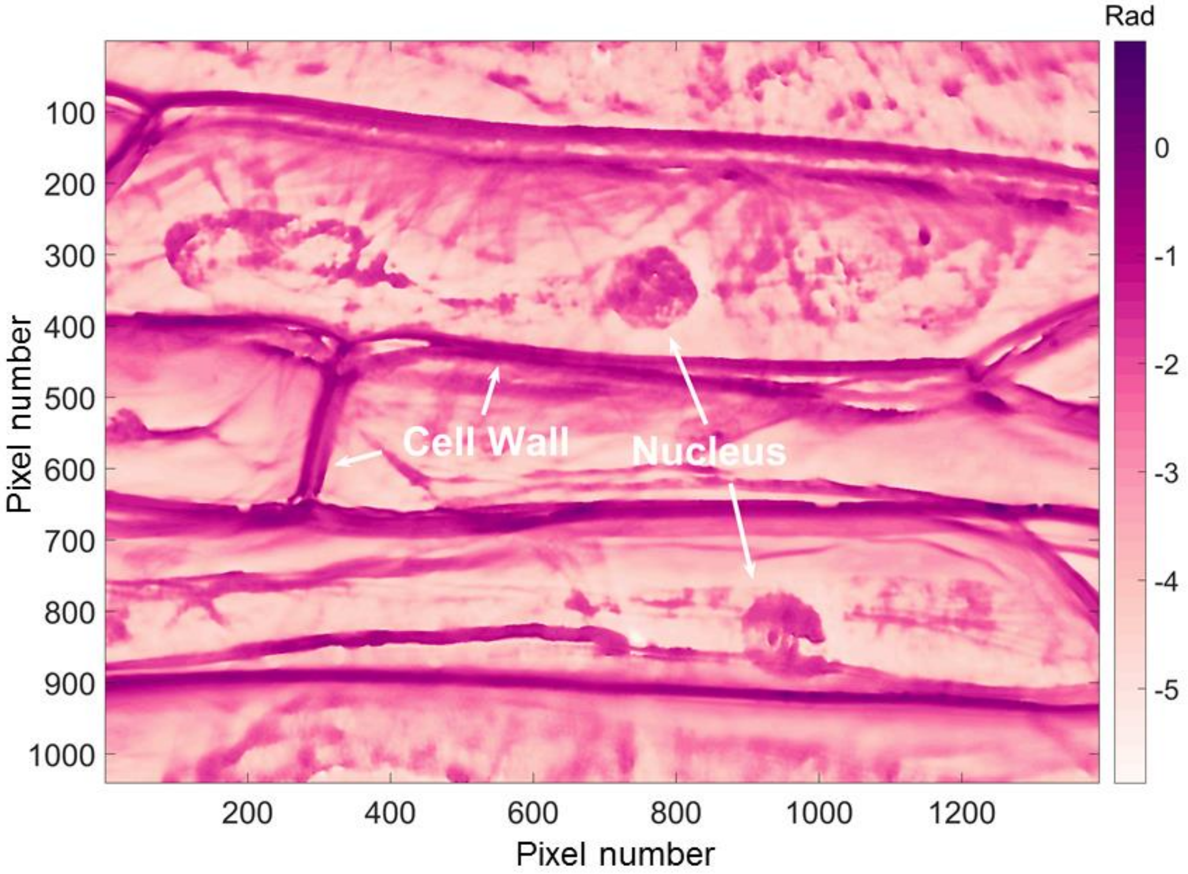

Figure 5.28 Phase map of epidermis cells of Allium cepa under green laser illumination

5.7 Summary

The proposed LQPIM system was evaluated by measuring the phase noise levels from a NBA 1963A resolution test chart. Furthermore, it was also used to extract phase profiles of the fine spatial strures at nanometre scale from the optically thin and thick samples. This method successfully renders the phase maps of NBA 1963A test chart, thick glass beads and epidermis cells of *Allium cepa.* It also provides similar functionality and accuracy in phase measurement that appears in the SLM based microscopy methods but at a significantly lower cost for the instrumentation. In Section 5.2, the optimisation of laser-cut apertures for reshaping and spatially filtering the scattered and non-scattered image fields was presented. The precise size of LCAs removes the cross-talk between the scattered and non-scattered image light fields in some instances at the Fourier plane and directs both two-beams to form a high contrast interference image at the CCD camera. A sequential assessment of different sizes of LCAs implemented on mirrors M_2 and M_3 in Michelson interferometer optics was done showing significant performance benefits. Further, the parameters such as mean modulation depth, mean phase shift angle (α) and the visibility ratio (γ) were evaluated from the captured temporal phase shifted images of the NBA 1963A Test chart. A uniform area on the test chart, for example column 1077 and 1230 corresponding to black strip (chrome coating) and without strips (glass slide itself) were selected for the assessment of phase noise. Section 5.6, presents the effect of different illumination sources, for example, a green LED or a green laser on reconstruction of phase maps of the NBA 1963A test chart as well as epidermis cells of *Allium cepa*. A phase resolution of 0.318 µm was achieved under green LED illumination compared to a phase resolution of 0.583 µm under green laser illumination.

The phase resolution using a laser illumination source may be affected due to speckle noise, mechanical vibrations and spurious interference fringes in the image, the latter being observed in the images when a high speed rotating diffuser was used. The ability of both the green LED and laser illuminated LQPIM system to quantify biological structures in static cells was also demonstrated. In particular, the use of incoherent illumination has provided highest quality images, these enabling measurements of the cellular structure and sub-cellular organelles at nanometre scale. The physical artefacts, glass bead sample, were utilised to introduce a known long OPD, where the OPD is larger than that hitherto reported to the best of the author’s knowledge. Measurements in excess of 1400 nm OPD have been presented.

Chapter 6. CONCLUSIONS AND FUTURE WORK

In this thesis, a flexible low-cost quantitative phase imaging microscope has been developed for imaging fixed cells and the dynamics of label-free biological cells. Both LQPIM optics based on twin-machined concentric mirrors or LCAs utilises standard optical components in practice. The cost of phase shifting module is <10% of that using an SLM in QPI microscopy methods or wire grid polariser based camera in case of dynamic phase microscope. This study includes an assessment of the relationship between the wavelength, bandwidth and coherence properties of the illumination source and PSAs to render an optimal solution for imaging phase objects from the biological origin. The following conclusions are drawn from the research work presented in this thesis.

6.1 An optimal solution for imaging label-free phase objects

The mathematical simulations based on two-beam interference equation model efficiently implemented in MATLAB. It has been shown that a specific wavelength and bandwidth of illumination source and a suitable PSA provides a minimum error free space to image the phase distribution of label-free objects. The simulation model also confirms that an accurate phase distribution can be obtained from large OPDs that correspond to thick optical samples. In such large OPD calculations, PSAs with a higher number of frames tend to be useful (e.g. 6+1F@60° PSA) compared to lower frame number PSAs (e.g. 3F@90° PSA) due to an advantage of averaging out systematic noise from the measurements. The results show variable performance and critical levels of source bandwidth beyond which the OPD calculation errors rise steeply due to significant reductions in fringe modulation (Chapter 3, Section 3.5). Almost all the PSAs evaluated were failed to quantify phase accurately from the large OPD (e.g. ≥ 1300 nm) at higher bandwidths (≥ 90 nm) with a central wavelength of 520nm. In general, it has been found that 4F@90° and 6+1F@60° PSA offers the best compromise for optically thin and thick samples, respectively. The simulation experiments show that the phase resolution achievable is not significantly altered for source bandwidths in the range of 30 - 90 nm. Therefore, measurements over longer OPDs – relevant to more complex cells and multi-cell layer samples – are best achieved using narrower band LED sources with bandwidths in the range 30 - 60 nm, contrary to the wide spread use of white light sources in current quantitative phase imaging microscopes. Incoherent LED sources offer performance benefits in terms of noise and parasitic fringes compared to the use of lasers with rotating diffusers for speckle averaging. It can be conjectured that measurements over even longer OPDs are best achieved by band-pass filtering an LED source.

6.2 A flexible LQPIM system for phase imaging

A flexible LQPIM optical system is developed (detailed information can be found in Chapter 4) with phase shifting modules in the back focal plane that offer similar functionality compared to designs that employ a phase only spatial light modulator. The developed LQPIM optics are much cheaper by utilising standard optical components. The first LQPIM optical system utilises twin concentric mirrors in the PSM (requiring one custom optical component) while the second utilises LCAs in the arms of an interferometer (requiring only standard optical components and low cost laser cut apertures). Most importantly, both PSMs are capable of inducing pre-defined or as per required by the user phase modulations between the scattered and non-scattered image field in the LQPIM system. The phase imaging from both the QPIM optics is concluded as follows;

- ❖ In practice, most commercial condensers position the illumination annulus at an intermediate numerical aperture of the objective lens in the microscopy system. The NA and the lateral resolution of LQPIM based on the custom twin concentric mirrors is limited by the design. Technically, the gap between the twin mirrors loses some full field information and hence, the scattered field beyond the NA of the illuminating annulus was lost, therefore, the lateral resolution. However, this optical system can be optimised for phase imaging as discussed in future work (Section 6.4).

- The alternative design was achieved without custom mirror optics by employing low-cost LCAs in PSM. The use of LCAs in the arms of Michelson interferometer efficiently separates and reshapes the scattered and non-scattered optical image fields and hence, produces a high contrast interference image at the CCD camera. In both cases, a PZT driven high precision linear stage holding a reference mirror was used for phase shifting by supplying appropriate voltages using an analogue output card (NI-USB6008).

6.3 Phase imaging from label-free biological samples

The biological cellular and sub-cellular structural organisation is very complex, ranging from monolayer cell culture to multilayer cell cultures. It comprises from thin (e.g. semi permeable cell membrane) to thick (e.g. Golgi complex) cellular structures with spatially varying refractive index properties. Such spatial variations in the thickness and index of refraction provides non-linear intensity distribution with optical phase change in the image field. The LQPIM system based on LCAs efficiently captured all intensity variations from edges of the cells and cellular structures. The phase distribution were quantified using a suitable PSA and narrowband green LED illumination. The method render phase maps from the spatially fine biological structures at resolution. For example, the phase maps of the cell wall, thin plasma membrane, the nucleus and the nucleolus were reconstructed and resolved efficiently.

The method is also capable of rendering phase distributions from optically thick samples. For example, phase distribution from 10 - 30 µm diameter glass beads were measured effectively. The OPD of approximately ≥ 1300 nm has been successfully measured in the experiments and the uncertainties obtained are in agreement with a theoretical analysis at approximately 2%.

6.4 Future work

In future, the proposed LQPIM system optics will be improved to enable live cell imaging experiments in a long-term manner (i.e. hours to days). In the PSM, the replacement of kinematic mirror mounts with piezoelectric adjusters can give easier and more accurate superposition of the scattered and non-scattered image light fields. This will create an opportunity to minimise cross talk from spurious diffraction other than from the phase plate and annulus masks. The improved superposition will also help to achieve good modulation depth among consecutive phase shifted interference images. Hence, altogether it would help to resolve steep phase gradients around the edges of objects, a general problem in phase microscopy. Furthermore, a small working distance condenser lens used in this thesis will be replaced with a long working distance optic to ease observations of live cells under petri plates. This implementation will also give an opportunity to introduce live cell incubation chambers to image their dynamics naturally. Therefore, live cell dynamics can be studied and will provide a scope to monitor the cells under a microscope without special preparation.

A further implementation may be done to achieve a common path optics using a PZT actuated circular mirror and a fixed annular mirror. The implementation of twin-machined concentric circulars mirrors to form a common path LQPIM optical system outlined in Section 4.5.2 has limited NA and hence, the lateral resolution. However, silicon technology can be used to fabricate the mirror pair using photolithography and a dry etching process. Optically flat reflective surfaces can be produced precisely by depositing a thin silver coating over the surface that can modulate the scattered and non-scattered image light fields from the phase plate and annular rings, respectively from the microscope. A gap between the two surfaces (few microns ≤ 25 µm) could minimise the loss of the light field while preventing the friction between the two surfaces. The annular in the condenser lens would also need to be modified to position the non-scattered field towards edge of the available NA from the objective lens. The side and front view of the piezo actuator based mirror module is presented in Figure 6.1.

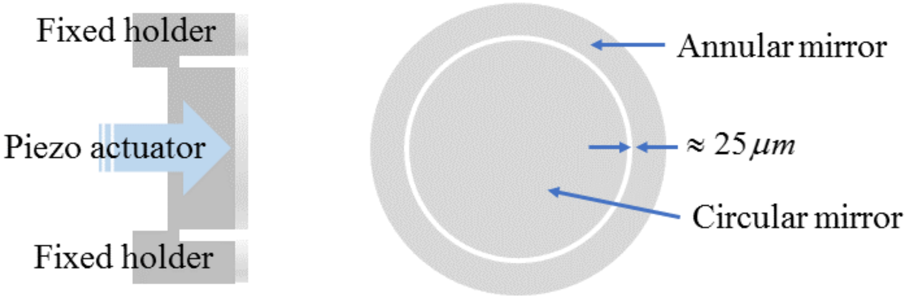

Figure 6.1 Piezo actuator based mirror module, left - side view and right - front view.

The Fourier fields of the scattered and non-scattered light can be controlled using the relay lenses in the optics of the LQPIM system. The relay lenses will fit the scattered and non-scattered light onto the mirror pair as shown in Figure 6.1 giving a common path optical system overall. This will further reduce instability due to vibrations and environmental perturbations.

APPENDIX

A.1 MATLAB code for the assessment of PSAs, bandwidth and wavelength of illumination source

```
clear all
clear global
close all;

mxopd = 2000;                % Optical path difference in nanometres
nopd = 4000;
opd = linspace(0, mxopd, nopd);

% Type of light source
ls = input('Input the light source type, 0 - laser, 1 - green LED, 2 -
white LED, 3 - uniform broadband : ');
% Type of simulation
sim = input('Input the simulation type, 0 - vs OPD, 1 - vs source centre
and BW : ');
% Do we want to see intermediate plots
iplot = input('Input 1 to see intermediate plots, 0 otherwise : ');

if sim==0,
    % Depending on the input, define the light source characteristics
    if ls==0,           % laser
        centrew = input('Input the laser wavelength (nm) : ');
        fwhm = 0;               % These 3 definitions are needed to avoid
an undefined variable error in calling the function to setup the source
spectrum
        leftw = centrew;
        rightw = centrew;

    elseif ls==3,           % uniform broadband
        centrew = input('Input the centre wavelength (nm) : ');
        fwhm = input('Input the FWHM of the uniform broadband source (nm)
: ');
        leftw = centrew - fwhm/2;
        rightw = centrew + fwhm/2;
    else
        centrew = 0;            % These 4 definitions are needed to avoid
an undefined variable error in calling the function to setup the source
spectrum
        fwhm = 0;
        leftw = 0;
        rightw = 0;
    end;
end;

% Read in the basic LED spectra to be used
% Green
green_led = xlsread('M530L3_data.xlsx');
wgled = green_led(:,1);                     % Normalised intensity data
igled = green_led(:,2);
mxigled = max(igled);
nw = length(wgled);
```

```
% Find statistics for this LED
gmoment = 0;
gipeak = 0;
for i=1:length(wgled),
    gmoment = gmoment + igled(i)*wgled(i);
    if igled(i)>gipeak,
        gipeak = igled(i);
        gwpeak = wgled(i);
    end;
end;
gledcw = gmoment / sum(igled);

% Now find the FWHM data
idx = find(igled>(gipeak/2));
gledfwhmleft = wgled(min(idx));
gledfwhmright = wgled(max(idx));
gledfwhm = wgled(max(idx)) - wgled(min(idx));
if iplot==1,
    figure
    plot( wgled, igled, 'k-', 'LineWidth', 2);
    v=axis;
    axis([200 1000 0 v(4)]);
    v=axis;
    hold on;
    plot( [gledcw gledcw], [0 v(4)], 'g-.', 'LineWidth', 2);
    plot( [gwpeak gwpeak], [0 v(4)], 'g-', 'LineWidth', 2);
    plot( [gledfwhmleft gledfwhmleft], [0 v(4)/2], 'g:', 'LineWidth', 2);
    plot( [gledfwhmright gledfwhmright], [0 v(4)/2], 'g:', 'LineWidth',
2);
    s = sprintf('Green LED, Thorlabs M530L3, Centroid wavelength %.1f nm,
Peak wavelength %.1f nm, FWHM %.1f nm', gledcw, gwpeak, gledfwhm);
    title(s, 'FontSize', 16);
    set(gca, 'FontSize', 14);
    grid on;
end;

% Read in the basic LED spectra to be used
% White
white_led = xlsread('MWWHL4_data.xlsx');
wwled = white_led(:,1);                     % Normalised intensity data
iwled = white_led(:,2);
mxiwled = max(iwled);
nw = length(wwled);

% Find statistics for this LED
wmoment = 0;
wipeak = 0;
for i=1:length(wwled),
    wmoment = wmoment + iwled(i)*wwled(i);
    if iwled(i)>wipeak,
        wipeak = iwled(i);
        wwpeak = wwled(i);
    end;
end;
wledcw = wmoment / sum(iwled);

% Now find the FWHM data
idx = find(iwled>(wipeak/2));
wledfwhmleft = wwled(min(idx));
wledfwhmright = wwled(max(idx));
wledfwhm = wwled(max(idx)) - wwled(min(idx));
if iplot==1,
```

```
    figure
    plot( wwled, iwled, 'k-', 'LineWidth', 2);
    v=axis;
    axis([200 1000 0 v(4)]);
    v=axis;
    hold on;
    plot( [wledcw wledcw], [0 v(4)], 'k-.', 'LineWidth', 2);
    plot( [wwpeak wwpeak], [0 v(4)], 'k-', 'LineWidth', 2);
    plot( [wledfwhmleft wledfwhmleft], [0 v(4)/2], 'k:', 'LineWidth', 2);
    plot( [wledfwhmright wledfwhmright], [0 v(4)/2], 'k:', 'LineWidth',
2);
    s = sprintf('White LED, Thorlabs MWWHL4, Centroid wavelength %.1f nm,
Peak wavelength %.1f nm, FWHM %.1f nm', wledcw, wwpeak, wledfwhm);
    title(s, 'FontSize', 16);
    set(gca, 'FontSize', 14);
    grid on;
end;

if sim==0,           % Doing a simulation against OPD
    % We need a single source spectrum as per the possible definitions
    % above
    wsource = 200:0.2:1000;          % Define the wavelength axis from 200
nm to 1000 nm in 0.2 nm steps, the step size directly reflects the
resolution of the spectra from Thorlabs
    newcentrew = 0;                  % For this simulation we do not wish
to shift the spectrum so set this to 0
    isource = DefineLightSourceSpectrum( ls, newcentrew, wsource, centrew,
fwhm, leftw, rightw, wgled, igled, gledcw, wwled, iwled, wledcw);
    % Find centre of final spectrum
    imom = 0;
    for i=1:length(wsource),
        imom = imom + isource(i)*wsource(i);
    end;
    sourcecw = imom/sum(isource);
    % Optional plot of the source spectrum
    if iplot==1,
        figure
        plot( wsource, isource, 'k-', 'LineWidth', 2);
        set(gca, 'FontSize', 14);
        grid on;
        title(sprintf('Source Spectrum for Simulation, Calculated Centre
Wavelength %.2f nm', sourcecw), 'FontSize', 16);
    end;

    % Now we have the source spectrum in a common format in wsource,
    % isource.  Carry out simulation

    %%%%%%%%%%%%%%%%%%%%%%%%%%%%%%%%% This line is dependent on the phase
    %%%%%%%%%%%%%%%%%%%%%%%%%%%%%%%%% step algorithm
    % Note the most accurate value for the source centre wavelength will
    % come from the centre of mass calculation above, hence base the steps
    % on this
    opdstep = [0 sourcecw/4 sourcecw/2 sourcecw*3/4];         % Define the
phase steps that we will be using, nm

    inten = zeros(nopd, length(opdstep));
% To store the phase stepped intensities as a function of OPD and phase
step
% 2 beam interference intensity equation: I = Idc + Im * cos(2pi x/w)

% Assume perfect interference for now
    idc = 1;
```

```
    im = 1;
    % Loop and sum intensities for each OPD and each wavelength
    for iiopd = 1:nopd,
        for iiw = 1:length(wsource),
            for kk = 1:length(opdstep);
                ph = 2*pi*(opd(iiopd)+opdstep(kk))/wsource(iiw);
                inten( iiopd, kk) = inten( iiopd, kk) + isource(iiw)*(idc
+ im*cos(ph));        % Now modifies each intensity by the intensity at
that wavelength from the LED spectrum
            end;
        end;
    end;
    inten = inten./sum(isource);

    % Check by plotting phase stepped intensities before re-scaling or
    % adding noise
    if iplot==1,
        figure
        plot( opd, inten(:,1), 'k-', 'LineWidth', 2);
        xlabel('OPD (nm)');
        ylabel('Interference Intensity (arb.)');
        hold on;
        plot( opd, inten(:,2), 'k:', 'LineWidth', 2);
    end;
    % Modify intensities to new IDC and IM
    newidc = 1350;                          % Based on experimental
measurements
    newim = 475;
    inten = ((inten-idc)./im*newim) + newidc;

    % Add multiplicative noise
    global AMNpn AMNnframes
    AMNpn = 2.5;
    AMNnframes = 1;                         % Change this value to >1 for
frame averaging (integer)
    inten = TTAddMultNoise(inten, 0, 0);

    % Calculate the wrapped phase
    % This line is dependent on the phase step algorithm
    global Wlm
    Wlm = 0;
    global WFFANlm
    WFFANlm = 0;
    [wrph moddepth] = TTWrappedFFAN(inten, 0, 0);

    % Generate the expected phase function at the mid-point of the
wavelength range
    meanph = 2*pi*opd/(sourcecw);

    % And hence get the phase error by taking the difference of the
unwrapped phase from phase stepping and the expected phase
    pherr = unwrap(wrph)-meanph';

    % Calculate errors in terms of optical path difference at the mean
wavelength (in nm)
    opderr = pherr/(2*pi)*(sourcecw);
    stdopderr = std( opderr);

    % Determine error up to a certain OPD (250 nm)
    %clear relerr
    opdthreshold_250 = 250;
    idx = find(opd>=opdthreshold_250, 1, 'first');
```

```
    meansysabserr250 = mean(abs(opderr(1:idx)));
    maxsysabserr250 = max(abs(opderr(1:idx)));
    relerr = opderr(1:idx) - mean(opderr(1:idx));
    maxsysrelerr250 = max(abs(relerr));

    % Determine error up to a certain OPD (250 nm)
    s = sprintf('Centre %.1f nm, Max OPD Error is %.3f nm and Mean OPD
Error is %.3f nm up to an OPD of %.1f nm', sourcecw, maxsysabserr250,
meansysabserr250, opdthreshold_250);
    disp(s);

    % Determine error up to a certain OPD (1250 nm)
    %clear relerr
    opdthreshold_1250 = 1250;
    idx = find(opd>=opdthreshold_1250, 1, 'first');
    meansysabserr1250 = mean(abs(opderr(1:idx)));
    maxsysabserr1250 = max(abs(opderr(1:idx)));
    relerr = opderr(1:idx) - mean(opderr(1:idx));
    maxsysrelerr1250 = max(abs(relerr));

    % Determine error up to a certain OPD (1250 nm)
    s = sprintf('Centre %.1f nm, Max OPD Error is %.3f nm and Mean OPD
Error is %.3f nm up to an OPD of %.1f nm', sourcecw, maxsysabserr1250,
meansysabserr1250, opdthreshold_1250);
    disp(s);

    % Generate a plot to show output
    figure
    subplot(311);
    plot( opd, inten(:,1), 'k-', 'LineWidth', 2);
    ylabel('Interference Intensity (gray)');
    set(gca, 'FontSize', 14);
    v=axis;
    axis([v(1) v(2) 0 v(4)]);
    subplot(312);
    plot( opd, unwrap(wrph), 'k-', 'LineWidth', 2);
    hold on;
    plot( opd, meanph', 'k:', 'LineWidth', 2);
    ylabel('Unwrapped phase (radians)');
    legend('Calculated Phase','Theoretical Phase');
    set(gca, 'FontSize', 14);
    subplot(313);
    plot( opd, opderr, 'k-', 'LineWidth', 2);
    ylabel('Phase error (nm)');
    set(gca, 'FontSize', 14);
    xlabel('Optical Path Difference (nm)');
    title(sprintf('Standard Deviation Phase Uncertainty %.3f nm',
stdopderr),'FontSize', 16);

elseif sim==1,              % Simulation against source centre wavelength
and bandwidth
    % Actual simulation depends on the light source selected
    % For the LED sources, only the centre wavelength can be reasonably
adjusted
    % Similarly, for a laser source
    % Only for a uniform broadband source does it make sense to adjust
both the bandwidth and the centre wavelength

    % Setup the simulation, all light sources need the centre wavelength
adjusting
    centrelow = input('Input the lowest centre wavelength to use (nm) :
');
```

```
    centrehigh = input('Input the highest centre wavelength to use (nm) :
');
    ncentre = input('Input the number of centre wavelengths to simulate :
');
    centreset = linspace( centrelow, centrehigh, ncentre);
    if ls==3,        % broadband source so get low high and number of
bandwidths to use
        fwhmlow = input('Input the lowest bandwidth to use (nm)  : ');
        fwhmhigh = input('Input the highest bandwidth to use (nm)  : ');
        nfwhm = input('Input the number of bandwidths to simulate : ');
        fwhmset = linspace( fwhmlow, fwhmhigh, nfwhm);
    else
        nfwhm = 1;
        if ls==0,
            fwhmset = [0];
        elseif ls==1,
            fwhmset = [gledfwhm];
        elseif ls==2,
            fwhmset = [wledfwhm];
        end;
    end;

    % Initialise output variables
    meansysabserr250 = zeros(length(centreset), length(fwhmset));
    maxsysabserr250 = zeros(length(centreset), length(fwhmset));
    maxsysrelerr250 = zeros(length(centreset), length(fwhmset));
    meansysabserr1250 = zeros(length(centreset), length(fwhmset));
    maxsysabserr1250 = zeros(length(centreset), length(fwhmset));
    maxsysrelerr1250 = zeros(length(centreset), length(fwhmset));

    for icentre=1:length(centreset),
        for ifwhm=1:length(fwhmset),

            wsource = 200:0.2:1000;          % Define the wavelength axis
from 200 nm to 1000 nm in 0.2 nm steps, the step size directly reflects
the resolution of the spectra from Thorlabs
            newcentrew = centreset(icentre);
            if ls==3,
                fwhm = fwhmset(ifwhm);
            elseif ls==1,
                fwhm = gledfwhm;
            elseif ls==2,
                fwhm = wledfwhm;
            else
                fwhm = 0;            %laser case
            end;
            isource = DefineLightSourceSpectrum( ls, newcentrew, wsource,
0, fwhm, 0, 0, wgled, igled, gledcw, wwled, iwled, wledcw);
            % Find centre of final spectrum
            imom = 0;
            for i=1:length(wsource),
                imom = imom + isource(i)*wsource(i);
            end;
            sourcecw = imom/sum(isource);
            % Optional plot of the source spectrum
            if iplot==1,
                figure
                plot( wsource, isource, 'k-', 'LineWidth', 2);
                set(gca, 'FontSize', 14);
                grid on;
                title(sprintf('Source Spectrum for Simulation, Calculated
Centre Wavelength %.2f nm', sourcecw), 'FontSize', 16);
            end;
```

```
            % Now we have the source spectrum in a common format in
wsource,
            % isource.  Carry out simulation

            % This line is dependent on the phase step algorithm
            % Note the most accurate value for the source centre
wavelength will
            % come from the centre of mass calculation above, hence base
the steps
            % on this
            opdstep = [0 sourcecw/4 sourcecw/2 sourcecw*3/4];        %
Define the phase steps that we will be using, nm

            inten = zeros(nopd, length(opdstep));                   % To
store the phase stepped intensities as a function of OPD and phase step

            % 2 beam interference intensity equation: I = Idc + Im * cos(
2 pi x / w)
            % Assume perfect interference for now
            idc = 1;
            im = 1;
            % Loop and sum intensities for each OPD and each wavelength
            for iiopd = 1:nopd,
                for iiw = 1:length(wsource),
                    for kk = 1:length(opdstep);
                        ph = 2*pi*(opd(iiopd)+opdstep(kk))/wsource(iiw);
                        inten( iiopd, kk) = inten( iiopd, kk) +
isource(iiw)*(idc + im*cos(ph));       % Now modifies each intensity by
the intensity at that wavelength from the LED spectrum
                    end;
                end;
            end;
            inten = inten./sum(isource);
            % Check by plotting phase stepped intensities before re-
scaling or
            % adding noise
            if iplot==1,
                figure
                plot( opd, inten(:,1), 'k-', 'LineWidth', 2);
                xlabel('OPD (nm)');
                ylabel('Interference Intensity (arb.)');
                hold on;
                plot( opd, inten(:,2), 'k:', 'LineWidth', 2);
            end;
            % Modify intensities to new IDC and IM
            newidc = 1350;                             % Based on
experimental measurements
            newim = 475;
            inten = ((inten-idc)./im*newim) + newidc;

            % Add multiplicative noise
            global AMNpn AMNnframes
            AMNpn = 2.5;
            AMNnframes = 1;                            % Change this value to
>1 for frame averaging (integer)
            inten = TTAddMultNoise(inten, 0, 0);

            % Calculate the wrapped phase
            %% This line is dependent on the phase step algorithm
            global Wlm
            Wlm = 0;
```

```
      global WFFANlm
      WFFANlm = 0;
      [wrph moddepth] = TTWrappedFFAN(inten, 0, 0);

% Generate the expected phase function at the mid-point of the wavelength
range
      meanph = 2*pi*opd/(sourcecw);

% And hence get the phase error by taking the difference of the unwrapped
phase from phase stepping and the expected phase
      pherr = unwrap(wrph)-meanph';

% Calculate errors in terms of optical path difference at the mean
wavelength (in nm)
      opderr = pherr/(2*pi)*(sourcecw);
      stdopderr = std( opderr);

      % Determine error up to a certain OPD (250 nm)
      %clear relerr
      opdthreshold_250 = 250;
      idx = find(opd>=opdthreshold_250, 1, 'first');
      meansysabserr250(icentre, ifwhm) = mean(abs(opderr(1:idx)));
      maxsysabserr250(icentre, ifwhm) = max(abs(opderr(1:idx)));
      relerr = opderr(1:idx) - mean(opderr(1:idx));
      maxsysrelerr250(icentre, ifwhm) = max(abs(relerr));

      % Determine error up to a certain OPD (250 nm)
      s = sprintf('Centre %.1f nm, BW %.1f, Max OPD Error is %.3f nm
and Mean OPD Error is %.3f nm up to an OPD of %.1f nm', ...
        newcentrew, fwhm, maxsysabserr250(icentre, ifwhm),
meansysabserr250(icentre, ifwhm), opdthreshold_250);
      disp(s);

      % Determine error up to a certain OPD (1250 nm)
      %clear relerr
      opdthreshold_1250 = 1250;
      idx = find(opd>=opdthreshold_1250, 1, 'first');
      meansysabserr1250(icentre, ifwhm) = mean(abs(opderr(1:idx)));
      maxsysabserr1250(icentre, ifwhm) = max(abs(opderr(1:idx)));
      relerr = opderr(1:idx) - mean(opderr(1:idx));
      maxsysrelerr1250(icentre, ifwhm) = max(abs(relerr));

      % Determine error up to a certain OPD (1250 nm)
      s = sprintf('Centre %.1f nm, BW %.1f, Max OPD Error is %.3f nm
and Mean OPD Error is %.3f nm up to an OPD of %.1f nm', ...
        newcentrew, fwhm, maxsysabserr1250(icentre, ifwhm),
meansysabserr1250(icentre, ifwhm), opdthreshold_1250);
      disp(s);

    end;
  end;

  % Generate a plot to show output
  figure
  if ls==3,
    subplot(221);
    surf( fwhmset, centreset, meansysabserr250);
    xlabel('Bandwidth (nm)');
    ylabel('Centre Wavelength (nm)');
    zlabel('Mean Abs Error (nm)');
    title('Evaluated Over 250 nm OPD','FontSize',14);
```

```
        v=axis;
        axis([min(fwhmset) max(fwhmset) min(centreset) max(centreset) 0
v(6)]);
        set(gca, 'FontSize', 12);
        subplot(222);
        surf( fwhmset, centreset, maxsysabserr250);
        xlabel('Bandwidth (nm)');
        ylabel('Centre Wavelength (nm)');
        zlabel('Max Abs Error (nm)');
        title('Evaluated Over 250 nm OPD','FontSize',14);
        v=axis;
        axis([min(fwhmset) max(fwhmset) min(centreset) max(centreset) 0
v(6)]);
        set(gca, 'FontSize', 12);
        subplot(223);
        surf( fwhmset, centreset, meansysabserr1250);
        xlabel('Bandwidth (nm)');
        ylabel('Centre Wavelength (nm)');
        zlabel('Mean Abs Error (nm)');
        title('Evaluated Over 1250 nm OPD','FontSize',14);
        v=axis;
        axis([min(fwhmset) max(fwhmset) min(centreset) max(centreset) 0
v(6)]);
        set(gca, 'FontSize', 12);
        subplot(224);
        surf( fwhmset, centreset, maxsysabserr1250);
        xlabel('Bandwidth (nm)');
        ylabel('Centre Wavelength (nm)');
        zlabel('Max Abs Error (nm)');
        title('Evaluated Over 1250 nm OPD','FontSize',14);
        v=axis;
        axis([min(fwhmset) max(fwhmset) min(centreset) max(centreset) 0
v(6)]);
        set(gca, 'FontSize', 12);
    else
        subplot(221);
        plot( centreset, meansysabserr250, 'k-', 'LineWidth', 2);
        xlabel('Centre Wavelength (nm)');
        ylabel('Mean Abs Error (nm)');
        title('Evaluated over 250 nm OPD','FontSize',14);
        set(gca, 'FontSize', 12);
        v=axis;
        axis([min(centreset) max(centreset) 0 v(4)]);
        grid on;
        subplot(222);
        plot( centreset, maxsysabserr250, 'k-', 'LineWidth', 2);
        xlabel('Centre Wavelength (nm)');
        ylabel('Max Abs Error (nm)');
        title('Evaluated over 250 nm OPD','FontSize',14);
        set(gca, 'FontSize', 12);
        v=axis;
        axis([min(centreset) max(centreset) 0 v(4)]);
        grid on;
        subplot(223);
        plot( centreset, meansysabserr1250, 'k-', 'LineWidth', 2);
        xlabel('Centre Wavelength (nm)');
        ylabel('Mean Abs Error (nm)');
        title('Evaluated over 1250 nm OPD','FontSize',14);
        set(gca, 'FontSize', 12);
        v=axis;
        axis([min(centreset) max(centreset) 0 v(4)]);
        grid on;
        subplot(224);
```

```
        plot( centreset, maxsysabserr1250, 'k-', 'LineWidth', 2);
        xlabel('Centre Wavelength (nm)');
        ylabel('Max Abs Error (nm)');
        title('Evaluated over 1250 nm OPD','FontSize',14);
        set(gca, 'FontSize', 12);
        v=axis;
        axis([min(centreset) max(centreset) 0 v(4)]);
        grid on;
    end;
end;

return;
```

B.1 Reconstruction of 2D and 3D phase maps in MATLAB

```
% To read phase shifted images and find phase map

clear
close all;

% Reading all image files one by one
I1 = imread('0.tiff');
I2 = imread('1.tiff');
I3 = imread('2.tiff');
I4 = imread('3.tiff');
I5 = imread('4.tiff');
I6 = imread('5.tiff');
I7 = imread('6.tiff');
I_bg = imread('black.tiff');

% % Saving images in bmp format
% I1_bmp = I1/16-I_bg;
% I1_bmp = uint8(I1_bmp);
% imwrite(I1_bmp,'I1.bmp','bmp');
% info = imfinfo('0.tiff');

I1 = double(I1-I_bg); I2 = double(I2-I_bg); I3 = double(I3-I_bg);
I4 = double(I4-I_bg); I5 = double(I5-I_bg); I6 = double(I6-I_bg);
I7 = double(I7-I_bg);

figure('Color', [1 1 1]);
subplot_tight(3,3,1),imagesc(I1),title('(a)- 0','FontSize', 16)
axis image, colormap gray,set(gca,'FontSize',20),axis off
subplot_tight(3,3,2),imagesc(I2),title('(b)- \pi/3','FontSize', 16) axis
image,colormap gray,set(gca,'FontSize',20),axis off
subplot_tight(3,3,3),imagesc(I3),title('(c)- 2\pi/3','FontSize', 16) axis
image,colormap gray,set(gca,'FontSize',20),axis off
subplot_tight(3,3,4),imagesc(I4),title('(d)- \pi','FontSize', 16) axis
image,colormap gray,set(gca,'FontSize',20),axis off
subplot_tight(3,3,5),imagesc(I5),title('(e)- 4\pi/3','FontSize',16) axis
image,colormap gray,set(gca,'FontSize',20),axis off
subplot_tight(3,3,6),imagesc(I6),title('(f)- 5\pi/3','FontSize',16) axis
image,colormap gray,set(gca,'FontSize',20),axis off
subplot_tight(3,3,8),imagesc(I7),title('(g)- 2\pi','FontSize',16) axis
image,colormap gray,set(gca,'FontSize',20),axis off
axis tight

% Performing image filtering using a 3x3 lowpass Kernel filter
I1 = TTImageAverage3x3(I1,[3 3]); I2 = TTImageAverage3x3(I2,[3 3]);
I3 = TTImageAverage3x3(I3,[3 3]); I4 = TTImageAverage3x3(I4,[3 3]);
I5 = TTImageAverage3x3(I5,[3 3]); I6 = TTImageAverage5x5(I6,[5 5]);
I7 = TTImageAverage5x5(I7,[5 5]);

% Stacking four phase shifted images
I(:,:,1) = I1; I(:,:,2) = I2; I(:,:,3) = I3; I(:,:,4) = I4;
I(:,:,5) = I5; I(:,:,6) = I6; I(:,:,7) = I7;

hf = figure('Color', [1 1 1]);
subplot(2,2,1)
hs = slice(I,[],[],1:7);
title('(a)- Stack of images 6+1@60° phase step','FontSize', 16); shading
interp; set(hs,'FaceAlpha',0.8)
set(gca,'YDir','reverse','ZLim',[0 size(I,3)+1],'YLim',[0 1040], 'XLim',[0
1392]); colormap gray; axis tight; zlim([0 8])
```

```
% Calculate phase shift accuracy using Carre technique (Eq.Eq.3.33,
"PHASE-MEASUREMENT
% INTERFEROMETRY TECHNIQUES", Katherine Creath), mean phase shit angle
alpha = 2*atan(sqrt((3*(I2-I3)-(I1-I4))./((I1-I4)+(I2-I3))));

% find the non-zeros values in the imaginary part of alpha
ind = find(imag(alpha));
alpha(ind)=NaN;
alpha = abs(alpha);
alpha(alpha>pi)=NaN;
alpha = alpha*180/pi;
[n,xout] = hist(alpha(:),50);

%figure(3)
subplot_tight(2,2,3),
bar(xout,n);
set(gca,'FontSize',16);
title('(c)- Mean phase shift angle (in degree)','FontSize', 16);
xlim([0 180]);
grid on

%Overlay the mean
alpha1 = alpha(:);
alpha1(isnan(alpha))=[];
mu = mean(alpha1);
hold on
plot([60,60],ylim,'r--','LineWidth',1.5)
hold off

%Displaying the Std on plot
alpha(alpha<50|alpha>70) = NaN;
std = std(alpha(:),'omitnan');
stdlabel=sprintf('Std Dev -- %3.2d', std);
h=annotation('textbox',[0.58 0.75 0.1 0.1],'FontWeight','normal',...
    'FontSize',18,'FitBoxToText','on','LineStyle', 'none');
set(h,'String',stdlabel);

% Calculating wrapped phase map using atan2 function that considers the
quadrant so the output will be between -pi and +pi.
numerator = sqrt(3)*(I2 + I3 - I5 - I6);
denominator = -I1 - I2 + I3 + 2*I4 + I5 - I6 - I7;
wrph = atan2( numerator, denominator);

subplot_tight(2,2,2),
imagesc(wrph,[-pi pi])
title('(b)- Wrapped phase map','FontSize', 16);
set(gca,'FontSize',16);
hcb = colorbar;
colorTitleHandle = get(hcb,'Title');
titleString = 'Rad';
set(colorTitleHandle ,'String',titleString);
colormap gray
axis image
axis off

% Calling the 2D-SRNCP phase unwrapper from the C language code to
% compile the C code in Matlab. The wrapped phase should have the
% single data type (float in C)

        mex Miguel_2D_unwrapper.cpp
```

```
Unwrph = Miguel_2D_unwrapper(single(wrph));
Unwrph = double(Unwrph);

subplot_tight(2,2,4)
imagesc(Unwrph);
title('(d)- Unwrapped phase map', 'FontSize', 16);
hcb = colorbar;
colorTitleHandle = get(hcb,'Title');
titleString = 'Rad'; set(gca,'FontSize',16);
colorbar; colormap(bone); axis image; axis off
save('6+1F@60.mat','Unwrph')

% Calculation of recorded modulation of phase
moddepth = sqrt(numerator.*numerator + denominator.*denominator);
save('6+1FMOD@60.mat','moddepth');
SignalMaxValue = max(max(moddepth));
SignalMeanValue = mean2(moddepth);
figure('Color', [1 1 1]);
subplot(2,1,1)
imagesc(moddepth, [0 max(max(moddepth))])
set(gca,'YDir','reverse','FontSize',16);
title('(a)- Signal modulation depth','FontSize',16)
colormap(gray)
axis image
colorbar
[I, N]=size(moddepth);

hold on
line([1,N],[210,210],'Color','r','LineWidth',2)
hold off

subplot_tight(2,1,2)
plot(moddepth(210,1:N),'Color','r','LineWidth',3)
title('(b)- Signal modulation profile of the row 210','fontsize',16)
set(gca,'FontSize',16)

% Plotting 2d and 3d surface maps on top of each other
figure('Color', [1 1 1]);
surf(Unwrph);shading interp
title('2D and 3D Surface phase maps','FontSize',16);
zlabel('Depth in Radian','FontSize',16)
set(gca,'YDir','reverse','FontSize',16)
grid off

% get the corners of the domain in which the data occurs.
[x,y,z] = size(Unwrph);
min_x = min(min(Unwrph));
min_y = min(min(Unwrph));
max_x = max(max(x));
max_y = max(max(y));

% the image data you want to show as a plane.
planeimg = real(Unwrph);

% scaling image between [0, 255] to use a custom colourmap for it.

minplaneimg = min(min(planeimg)); % find the minimum
scaledimg = (floor(((planeimg - minplaneimg) ./ ...
    (max(max(planeimg)) - minplaneimg)) * 255)); % perform scaling
```

```
% convert the image to a true color image with the jet colormap.
colorimg = ind2rgb(scaledimg,copper(256));
set(gca,'FontSize',16)

% set the hold on so we can show multiple plots/surfs in the figure.
hold on

% do a normal surface plot.
surf(Unwrph,'edgecolor','none','LineStyle', 'none', 'FaceColor',
'interp'); xlim([1 1392]); ylim([1 1040]); colormap(bone); colorbar

% desired z position of the image plane.
imgzposition = -10;

% plot the image plane using surf.
surf([min_y max_y],[min_x max_x],rePSAt(imgzposition, [2 2]),...
    colorimg,'facecolor','texture','edgecolor','none')

% set the view.
view(45,30); zlim([-10 inf])

% Plotting wrapped phase map
figure('Color', [1 1 1]);
subplot(211), imagesc(wrph)
title('(a) Wrapped phase map')
set(gca,'FontSize',16); axis image; colorbar; colormap gray

subplot(212)
imagesc(Unwrph)
set(gca,'FontSize',16)
title('(b) Unwrapped phase map')
axis image; colorbar; colormap bone

% Plotting unwrapped phase map with all phase shifted
% interference frames.

f1=figure('Color', [1 1 1]);
subplot(571); imagesc(I1),axis image,colormap(gray), axis off, title('(a)-
0'),set(gca,'FontSize',16)
subplot(572); imagesc(I2),axis image,colormap(gray), axis off, title('(b)-
\pi/3'),set(gca,'FontSize',16)
subplot(573); imagesc(I3),axis image,colormap(gray), axis off, title('(c)-
2\pi/3'),set(gca,'FontSize',16)
subplot(574); imagesc(I4),axis image,colormap(gray), axis off, title('(d)-
4\pi/3'),set(gca,'FontSize',16)
subplot(575); imagesc(I5),axis image,colormap(gray), axis off, title('(e)-
5\pi/3'),set(gca,'FontSize',16)
subplot(576); imagesc(I6),axis image,colormap(gray), axis off, title('(f)-
2\pi'),set(gca,'FontSize',16)
subplot(577); imagesc(I7),axis image,colormap(gray), axis off, title('(g)-
7\pi/3'),set(gca,'FontSize',16)
subplot(5,7,[8 35]); imagesc(Unwrph),axis image,colormap (gray), axis off,
title('(h)- QPI phase image')
colorbar,set(gca,'FontSize',16)

% Marking cellular and sub-cellular structural features in
% quantitative phase image

% Create textarrow
annotation(f1,'textarrow',[0.416875 0.455625],...
```

```
    [0.595938775510201 0.637755102040814],'Color',[1 0 0], 'String',
{'Nuclei'}, 'LineWidth',2, 'LineStyle',':', 'FontSize',20);

% Create arrow
annotation(f1,'arrow',[0.3775 0.386875],...
    [0.568877551020407 0.525510204081631],'Color',[1 0 0], 'LineWidth',2,
'LineStyle',':');

% Create arrow
annotation(f1,'arrow',[0.455 0.41375],...
    [0.512755102040816 0.515306122448978],'Color',[1 0 0], 'LineWidth',2,
'LineStyle',':');

% Create textarrow
annotation(f1,'textarrow',[0.598125000000002 0.576875000000001],...
    [0.507928571428569 0.594387755102039],'Color',[1 0 0], 'String',
{'Cell wall'},...
    'LineWidth',2, 'LineStyle',':', 'FontSize',20);

% Create arrow
annotation(f1,'arrow',[0.593125 0.56875],...
    [0.457908163265305 0.367346938775509],'Color',[1 0 0],'LineWidth',2,
'LineStyle',':');

% Create textarrow
annotation(f1,'textarrow',[0.345 0.308125],[0.4375 0.478316326530612],...
    'Color',[1 0 0],'String',{'Cell membrane'},'LineWidth',2,...
    'LineStyle',':', 'FontSize',20);

% Create textarrow
annotation(f1,'textarrow',[0.49375 0.4775],...
    [0.538540816326525 0.614795918367347],'Color',[1 0 0],...
    'String',{'Nucleolus'},'LineWidth',2,'LineStyle',':',...
    'FontSize',20);

% Plotting subsection of the image
Nuclei = imcrop(Unwrph,[510 70 250 240]);
fh=figure('Color', [1 1 1]);
subplot(231), imagesc(Unwrph)
title('(a)- Phase map of an onion cells')
set(gca,'FontSize',16); axis image; colormap jet; colorbar

subplot(232), imagesc(Nuclei)
title('(b)- Inset of nucleus from a')
set(gca,'FontSize',16); axis image; colormap jet; colorbar

hold on
[xx,yy]=size(Nuclei);
line([1,yy],[80,80],'Color','r','LineWidth',2)
line([1,yy],[100,100],'Color','k','LineWidth',2)
line([1,yy],[135,135],'Color','m','LineWidth',2)
hold off

% Create rectangle
annotation(fh,'rectangle',...
    [0.186875 0.799744897959183 0.04225 0.06489795918363],'Color',[1 0
0],'LineWidth',1);

% Create arrow
annotation(fh,'arrow',[0.2275 0.408],...
    [0.85979387755102 0.907],'Color',[1 0 0],'LineWidth',2);
```

```
% Create arrow
annotation(fh,'arrow',[0.2275 0.408],...
    [0.799744897959183 0.6],'Color',[1 0 0],'LineWidth',2);

subplot(234)
plot(Nuclei(80,1:yy),'Color','r','LineWidth',3)
title('(c)- Phase profile of the row 80'), set(gca,'FontSize',16),xlim([0
yy])
subplot(235)
plot(Nuclei(100,1:yy),'Color','k','LineWidth',3)
title('(d)- Phase profile of the row 100'), set(gca,'FontSize',16),xlim([0
yy])
subplot(236)
plot(Nuclei(135,1:yy),'Color','m','LineWidth',3)
title('(e)- Phase profile of the row 135'), set(gca,'FontSize',16),xlim([0
yy])
```

BIBLIOGRAPHY

[1] V. Ntziachristos, “Fluorescence molecular imaging,” *Annual review of biomedical engineering*, vol. 8, pp. 1–33, 2006.

[2] B. Huang, M. Bates, and X. Zhuang, “Super-resolution fluorescence microscopy,” *Annual review of biochemistry*, vol. 78, pp. 993–1016, 2009.

[3] A. K. Shiau, M. E. Massari, and C. C. Ozbal, “Back to basics: label-free technologies for small molecule screening,” *Combinatorial chemistry & high throughput screening*, vol. 11, no. 3, pp. 231–7, 2008.

[4] L. K. Minor, “Label-free cell-based functional assays,” *Combinatorial chemistry & high throughput screening*, vol. 11, no. 7, pp. 573–580, 2008.

[5] R. Y. Tsien, “The green fluorescent protein,” *Annual review biochemistry*, vol. 67, pp. 509–44, 1998.

[6] M. Ehrenberg, “The green fluorescent protein: discovery, expression and development,” *The Royal Swedish Academy of Sciences*, 2008.

[7] D. Lasne, G. A. Blab, F. De Giorgi, F. Ichas, B. Lounis, and L. Cognet, “Label-free optical imaging of mitochondria in live cells,” *Optics express*, vol. 15, no. 21, pp. 14184–14193, 2007.

[8] F. Zernike, “How I discovered phase contrast,” *Science*, vol. 121, no. 3141, pp. 345–349, 1955.

[9] W. Lang, *Nomarski differential interference-contrast microscopy*. Oberkochen, Carl Zeiss, 1982.

[10] C. Petibois, “Imaging methods for elemental, chemical, molecular, and morphological analyses of single cells,” *Analytical and bioanalytical chemistry*, vol. 397, no. 6, pp. 2051–2065, 2010.

[11] T. F. Massoud, T. F. Massoud, S. S. Gambhir, and S. S. Gambhir, “Molecular imaging in living subjects: seeing fundamental biological processes in a new light,” *Genes & development*, vol. 17, pp. 545–580, 2003.

[12] A. F. Fercher, “Optical coherence tomography,” *Journal of biomedical optics*, vol. 1, no. 2, pp. 157–173, 1996.

[13] A. Lasslett, “Principles and Applications of Differential Interference Contrast Light Microscopy,” *Microscopy and Analysis*, vol. 20, no. 5, pp. S9–S11, 2006.

[14] G. Popescu *et al.*, “Fourier phase microscopy for investigation of biological structures and dynamics,” *Optics letters*, vol. 29, no. 21, pp. 2503–2505, 2004.

[15] G. Popescu, T. Ikeda, R. Dasari, and M. S. Feld, “Diffraction phase microscopy for quantifying cell structure and dynamics,” *Optics letters*, vol. 31, no. 6, pp. 775–777,

2006.

[16] M. Mir, B. Bhaduri, R. Wang, R. Zhou, and G. Popescu, “Quantitative Phase Imaging,” in *Progress in Optics*, vol. 57, Elsevier, 2012, pp. 133–217.

[17] K. Lee *et al.*, “Quantitative phase imaging techniques for the study of cell pathophysiology: from principles to applications,” *Sensors*, vol. 13, no. 4, pp. 4170–4191, 2013.

[18] G. Gaietta, “Multicolor and electron microscopic imaging of connexin trafficking,” *Science*, vol. 296, no. 5567, pp. 503–507, 2002.

[19] C. Antczak, J. Mahida, C. Singh, P. Calder, and H. Djaballah, “A high content assay to assess cellular fitness,” *Combinatorial chemistry & high throughput screening*, vol. 17, no. 1, pp. 12–24, 2014.

[20] R. M. F. Khalaf and D. R. Bainbridge, “Nomarski differential interference contrast studies of murine lymphocytes,” *European journal of immunology*, vol. 11, no. 10, pp. 816–824, 1981.

[21] B. Rappaz, B. Breton, E. Shaffer, and G. Turcatti, “Digital holographic microscopy: a quantitative label-free microscopy technique for phenotypic screening,” *Combinatorial chemistry & high throughput screening*, vol. 17, no. 1, pp. 80–88, 2014.

[22] P. Marquet *et al.*, “Digital holographic microscopy: a noninvasive contrast imaging technique allowing quantitative visualization of living cells with subwavelength axial accuracy,” *Optics letters*, vol. 30, no. 5, pp. 468–470, 2005.

[23] J. Marrison, L. Räty, P. Marriott, and P. O’Toole, “Ptychography - a label free, high-contrast imaging technique for live cells using quantitative phase information,” *Scientific reports*, vol. 3, p. 2369, 2013.

[24] R. N. Shagam and J. C. Wyant, “Optical frequency shifter for heterodyne interferometers using multiple rotating polarization retarders,” *Applied optics*, vol. 17, no. 19, pp. 3034–3035, 1978.

[25] K. Creath, “V Phase measurement interferometry techniques,” in *Progress in Optics XXVI*, 1988, pp. 351–393.

[26] Z. Wang, *Spatial light interference microscopy and applications*. University of Illinois at Urbana-Champaign, 2011.

[27] C. Seniya, C. E. Towers, and D. P. Towers, “Low cost label-free live cell imaging for biological samples,” in *Quantitative Phase Imaging III*, 2017, vol. 10074, p. 100741I.

[28] C. Seniya, C. E. Towers, and D. P. Towers, “Improvements in low-cost label-free QPI microscope for live cell imaging,” in *Advances in Microscopic Imaging*, 2017, vol. 10414, p. 104140F.

[29] Z. Wang *et al.*, “Spatial light interference microscopy (SLIM),” *Optics express*, vol. 19, no. 2, pp. 1016–1026, 2011.

[30] T. Kim *et al.*, “White-light diffraction tomography of unlabelled live cells,” *Nature photonics*, vol. 8, no. 3, p. 256, 2014.

[31] M. Mir, K. Tangella, and G. Popescu, “Blood testing at the single cell level using quantitative phase and amplitude microscopy,” *Biomedical optics express*, vol. 2, no. 12, pp. 3259–3266, 2011.

[32] N. T. Shaked, L. L. Satterwhite, M. J. Telen, G. A. Truskey, and A. Wax, “Quantitative microscopy and nanoscopy of sickle red blood cells performed by wide field digital interferometry,” *Journal of biomedical optics*, vol. 16, no. 3, p. 30506, 2011.

[33] Y. Park *et al.*, “Refractive index maps and membrane dynamics of human red blood cells parasitized by Plasmodium falciparum,” *Proceedings of the National Academy of Sciences of the United States of America*, vol. 105, no. 37, pp. 13730–13735, 2008.

[34] S. Wang, L. Xue, J. Lai, and Z. Li, “Three-dimensional refractive index reconstruction of red blood cells with one-dimensional moving based on local plane wave approximation,” *Journal of optics*, vol. 14, no. 6, p. 065301 (9pp), 2012.

[35] Z. Wang, K. Tangella, A. Balla, and G. Popescu, “Tissue refractive index as marker of disease,” *Journal of biomedical optics*, vol. 16, no. 11, p. 116017, 2011.

[36] M. Schurmann, J. Scholze, P. Muller, J. Guck, and C. J. Chan, “Cell nuclei have lower refractive index and mass density than cytoplasm,” *Journal of biophotonics*, vol. 9, no. 10, pp. 1068–1076, 2016.

[37] M. Mir *et al.*, “Optical measurement of cycle-dependent cell growth,” *Proceedings of the National Academy of Sciences of the United States of America*, vol. 108, no. 32, pp. 13124–13129, 2011.

[38] K. G. Phillips, S. L. Jacques, and O. J. T. McCarty, “Measurement of single cell refractive index, dry mass, volume, and density using a transillumination microscope,” *Physical review letters*, vol. 109, no. 11, p. 118105, 2012.

[39] G. Popescu and Y. K. Park, “Optical imaging of cell mass and growth dynamics,” *American journal of cell physiology - cell physiology*, vol. 295, pp. 538–544, 2008.

[40] H. Ding and G. Popescu, “Instantaneous spatial light interference microscopy,” *Optics express*, vol. 18, no. 2, pp. 1569–1575, 2010.

[41] E. Cuche, F. Bevilacqua, and C. Depeursinge, “Digital holography for quantitative phase-contrast imaging,” *Optics letters*, vol. 24, no. 5, pp. 291–293, 1999.

[42] E. M. Kim, S. Yazdanfar, and V. Dylov, “Quantitative phase microscopy for label-free high-contrast cell imaging,” US 8,934,103 B2, 2015.

[43] Y. S. Baek, K. R. Lee, J. Yoon, K. Kim, and Y. K. Park, “White-light quantitative phase imaging unit,” *Optics express*, vol. 24, no. 9, pp. 9308–9315, 2016.

[44] K. Creath, “Phase-shifting speckle interferometry,” *Applied Optics*, vol. 24, no. 18, pp. 3053–3058, 1985.

[45] C. E. Towers, D. P. Towers, and J. D. C. Jones, “Generalized frequency selection in multifrequency interferometry,” *Optics letters*, vol. 29, no. 12, pp. 1348–1350, 2004.

[46] M. J. Gander *et al.*, “Embedded micromachined fiber-optic fabry-perot pressure sensors in aerodynamics applications,” *IEEE Sensors journal*, vol. 3, no. 1, pp. 102–107, 2003.

[47] S. Watson *et al.*, "Investigation of shock waves in explosive blasts using fibre optic pressure sensors," *Measurement science and technology*, vol. 17, no. 6, pp. 1337–1342, 2006.

[48] P. Carré, "Installation et utilisation du comparateur photoélectrique et interférentiel du Bureau International des Poids et Mesures," *Metrologia*, vol. 2, no. 1, pp. 13–23, 1966.

[49] T. Otaki, "Artifact halo reduction in phase contrast microscopy using apodization," *Optical review*, vol. 7, no. 2, pp. 119–122, 2000.

[50] D. Gabor, "A new microscopic principle," *Nature*, no. 4098, pp. 777–778, 1948.

[51] D. B. Murphy and M. W. Davidson, "Differential interference contrast microscopy and modulation contrast microscopy," in *Fundamentals of light microscopy and electronic imaging*, Second Ed., Wiley Online Library, 2012, pp. 173–198.

[52] C. Preza, S. King, N. Dragomir, and C. Cogswell, "Phase imaging microscopy: beyond dark-field, phase contrast, and differential interference contrast microscopy," in *Handbook of biomedical optics*, David A. Boas, Ed. CRC Press, 2011, pp. 483–514.

[53] K. I. Willig, R. R. Kellner, R. Medda, B. Hein, S. Jakobs, and S. W. Hell, "Nanoscale resolution in GFP-based microscopy," *Nature methods*, vol. 3, no. 9, pp. 721–723, 2006.

[54] S. W. Hell and J. Wichmann, "Stimulated emission depletion fluorescence microscopy," *Optics letters*, vol. 19, no. 11, pp. 780–782, 1994.

[55] E. Abbe, "Beiträge zur Theorie des Mikroskops und der mikroskopischen Wahrnehmung," *Archiv für mikroskopische anatomie*, vol. 9, no. 1, pp. 424–468, 1873.

[56] K. Creath, "Dynamic Phase Imaging for in Vitro Process Monitoring and Cell Tracking," in *Conf Proc IEEE Eng Med Biol Soc*, 2011, vol. 6, no. 9, pp. 5977–5980.

[57] W. J. Choi, D. I. Jeon, S. G. Ahn, J. H. Yoon, S. Kim, and B. H. Lee, "Full-field optical coherence microscopy for identifying live cancer cells by quantitative measurement of refractive index distribution," *Optics express*, vol. 18, no. 22, pp. 23285–23295, 2010.

[58] K. Creath and G. Goldstein, "Optical thickness and optical volume measurement of dynamic cellular motion," in *Microscopy and microanalysis conference*, 2013, pp. 1–4.

[59] T. Noda and S. Kawata, "Separation of phase and absorption images in phase-contrast microscopy," *Journal of optical society of America A*, vol. 9, no. 6, pp. 924–931, 1992.

[60] N. Lue *et al.*, "Quantitative phase imaging of live cells using fast Fourier phase microscopy," *Applied optics*, vol. 46, no. 10, p. 1836, 2007.

[61] Z. Wang *et al.*, "Topography and refractometry of nanostructures using spatial light interference microscopy," *Optics letters*, vol. 35, no. 2, pp. 208–2010, 2010.

[62] A. Bouwens and T. Lasser, "Imaging: White-light diffraction tomography," *Nature photonics*, vol. 8, no. 3, pp. 173–174, 2014.

[63] N. Lue and G. Popescu, "Live cell refractometry using Hilbert phase microscopy and

confocal reflectance microscopy," *The journal of physical chemistry A*, vol. 113, no. 47, pp. 13327–13330, 2009.

[64] P. J. Rodrigo, D. Palima, and J. Glückstad, "Accurate quantitative phase imaging using generalized phase contrast," *Optics express*, vol. 16, no. 4, pp. 2498–2509, 2008.

[65] C. Mann, L. Yu, C.-M. Lo, and M. Kim, "High-resolution quantitative phase-contrast microscopy by digital holography," *Optics express*, vol. 13, no. 22, pp. 8693–8698, 2005.

[66] J. W. Goodman and R. W. Lawrence, "Digital image formation from electronically detected holograms," *Applied physics letters*, vol. 11, no. 3, pp. 77–79, 1967.

[67] J. W. Goodman, *Introduction to Fourier Optics*, Third Ed. Roberts and Company Publishers, 2005.

[68] E. Sánchez-Ortiga, A. Doblas, G. Saavedra, M. Martínez-Corral, and J. Garcia-Sucerquia, "Off-axis digital holographic microscopy: practical design parameters for operating at diffraction limit," *Applied optics*, vol. 53, no. 10, pp. 2058–2066, 2014.

[69] T. Ikeda, G. Popescu, R. Dasari, and M. S. Feld, "Hilbert phase microscopy for investigating fast dynamics in transparent systems," *Optics letters*, vol. 30, no. 10, pp. 1165–1167, 2005.

[70] G. Popescu, K. Badizadegan, R. Dasari, and M. S. Feld, "Observation of dynamic subdomains in red blood cells," *Journal of biomedical optics*, vol. 11, no. 4, p. 40503, 2006.

[71] B. Bhaduri, K. Tangella, and G. Popescu, "Fourier phase microscopy with white light," *Biomedical optics express*, vol. 4, no. 8, pp. 1434–1441, 2013.

[72] Y. K. Park *et al.*, "Refractive index maps and membrane dynamics of human red blood cells parasitized by Plasmodium falciparum," *Proceedings of the National Academy of Sciences*, vol. 105, no. 37, pp. 13730–13735, 2008.

[73] K. Creath and G. Goldstein, "Dynamic quantitative phase imaging for biological objects using a pixelated phase mask," *Biomedical optics express*, vol. 3, no. 11, pp. 2866–80, Nov. 2012.

[74] W. Choi *et al.*, "Tomographic phase microscopy," *Nature Methods*, vol. 4, no. 9, pp. 717–719, 2007.

[75] J. P. Haldar, Z. Wang, G. Popescu, and Z.-P. Liang, "Deconvolved spatial light interference microscopy for live cell imaging," *IEEE transactions on biomedical engineering*, vol. 58, no. 9, pp. 2489–2497, 2011.

[76] B. Bhaduri, H. Pham, D. Wickland, and G. Popescu, "Real-time quantitative phase imaging in biomedicine," *SPIE Newsroom*, pp. 2–5, Apr. 2013.

[77] B. Bhaduri, D. Wickland, R. Wang, V. Chan, R. Bashir, and G. Popescu, "Cardiomyocyte imaging using real-time spatial light interference microscopy (SLIM)," *PloS one*, vol. 8, no. 2, p. e56930, 2013.

[78] B. Bhaduri, H. V Pham, M. Mir, and G. Popescu, "Diffraction phase microscopy with

white light," *Optics letters*, vol. 37, no. 6, pp. 1094–1096, 2012.

[79] T. H. Nguyen, C. Edwards, L. L. Goddard, and G. Popescu, "Quantitative phase imaging with partially coherent illumination," *Optics letters*, vol. 39, no. 19, pp. 5511–5514, 2014.

[80] D. Dipresa, *Optical thin film measurement by interferometric fringe projection and fluorescence stimulated emission*. Doctoral dissertation, University of Leeds, 2013.

[81] K. Creath and G. Goldstein, "Dynamic quantitative phase imaging for biological objects using a pixelated phase mask," *Biomedical optics express*, vol. 3, no. 11, pp. 2866–2880, 2012.

[82] N. Brock, B. T. Kimbrough, and J. E. Millerd, "A pixelated micropolarizer-based camera for instantaneous interferometric measurements," in *Polarization science and remote sensing V*, 2011, vol. 8160, p. 81600W.

[83] K. Creath, "Dynamic phase imaging utilizing a 4-dimensional microscope system," in *Three-dimensional and multidimensional microscopy: image acquisition and processing XVIII*, 2011, vol. 79040, p. 79040O.

[84] G. Rajshekhar, B. Bhaduri, C. Edwards, R. Zhou, L. L. Goddard, and G. Popescu, "Nanoscale topography and spatial light modulator characterization using wide-field quantitative phase imaging," *Optics express*, vol. 22, no. 3, pp. 3432–3438, 2014.

[85] C. L. Varley and J. Southgate, "Effects of PPAR agonists on proliferation and differentiation in human urothelium," *Experimental and toxicologic pathology*, vol. 60, no. 6, pp. 435–441, 2008.

[86] R. Huber, M. Wojtkowski, J. G. Fujimoto, J. Y. Jiang, and a E. Cable, "Three-dimensional and C-mode OCT imaging with a compact, frequency swept laser source at 1300 nm," *Optics express*, vol. 13, no. 26, pp. 10523–10538, 2005.

[87] D. C. Adler *et al.*, "Three-dimensional endomicroscopy of the human colon using optical coherence tomography," *Optics express*, vol. 17, no. 2, pp. 784–796, 2009.

[88] D. Huang *et al.*, "Optical coherence tomography," *Science*, vol. 254, no. 5035. pp. 1178–11181, 1991.

[89] T. M. Yelbuz, "Optical Coherence Tomography: A new high-resolution imaging technology to study cardiac development in chick embryos," *Circulation*, vol. 106, no. 22, pp. 2771–2774, 2002.

[90] A. F. Fercher, W. Drexler, C. K. Hitzenberger, and T. Lasser, "Optical coherence tomography - principles and applications," *Reports on progress in physics*, vol. 2, no. 66, pp. 239–303, 2003.

[91] D. P. Towers, T. R. Judge, and P. J. Bryanston-Cross, "Automatic interferogram analysis techniques applied to quasi-heterodyne holography and ESPI," *Optics and lasers in engineering*, vol. 14, pp. 239–281, 1991.

[92] D. Ghiglia and M. Pritt, *Two-dimensional phase unwrapping: theory, algorithms, and software*. 1998.

[93] J. M. Huntley, “Random phase measurement errors in digital speckle pattern interferometry,” *Optics and Lasers in Engineering*, vol. 26, no. 2–3, pp. 131–150, 1997.

[94] R. Jones and C. Wykes, *Holographic and Speckle Interferometry*. Cambridge University Press, 1989.

[95] S. Eng, D. M. Cait, Z. Wang, K. Alameh, and W. Jiang, “Optimization of Liquid-Crystal Spatial Light Modulator for Precise Phase Generation Optimization of Liquid-Crystal Spatial Light Modulator for Precise Phase Generation,” no. 2007, pp. 105–108, 2011.

[96] S. Noorizadeh, “SLM-based fourier differential interference contrast microscopy,” Doctoral dissertation, Portland State University, 2014.

[97] K. Creath, “Temporal phase measurement methods,” in *Interferogram Analysis Digital Fringe Pattern Measurement Techniques*, D. W. Robinson and G. T. Reid, Eds. IOP Publishing, 1993, pp. 94–140.

[98] E. P. Goodwin and J. C. Wyant, *Field guide to interferometric optical testing*. SPIE, 2006.

[99] P. Hariharan, *Optical interferometry*, Second. Academic Press, 2003.

[100] E. Hecht, *Optics*, Fourth. Addison Wesley, 2002.

[101] P. Hariharan, B. F. Oreb, and T. Eiju, “Digital phase-shifting interferometry: a simple error-compensating phase calculation algorithm,” *Applied optics*, vol. 26, no. 5, pp. 2504–2506, 1987.

[102] C. Meneses-Fabian, G. Rodriguez-Zurita, M. C. Encarnacion-Gutierrez, and N. I. Toto-Arellano, “Phase-shifting interferometry with four interferograms using linear polarization modulation and a Ronchi grating displaced by only a small unknown amount,” *Optics communications*, vol. 282, no. 15, pp. 3063–3068, 2009.

[103] X. Xun and R. W. Cohn, “Phase calibration of spatially non uniform spatial light modulators,” *Applied optics*, vol. 43, no. 35, pp. 6400–6406, 2004.

[104] M. P. Kothiyal and C. Delisle, “Shearing interferometer for phase shifting interferometry with polarization phase shifter,” *Applied optics*, vol. 24, no. 24, pp. 4439–4442, 1985.

[105] P. Hariharan, *Basics of interferometry*, Sescond. Elsevier, 2007.

[106] J. Schwider, R. Burow, K. E. Elssner, J. Grzanna, R. Spolaczyk, and K. Merkel, “Digital wave-front measuring interferometry: some systematic error sources,” *Applied optics*, vol. 22, no. 21, pp. 3421–3432, 1983.

[107] Y. Y. Cheng and J. C. Wyant, “Phase shifter calibration in phase-shifting interferometry,” *Applied optics*, vol. 24, no. 18, pp. 3049–3052, 1985.

[108] K. G. Larkin and B. F. Oreb, “Design and assessment of symmetrical phase-shifting algorithms,” *Journal of the optical society of America A*, vol. 9, no. 10, pp. 1740–1748, 1992.

[109] K. Hibino, B. F. Oreb, D. I. Farrant, and K. G. Larkin, “Phase shifting for nonsinusoidal waveforms with phase-shift errors,” *Journal of the optical society of America A*, vol. 12, no. 4, pp. 761–768, 1995.

[110] Y. Surrel, “Additive noise effect in digital phase detection,” *Applied optics*, vol. 36, no. 1, pp. 271–276, 1997.

[111] M.-H. Shen, C.-H. Hwang, and W.-C. Wang, “Using higher steps phase-shifting algorithms and linear least-squares fitting in white-light scanning interferometry,” *Optics and lasers in engineering*, vol. 66, pp. 165–173, 2015.

[112] L. Mavarani *et al.*, “Spectral histopathology of colon cancer tissue sections by Raman imaging with 532 nm excitation provides label free annotation of lymphocytes, erythrocytes and proliferating nuclei of cancer cells,” *The analyst*, vol. 138, no. 14, pp. 4035–4039, 2013.

[113] X. Wu *et al.*, “Label-free detection of breast masses using multiphoton microscopy,” *PloS one*, vol. 8, no. 6, p. e65933, 2013.

[114] M. Kemmler, M. Fratz, D. Giel, N. Saum, A. Brandenburg, and C. Hoffmann, “Noninvasive time-dependent cytometry monitoring by digital holography,” *Journal of biomedical optics*, vol. 12, no. 6, p. 64002, 2007.

[115] R. Barer, “Refractometry and interferometry of living cells,” *Journal of the optical society of America*, vol. 47, no. 6, pp. 545–556, 1957.

[116] J. D. Wilson, W. J. Cottrell, and T. H. Foster, “Index-of-refraction-dependent subcellular light scattering observed with organelle-specific dyes,” *Journal of biomedical optics*, vol. 12, no. 1, p. 14010, 2007.

[117] S. Johnsen and E. Widder, “The physical basis of transparency in biological tissue: ultrastructure and the minimization of light scattering,” *Journal of theoretical biology*, vol. 199, no. 2, pp. 181–98, Jul. 1999.

[118] B. R. Barer and S. Joseph, “Refractometry of living cells Part II. The immersion medium,” *Journal of cell science*, vol. 3, no. 33, pp. 1–27, 1955.

[119] W. Heller, “Remarks on refractive index mixture rules,” *The journal of physical chemistry*, vol. 69, no. 4, pp. 1123–1129, 1965.

[120] X. J. Liang, A. Q. Liu, C. S. Lim, T. C. Ayi, and P. H. Yap, “Determining refractive index of single living cell using an integrated microchip,” *Sensors and Actuators, A: Physical*, vol. 133, no. 2 SPEC. ISS., pp. 349–354, 2007.

[121] C. Buckberry and D. Towers, “New Approaches to the Full-field Analysis of Photoelastic Stress Patterns,” *Optics and lasers in engineering*, vol. 24, no. 1996, pp. 415–442, 1996.

[122] C. Zuo, L. Huang, M. Zhang, Q. Chen, and A. Asundi, “Temporal phase unwrapping algorithms for fringe projection profilometry: A comparative review,” *Optics and lasers in engineering*, vol. 85, pp. 84–103, 2016.

[123] H. O. Saldner and J. M. Huntley, “Temporal phase unwrapping: application to surface profiling of discontinuous objects,” *Applied optics*, vol. 36, no. 13, pp. 2770–2775,

1997.

[124] J. W. Goodman, *Statistical optics*, Second. John Wiley & Sons, 2000.

[125] C. P. Brophy, “Effect of intensity error correlation on the computed phase of phase-shifting interferometry,” *Journal of the optical society of America A*, vol. 7, no. 4, pp. 537–541, 1990.

[126] J. C. Wyant, “Use of an ac heterodyne lateral shear interferometer with real-time wavefront correction systems,” *Applied optics*, vol. 14, no. 11, pp. 2622–2626, 1975.

[127] H. Iwai *et al.*, “Quantitative phase imaging using actively stabilized phase-shifting low-coherence interferometry,” *Optics letters*, vol. 29, no. 20, pp. 2399–2401, 2004.

[128] C. Elliott, V. Vijayakumar, W. Zink, and R. Hansen, “National Instruments LabVIEW: A programming environment for laboratory automation and measurement,” *Journal of Laboratory Automation*, vol. 12, no. 1, pp. 17–24, 2007.

[129] B. R. Hunt, R. L. Lipsman, and J. M. Rosenberg, *A guide to MATLAB*, vol. 53, no. 9. Cambridge University Press, 2001.

[130] K. Itoh, “Analysis of the phase unwrapping algorithm,” *Applied optics*, vol. 21, no. 14, p. 2470, 1982.

[131] F. Zernike, “Phase contrast, a new method for the microscopic observation of transparent objects part- II,” *Physica*, vol. IX, no. 10, pp. 974–985, 1942.

[132] T. H. Nguyen and G. Popescu, “Spatial light interference microscopy (SLIM) using twisted-nematic liquid-crystal modulation,” *Biomedical optics express*, vol. 4, no. 9, pp. 1571–1583, 2013.

[133] Y. Ozeki *et al.*, “High-speed molecular spectral imaging of tissue with stimulated Raman scattering,” *Nature photonics*, vol. 6, pp. 845–851, 2012.

[134] M. A. Herráez, D. R. Burton, M. J. Lalor, and M. A. Gdeisat, “Fast two-dimensional phase-unwrapping algorithm based on sorting by reliability following a noncontinuous path,” *Applied optics*, vol. 41, no. 35, pp. 7437–7444, 2002.

[135] C. Kohler, X. Schwab, and W. Osten, “Optimally tuned spatial light modulators for digital holography,” *Applied optics*, vol. 45, no. 5, pp. 960–967, 2006.

[136] Y. Zeng, J. Xu, D. Li, L. Li, Z. Wen, and J. Y. Qu, “Label-free in vivo flow cytometry in zebrafish using two-photon autofluorescence imaging,” *Optics letters*, vol. 37, no. 13, pp. 2490–2492, 2012.

[137] G. Wang, D. Garcia, Y. Liu, R. de Jeu, and A. Johannes Dolman, “A three-dimensional gap filling method for large geophysical datasets: Application to global satellite soil moisture observations,” *Environmental modelling and software*, vol. 30, pp. 139–142, 2012.

[138] G. Goldstein and K. Creath, “Quantitative phase microscopy: automated background leveling techniques and smart temporal phase unwrapping,” *Applied optics*, vol. 54, no. 16, pp. 5175–5185, 2015.

[139] H. W. Gausman and W. A. Allen, “Optical parameters of leaves of 30 plant species,” *Plant physiology*, vol. 52, pp. 57–62, 1973.

[140] I. Azharul, “Cell - walls of growing plant cells,” Doctoral Dissertation, University of Westminster, 2013.

[141] Y. Tamada *et al.*, “Optical property analyses of plant cells for adaptive optics microscopy,” *International Journal of optomechatronics*, vol. 8, no. 2, pp. 89–99, 2014.

[142] D. A. Collings, C. N. Carter, J. C. Rink, A. C. Scott, S. E. Wyatt, and N. S. Allen, “Plant nuclei can contain extensive grooves and invaginations,” *The plant cell*, vol. 12, no. 12, pp. 2425–2439, 2000.

[143] J. R. Groff, “Estimating the size of onion epidermal cells from diffraction patterns,” *The physics teacher*, vol. 50, no. 7, pp. 420–423, 2012.

[144] W. Wang and C. Li, “Measurement of the light absorption and scattering properties of onion skin and flesh at 633nm,” *Postharvest biology and technology*, vol. 86, pp. 494–501, 2013.